

Study of Mesospheric Gravity Waves in the  
Antarctic Observed by Airglow Imaging  
Network, Using Phase Velocity Spectrum

MATSUDA TAKASHI

Doctor of Philosophy

Department of Polar Science  
School of Multidisciplinary Sciences  
SOKENDAI (The Graduate University for  
Advanced Studies)



Study of Mesospheric Gravity Waves in the  
Antarctic Observed by Airglow Imaging  
Network, Using Phase Velocity Spectrum

Takashi Matsuda

Department of Polar Science

School of Multidisciplinary Sciences

The Graduate University for Advanced Studies

March 2017

# Contents

Abstract	iv
Acknowledgements	vi
1 General Introduction	1
1.1 Earth's Atmosphere.....	1
1.1.1 Temperature and Wind Structures of Earth's Atmosphere.....	1
1.1.2 Atmospheric Wave.....	2
1.2 Atmospheric Gravity Wave.....	3
1.2.1 Linear Theory.....	3
1.2.2 AGW Observation and Model Studies.....	7
2 Airglow Imaging Observation of Atmospheric Gravity Waves	14
2.1 Mesospheric Airglow.....	14
2.2 Airglow Imaging Observation.....	16
2.3 Analysis Method for Airglow Imaging Data.....	20
2.4 Antarctic Airglow Imaging Network and Other Data.....	21
2.5 Purpose and Outline of This Thesis.....	22
3 New Statistical Analysis of Gravity Waves Observed by Airglow Imaging	24
3.1 Observation.....	25
3.2 Analysis Methods.....	25
3.2.1 Spectral Analysis.....	25
3.2.2 Event Analysis.....	29
3.3 Results and Discussion.....	30
3.3.1 Comparison Between Spectral and Event Analyses.....	30
3.3.2 Average Spectrum.....	32
3.3.3 Effects of the Galaxy on the Phase Velocity Spectrum.....	33
3.3.4 Discussion of the Anisotropic Distribution of Phase Velocities.....	34
3.4 Conclusion.....	35
4 Characteristics of Mesospheric Gravity Waves Over the Antarctic	37

4.1 Observation and Analysis.....	38
4.2 Results and Discussion.....	39
4.2.1 Station-to-Station and Day-to-Day Variation.....	39
4.2.2 Comparison with the Blocking Diagram.....	42
4.2.3 Temporal Variation in One Night of May 11–12, 2013.....	44
4.2.4 Wave Period Dependency of the Directionality.....	45
4.3 Conclusion.....	47
5 Summary and Conclusions	49
Appendix	53
References	55
Tables	69
Figures	70

# Abstract

Atmospheric gravity waves (AGW), generated in the lower atmosphere, can propagate to the mesosphere and lower thermosphere. They transport great amounts of energy and momentum and release them at various altitudes. Among many parameters to characterize gravity waves, the horizontal phase velocity is important to discuss the vertical propagation and where the momentum is released. Near the mesopause region, OH and other airglow imagings have been used to investigate horizontal structures of gravity waves for more than two decades. Traditionally, the statistics of these observations are based on the wave characteristics of individual AGW events, which are detected by visual inspection of outstanding wave-like structures in airglow image data. However, such methods are not suitable for the analysis of large amounts of data for a few reasons: (1) the analysis procedure is time-consuming, (2) differences in criteria for determination of wave events, and (3) the extraction of the AGW parameters depends on the work of the people processing the data differences and criteria for the determination of wave events. The latter two might induce biases in the sampling of wave events. These problems cause difficulties in obtaining a global map of gravity wave characteristics in the mesopause region. Another important fact with respect to mesospheric gravity wave studies is that the observations over the Antarctic are few, although a significant amount of AGWs is generated in this region. In this thesis, we aim to reveal the characteristics of horizontal phase velocity distributions of mesospheric small-scale and short-period AGWs in the Antarctic and to investigate the propagation process and source of the AGWs.

First, we developed a new analysis method obtaining the power spectrum in the horizontal phase velocity domain from airglow intensity image data to study AGWs. This method can deal with extensive amounts of imaging data obtained in different years and at various observation sites independent of the work of the people processing the data for the determination of AGW events and extraction of AGW characteristics. The new method was applied to sodium airglow data obtained in 2011 at the Syowa Station (69°S, 40°E) in the Antarctic. The results were compared with those obtained from conventional event analysis in which the phase fronts were traced manually to estimate the horizontal characteristics such as wavelengths, phase velocities, and wave

periods. The horizontal phase velocity of each wave event in the airglow images corresponded closely to a peak in the spectrum. The statistical results of both analyses show the eastward offset of the horizontal phase velocity distribution of AGWs. Both spectral and event analyses showed (1) a cluster of westward-propagating slow ( $< 50\text{--}60$  m/s) waves and (2) the dominance of eastward-propagating waves with high speeds (no complete absence of slower waves in this direction), which could be interpreted as the existence of a stratospheric source in the polar night jet. The galactic contamination of the spectrum was examined by calculating the apparent velocity of the stars and found to be limited for phase speeds lower than 30 m/s.

Subsequently, we obtained horizontal phase velocity distributions of the gravity waves at an altitude of  $\sim 90$  km from four airglow imagers in the Antarctic, which belong to the Antarctic Gravity Wave Imaging/Instrument Network (ANGWIN), an international airglow imager/instrument network in the Antarctic. Results from the airglow imagers at four stations, Syowa, Halley ( $76^\circ\text{S}, 27^\circ\text{W}$ ), Davis ( $69^\circ\text{S}, 78^\circ\text{E}$ ), and McMurdo ( $78^\circ\text{S}, 167^\circ\text{E}$ ), were compared using the new statistical analysis method based on a 3-D Fourier transform developed in this study for the observation period between April and May 2013. Significant day-to-day and site-to-site variations were observed. The two-monthly average of the phase velocity spectrum showed a preferential westward direction at Syowa, McMurdo, and Halley but no preferential direction at Davis. The AGW energy estimated from I/I was  $\sim 5$  times larger at Davis and Syowa than at McMurdo and Halley. We also compared the phase velocity spectrum at Syowa and Davis with the background wind and found that only the directionality over Syowa could be explain with critical level filtering. The gravity waves over Davis, which propagated into all azimuth directions, could be generated above the polar night jet by a mechanism such as secondary wave generation. The comparison of the nighttime variation of phase velocity spectra with background wind measurements suggested that the effect of critical level filtering could not explain the temporal variation of the gravity wave directionality well; however, for the same cases, other reasons such as the variation of wave sources should be taken into account. We also found that the directionality is dependent on gravity wave periods.

# Acknowledgements

The author deeply thanks Drs. Takuji Nakamura (chief supervisor), Yoshihiro Tomikawa (co-supervisor), and Mitsumu K. Ejiri (former co-supervisor, now in the Antarctic). Their great instruction and support have been required for the progress of the author's research and this Ph.D. thesis. They provided the author the analysis of airglow data, spectral analysis, conference presentations, and articles and also introduced the author to many other famous researchers.

The author appreciates the careful support of and useful discussion with Drs. Masaki Tsutsumi, Yasunori Nishiyama, and Takuo T. Tsuda. Their expertise with respect to the middle and upper atmosphere and valuable advice have helped the author.

The author thanks the advisory committee members, Dr. Yasuhiro Murayama and Dr. Hitoshi Fujiwara, for the examination and evaluation of the Ph.D. thesis.

The author is grateful to Dr. Kazuo Shiokawa at Nagoya University for providing the Optical Mesosphere Thermosphere Imagers data for Syowa in 2011 and the co-authorship in the article published in 2014 corresponding to Chapter 3. The author specially thanks the ANGWIN members at Utah State University (USU): Drs. Michael J. Taylor, Yucheng Zhao, and P.-Dominique Pautet. The author spent valuable time for collaborative study at USU due to their hospitality. The USU ANGWIN members, Dr. Damian J. Murphy of the Australian Antarctic Division and Dr. Tracy Moffat-Griffin of the British Antarctic Survey, provided the airglow data observed at the Antarctic and are coauthors in the article corresponding to Chapter 4. I especially thank the 52nd and 54th Japanese Antarctic Research Expedition (JARE) and all members of the 52nd and 54th JARE for the installation and operation of the airglow imager at Syowa.

The author greatly thanks all staff of the National Institute of Polar Research and all the students of the Graduate University for Advanced Studies, Department of Polar Science, for their kind support and encouragement throughout the five years of his Ph.D. work.

Finally, this thesis was financially supported by the Japan Society for the Promotion of Science (JSPS) Grant-in-Aid [JSPS Research Fellow Grant Number JP16J10875].

# Chapter 1

## General Introduction

### 1.1 Earth's Atmosphere

#### 1.1.1 Temperature and Wind Structures of Earth's Atmosphere

The atmosphere on Earth is vertically classified into the troposphere (0–10 km), stratosphere (10–50 km), mesosphere (50–90 km), and thermosphere (90–500 km) based on the temperature structure. The temperature structure up to the mesosphere is shown in Figure 1.1. This vertical structure depends on the profile of heat sources in the atmosphere. The temperature in the troposphere decreases with height at a rate of  $\sim 6.5$  K/km. The tropopause is a boundary between the troposphere and stratosphere defined by a local minimum in the vertical temperature profile. In the stratosphere, the temperature increases with height because of the absorption of ultraviolet radiation ( $\lambda = 200\text{--}300$  nm) by ozone. At the upper boundary of the stratosphere, named stratopause, the temperature shows a local maximum. The temperature in the mesosphere then decreases again with height up to 90 km (mesopause). The temperature in the thermosphere increases with the height. The thermosphere is heated primarily by absorption of extreme ultraviolet radiation and ultraviolet radiation ( $10 < \lambda < 200$  nm). The vertical profile of the Earth's temperature is mainly determined by the radiative equilibrium, which is the balance of atmospheric absorption and radiation.

The atmospheric temperature has not only a vertical but also a latitudinal structure. Figure 1.2 shows the temperature as a function of altitude and latitude in January. In the stratosphere, the temperature is higher in the summer hemisphere because the solar radiation absorbed by ozone is stronger in the summer hemisphere and weaker in the winter hemisphere. In the mesopause, opposite to the stratopause, the temperature is lower in the summer hemisphere and higher in the winter hemisphere. Neutral atmospheric wind velocities also depend on the latitude and altitude, as shown in Figure 1.3. Eastward wind in the winter hemisphere and westward wind in the summer

hemisphere exist at the altitude of 20–80 km, although zonal winds are very weak in the mesopause. The temperature distribution in Figure 1.2 and the wind velocity distribution in Figure 1.3 are related by the thermal wind balance. As described later, the atmospheric meridional pole-to-pole circulation driven by atmospheric gravity waves (AGW) results in the mesospheric latitudinal temperature structure, which is different from the radiative equilibrium. This wave is very important and this study will focus on this topic.

### 1.1.2 Atmospheric Wave

Atmospheric waves in the middle atmosphere are observed as perturbation of the atmospheric density, wind velocity, and temperature with a broad temporal and spatial range. Here, we introduce AGW, atmospheric tides, and Rossby waves.

An AGW is an atmospheric wave; its restoring force is the buoyant force in the stable stratified atmosphere. The AGWs are generated by vertical motion of an air parcel and heating and their generation sources are, for example, the topography, convective and frontal activity, wind shear, and geostrophic adjustment [e.g., *Fritts and Alexander, 2003*]. The horizontal scale ranges from several km to ten thousand km wavelength; the vertical wavelength ranges from 2 to 100 km [*Manson, 1990*], and the wave period varies between the Brunt–Väisälä period (~6 min at the mesopause altitude) and the inertia period (~12.9 h at 69°S). The AGW plays an important role in the vertical coupling of the atmosphere through transport of significant amounts of energy and horizontal momentum into the mesosphere and lower thermosphere (MLT). The momentum transport and subsequent deposition through wave-breaking cause zonal wind accelerations in the mesosphere. The weak zonal wind in the mesopause is a result of such accelerations. The meridional circulation from the summer pole to the winter pole is driven by wave-induced zonal accelerations, which are in balance with the Coriolis torque. The latitudinal temperature structure in the mesosphere is created by the meridional circulation, which causes upward/downward motion with adiabatic cooling/heating around the poles [e.g., *Lindzen, 1981; Holton, 1982; Matsuno, 1982*]. The AGW is one of the major topics of mesospheric studies.

Atmospheric tides are large-scale waves (~40,000 km) in the middle atmosphere. The periods of atmospheric tides are 24 h and its higher harmonics because the major generation source of atmospheric tides is solar heating. Solar heating is induced by absorption of near-infrared radiation by water vapor in the troposphere, ultraviolet radiation by ozone in the stratosphere, and the extreme ultraviolet radiation by molecular oxygen in the thermosphere. The nonlinear coupling of atmospheric tides or tides and planetary waves is also a source of mesospheric tides. Atmospheric tides in the mesosphere originate from other altitudes. Gravitational tides by the moon and the sun are less effective in the atmosphere.

Rossby waves are also large-scale waves with periods longer than a day in the middle atmosphere. Their restoring force is a latitudinal gradient of the Coriolis force. They are generated by topographic forcing, non-uniform thermal distribution, instability, and wave-wave interaction. Rossby waves are classified into free and forced Rossby waves. Free Rossby waves can independently exist after their excitation. Forced Rossby waves need continuous excitation and can propagate vertically when their phase moves westward relative to the background wind. The vertical propagation of the forced Rossby wave is allowed only in the winter hemisphere in which the background wind direction is eastward [Charney and Drazin, 1961]. They contribute to driving the meridional circulation in the stratosphere through westward acceleration of the background wind by wave dissipation.

## 1.2 Atmospheric Gravity Wave

### 1.2.1 Linear Theory

Here, the linear theory of AGWs is introduced for irrotational, frictionless, and adiabatic flow based on Nappo [2012] because small-scale AGWs are investigated in this study. In this Subsection, the coordinates  $(x, z)$  are used in a Cartesian coordinate system with  $x$  in the horizontal direction (positive eastward) and  $z$  in the vertical direction (positive upward). The equation of the motion of an air parcel in the vertical direction can be

described as

$$\frac{d^2(\delta z)}{dt^2} = -\frac{g}{\theta} \frac{\partial \theta}{\partial z} \delta z \quad (1.1)$$

where  $t$ ,  $g$ , and  $\theta$  are the time, acceleration of gravity, and potential temperature, respectively. The potential temperature is the temperature of an air parcel when brought down adiabatically to the height, where the pressure is 1000 hPa (*i.e.*, the ground surface); it is defined as

$$\theta = T_a \left( \frac{1000}{p} \right)^{R/c_p} \quad (1.2)$$

where  $T_a$  is the background temperature,  $R$  is the specific gas constant,  $c_p$  is the specific heat capacity at constant pressure, and  $p$  is the pressure of the air parcel. The displacement of the air parcel,  $\delta z$ , can be described as

$$\delta z(t) = Ae^{iNt} + Be^{-iNt} \quad (1.3)$$

$$N = \sqrt{\frac{g}{\theta} \frac{\partial \theta}{\partial z}} \quad (1.4)$$

where  $A$  and  $B$  are constants and  $N$  is called the Brunt–Väisälä frequency when it is a real number. If  $N$  is an imaginary number, the background atmosphere is statically unstable and the amplitude of the air parcel displacement increases infinitely.

The Taylor–Goldstein equation can describe the wave motion of AGWs under linearization, assuming an irrotational, frictionless, and non-heat conducting atmosphere.

It is given as

$$\frac{d^2 \hat{w}}{dz^2} + \left[ \frac{N^2}{(c_h - u_0)^2} + \frac{1}{(c_h - u_0)} \frac{d^2 u_0}{dz^2} - \frac{1}{H_s} \frac{1}{(c_h - u_0)} \frac{du_0}{dz} - \frac{1}{4H_s^2} - k^2 \right] \hat{w} = 0 \quad (1.5)$$

where  $\hat{w}$  is the vertical speed; and  $c_h$ ,  $u_0$ ,  $H_s$ , and  $k$  are the ground-based phase speed of an AGW, horizontal background wind velocity (positive eastward), scale height in the ideal atmosphere, and horizontal wavenumber, respectively. If the bracket factor would be replaced by  $m^2$ , then Eq. (1.5) becomes

$$\frac{d^2 \hat{w}}{dz^2} + m^2 \hat{w} = 0. \quad (1.6)$$

If  $m$  is invariant, then

$$\hat{w} = Ce^{imz} + De^{-imz} \quad (1.7)$$

where  $C$  and  $D$  are constants. This equation is the basis of the linear gravity wave theory. If  $m$  is real, Eq. (1.7) shows that the vertical speed of the AGW perturbation varies sinusoidally with the height, with a vertical wave number  $m$ . However, an AGW with a complex  $m$  does not vertically propagate. This is referred to as *external* or *evanescent*.

The Taylor–Goldstein equation (1.5) can be simplified in the case of no background wind.

$$\frac{d^2 \hat{w}}{dz^2} + \left[ \frac{N^2}{c_h^2} - k^2 + \frac{1}{4H_s^2} \right] \hat{w} = 0 \quad (1.8)$$

where the vertical wave number  $m$  is given by

$$m^2 = \frac{N^2}{c_h^2} - k^2 + \frac{1}{4H_s^2}. \quad (1.9)$$

The ground-based horizontal phase speed,  $c_h$ , and the vertical phase speed,  $c_z$ , of AGW are given by

$$c_h = \omega/k, c_z = \omega/m \quad (1.10)$$

where  $\omega$  is the ground-based frequency.

The direction of the phase speed is parallel to the wavenumber vector,  $\mathbf{k} = (k, m)$ .

In case the vertical wavelength is not so long (i.e.,  $m^2 \gg 1/4H_s^2$ ), we obtain the following equation from Eqs (1.9) and (1.10)

$$\omega = \frac{kN}{\sqrt{k^2 + m^2}} = N \cos \beta \quad (1.11)$$

where  $\beta$  is the angle of the wave number vector from the horizontal direction, as illustrated in Fig. 1.4. This equation suggests that AGWs with short periods can propagate more vertically than horizontally.

The group velocity vector,  $\mathbf{c}_{gr}$ , is

$$\mathbf{c}_{gr} = \left( \frac{\partial \omega}{\partial k}, \frac{\partial \omega}{\partial m} \right) = \left( \frac{Nm^2}{(k^2 + m^2)^{3/2}}, \frac{-Nmk}{(k^2 + m^2)^{3/2}} \right). \quad (1.12)$$

Based on the fact that  $\mathbf{k} \cdot \mathbf{c}_{gr} = 0$ , the phase speed of AGW and the group velocity of AGW are perpendicular and their vertical components are always in opposite directions, as shown in Figure 1.4. These are very important characteristics of AGWs. It should be noted that horizontally small-scale AGWs have faster vertical group velocities.

When the background wind is constant, the vertical wave number,  $m$ , is

$$m^2 = \frac{N^2}{(c_h - u_0)^2} - k^2 + \frac{1}{4H_s^2}. \quad (1.13)$$

The intrinsic horizontal phase speed,  $c_{hi}$ , is defined as

$$c_{hi} = c_h - u_0. \quad (1.14)$$

The dispersion relation in Eq. (1.13) shows that if the background wind speed approaches the ground-based phase speed in the same direction, the vertical wave number approaches infinity. In such a case, the horizontal intrinsic phase speed in Eq. (1.14) and the vertical group velocity in Eq. (1.12) become zero. The AGW is unable to propagate vertically across the altitude of the critical level, which is called critical level filtering. This mechanism is one of the important processes causing wave breaking and momentum deposition.

### 1.2.2 AGW Observation and Model Studies

AGWs in the mesosphere are mostly observed by remote sensing techniques such as radio detection and ranging (radar), light detection and ranging (lidar), and airglow imaging. Radar is an active remote sensing technique measuring the wind velocity by detecting the weak backscattering due to refractive index anomalies. Radar can measure the vertical profile of the wind velocity and therefore is used to detect wind velocity perturbations induced by AGWs. The AGW kinetic energy and AGW momentum flux in the troposphere, lower stratosphere, mesosphere, and lower thermosphere can be observed. Lidar is an optical active remote sensing technique in which a laser pulse is transmitted and its backscatter is measured as a function of height. Lidar observations can obtain the temperature profiles and potential energy of AGWs from near the ground to the mesosphere and lower thermosphere. Airglow observation detects faint photochemical luminescence of atoms and molecules in the atmosphere at ~80–120 km height. Airglow imaging observation with a high sensitive camera is useful to investigate the horizontal structure of small-scale (< 100 km) and short-period (< 1 h) AGWs due to its high horizontal and time resolutions, while radar and lidar observations are suitable to obtain the vertical structure of AGWs. These observation techniques have their own characteristics such as time and spatial resolutions, observational coverage, and available spectral ranges of the period and wavelengths of atmospheric waves. It is important to know the capability and limits of these observation techniques and to compare the results obtained with these techniques to

reveal all characteristics of AGWs in the real atmosphere.

Medium Frequency (MF) radar, Mesosphere–Stratosphere–Thermosphere (MST) radar, and meteor radar are used for AGW observations in the mesosphere. An example of a horizontal wind velocity profile measured by MF radar is shown in Figure 1.5. The vertical structure of AGWs can be seen in this figure as downward propagation of phase fronts. *Vincent and Reid* [1983] derived AGW momentum fluxes of AGWs in the mesosphere from MF radar measurement using a partial reflection in Adelaide (35°S, 138°E), Australia, in the period of May 11–14, 1981. They obtained an eastward acceleration of ~20 m/s/day in the mesosphere due to AGWs with a dominant horizontal wavelength of ~50 km and a phase speed of ~50 m/s. The radar observations clarified the spectral characteristics of AGWs and implied that short-period and small-scale AGWs primarily contribute to the momentum transport [e.g., *Vincent*, 1984; *Fritts and Vincent*, 1987]. *Vincent and Fritts* [1987] analyzed the data obtained by the same MF radar in Adelaide between November 1983 and December 1984 and showed that the kinetic energy of AGWs in the mesosphere has a semiannual variation, with maxima in summer and winter and minima in spring and fall, by analyzing the mean square amplitude of the zonal and meridional wind perturbation. The MU radar at Shigaraki (35°N, 136°E), Japan, is a MST radar, which uses Bragg scattering from turbulence and can observe wind velocities in the altitude ranges of 2–24 km and 60–98 km. *Tsuda et al.* [1990] derived the kinetic energy and momentum flux of AGWs based on mesospheric wind data at 60–85 km obtained over three years by the MU radar. *Manson and Meek* [1993] used wind data to derive the momentum flux of AGWs between 58 and 109 km obtained by the MF radar at Saskatoon (52°N, 107°W), Canada. These studies in both hemispheres showed a similar semiannual variation of the kinetic energy and suggested that the background wind in the middle atmosphere affects the AGW energy in the mesosphere. The zonal momentum flux of AGWs showed an annual variation, which was eastward in summer and westward in winter at these three radar stations [*Tsuda et al.*, 1990; *Manson and Meek*, 1993; *Nakamura et al.*, 1993, 1996]. The meteor radar measures the wind profile in the mesosphere and lower thermosphere by using the Fresnel reflection from a meteor trail. *Tsutsumi and Aso* [2005] reported the results of the wind profile between 60–120 km altitudes by the MF radar at Syowa Station, Antarctic, which has both MF and meteor radar modes. Radar observations of

the vertical profile of the wind velocities in the mesosphere have greatly contributed to the understanding of momentum and energy transport by AGWs into the mesosphere, although the wind profile in the upper stratosphere is unavailable.

Various types of lidar techniques are used for the AGW observation for the altitudes from near the ground to the mesosphere and lower thermosphere. Sodium fluorescence backscatter has been used for lidar observations to measure Na density perturbations caused by AGWs between 80–100 km [Blamont *et al.*, 1972; Kirchoff and Clemesha, 1973; Richter and Sechrist, 1979; Juramy *et al.*, 1981]. She *et al.* [1990] observed Na temperature profiles between 82 and 102 km at Ft. Collins (41°N, 105°W), U.S., by using the Doppler-free structure of the sodium D2 fluorescence spectrum. The accuracies of the temperature measurement was better than  $\pm 3$  K with a vertical resolution of 1 km and a time resolution of 5 min at the sodium density peak height. The Na lidar at Ramfjordmoen, Tromsø (70°N, 19°E), Norway, of the research group at Nagoya University used this technique [Tsuda *et al.*, 2011; Takahashi *et al.*, 2015] and observed AGWs based on vertical temperature profiles [Nozawa, *et al.*, 2014; Takahashi *et al.*, 2014]. A Na lidar can also measure wind velocities by using the Doppler shift of backscattering signals [e.g., Liu *et al.*, 2002; Franke *et al.*, 2005]. The first Rayleigh lidar observation to measure the atmospheric density and temperature at an altitude of 30–80 km was performed at the Observatory of Haute-Provence (44°N, 6°E), France [Hauchecorne and Chanin, 1980; Chanin and Hauchecorne, 1981]. Since this observation, Rayleigh lidar observations of AGWs have been carried out at various locations [Gardner *et al.*, 1989; Senft and Gardner, 1991; Whiteway and Carswell, 1994; Gerrard *et al.*, 2000]. It should be noted that the potential energy density of AGWs per unit mass can be derived from the temperature profile observed by a Rayleigh lidar [Wilson *et al.*, 1991]. Yamashita *et al.* [2009] compared the seasonal variation of the potential energy density of AGWs observed by lidar at the South Pole (90°S) and Rothera (68°S, 68°W), Antarctic, at an altitude of 30–45 km. They revealed that the smaller seasonal variation of the potential energy at the South Pole could be explained by the absence of seasonal variations of the AGW source and background wind at the South Pole, which were responsible for critical level filtering. Rauthe *et al.* [2006] performed lidar temperature measurements to derive temperature variations due to AGWs between altitudes of 1 and 105 km using co-located Rayleigh–Mie–Raman

and potassium resonance lidars in Kühlungsborn (54°N, 12°E), Germany, as shown in Figure 1.6. Such a continuous, remote temperature measurement from near the ground to the mesopause is only available using lidar observations.

When AGWs reach the airglow altitude, atmospheric density perturbations induced by AGWs appear in the intensity variations of the airglow [e.g., *Gardner and Taylor, 1998*]. Airglow imaging is a passive remote sensing technique, which allows us to measure horizontal structures of AGWs including the horizontal wavelength, horizontal propagation direction, horizontal ground-based phase speed, and ground-based period. Figure 1.7 shows an example of an airglow image with a wave-like structure induced by AGWs. To record airglow emission, *Peterson and Keiffaber [1973]* carried out an infrared photograph observation for hydroxyl (OH) airglow with an exposure time of 15 min under moonless night sky. The obtained images contained a wave-like structure caused by AGWs of OH airglow. Since the 1990s, imagers with a charged-coupled device (CCD) have been widely used for airglow imaging observations of AGWs in the mesopause [e.g., *Hecht et al., 1993, 1994; Swenson et al., 1995; Taylor et al., 1991a, b, 1995a, b*]. The high spatial and temporal resolutions are quite useful to observe the temporal evolution of AGWs such as AGW breaking events [e.g., *Yamada et al., 2001*]. In recent years, the Advanced Mesospheric Temperature Mapper (AMTM) equipped with an Indium–Gallium–Arsenide (InGaAs) detector has been used to derive the atmospheric temperature from infrared emissions in the mesospheric OH (3,1) band (at  $\sim 1.5 \mu\text{m}$ ) with a rather short exposure time ( $\sim 3\text{s}$ ) [*Pautet et al., 2014; Cai et al., 2014*]. Airglow imaging observations are also adequate to measure a concentric AGW. *Taylor et al. [1988]* observed a concentric AGW using a low-light TV system on August 14, 1980, at the Gornergrat Observatory (46°N, 7.8°E), Switzerland. They identified a thunderstorm as the source of the AGWs based on the consistency between the center of the concentric AGW and lightning activity. Other airglow imaging observations of concentric AGWs were performed by ground-based [*Suzuki et al., 2007a, 2013a; Yue et al., 2009*] and space-borne [e.g., *Perwitasari et al., 2015*] observations. It should be noted that well-automated airglow imagers that require little electric power could be easily used at multiple sites worldwide. With respect to the mid-latitude, it has been suggested that critical level filtering by strong background wind affects the horizontal phase velocity distribution, which means that AGWs propagating towards the same

directions with the background winds are less frequently observed [e.g., *Nakamura et al.*, 1999; *Walterscheid et al.*, 1999; *Hecht et al.*, 2001; *Ejiri et al.*, 2003; *Dou et al.*, 2010; *Kim et al.*, 2010; *Q. Li et al.*, 2011]. With respect to the low latitude, it is reported that the distribution of the generation source of AGWs mainly affects the phase velocity distributions of AGWs due to the weak background winds near the equator [e.g., *Suzuki et al.*, 2004, 2009a; *Medeiros et al.*, 2005; *Taylor et al.*, 1997; *Zhenhua Li et al.*, 2011]. However, airglow observations at higher latitude are not as abundant as at mid and low latitudes [*Espy et al.*, 2004, 2006; *Nielsen et al.*, 2009, 2012; *Bageston et al.*, 2009; *Suzuki et al.*, 2011].

Space-borne observations of AGWs have been performed by satellites such as the Aqua/Atmospheric Infrared Sounder (Aqua/AIRS), International Space Station-Ionosphere, Mesosphere, upper Atmosphere, and Plasmasphere/Visible and near-Infrared Spectral Imager (ISS-IMAP/VISI), and Suomi National Polar-orbiting Partnership/Day/Night Band (Suomi NPP/DNB). The AIRS [*Aumann et al.*, 2003] aboard Aqua launched by the National Aeronautics and Space Administration (NASA) into a sun-synchronous polar orbit with 98° inclination on May 4, 2002, can derive the atmospheric temperature in the stratosphere by measuring the radiation of atmospheric constituents. Its horizontal resolution is  $13.5 \times 13.5 \text{ km}^2$  at nadir and  $41 \times 21.4 \text{ km}^2$  at the scan extremes. *Hoffman et al.* [2013] showed the global distribution of AGW occurrence frequencies for different seasons during daytime and nighttime. The ISS-IMAP/VISI [*Sakanoi et al.*, 2011] is a space-borne airglow imager, which can detect mesospheric AGWs. It has two field-of-views pointing 45° forward and 45° backward to nadir and covers a width of ~600 km at the mesopause with a horizontal resolution of ~10 km. The ISS-IMAP/VISI contributed to the investigation of the global distribution of a concentric AGW, which could horizontally propagate up to ~1400–1500 km and be likely ducted [*Perwitasari et al.*, 2015]. The Suomi NPP/DNB [*Miller et al.*, 2015] can also measure airglow emission in the mesosphere. *Yue et al.* [2014] reported the simultaneous observation of concentric AGWs from space using Suomi/DNB and Aqua/AIRS and provided the three-dimensional structure of AGW propagation. The satellite airglow imaging observation provides a global view of AGWs by moving relatively to the Earth's surface, although the ground-based airglow imaging observation is suitable for a continuous observation at a specified point.

Theoretical studies and numerical simulations of AGWs have been widely performed [see the review in *Fritts and Alexander, 2003*]. Here, we select and introduce studies of secondary AGW generation by 3-D body forcing via AGW breaking. Horizontal body forces due to horizontal momentum deposition of AGWs can accelerate horizontal mean wind in the AGW propagating direction [e.g., *Fritts and Alexander, 2003*]. *Holton and Alexander [1999]* simulated convectively generated AGWs propagating toward the mesosphere by using a two-dimensional model and showed that the breaking of these AGWs generated secondary AGWs. They also showed power spectra of the vertical wind velocity as function of the horizontal wavelength, ground-based period, and zonal phase speed for upgoing and downgoing waves at the altitudes of 60–70 km (Figure 1.8). The down-going AGWs with a shorter period ( $< 10$  min) and a shorter horizontal wavelength (15–25 km) had a spectral density similar to the up-going AGWs, although the spectral power of the down-going AGWs with longer periods and longer wavelengths was much smaller than that of the up-going AGWs. *Satomura and Sato [1999]* found that small-scale AGWs are generated in association with the breaking of AGWs (excited by mountains) in the stratosphere based on a two-dimensional model simulation. *Vadas et al. [2003]* examined, whether the properties of secondary AGWs and their momentum fluxes depend on the spatial and temporal scales of a body force by using a linear formulation of the atmospheric response [*Vadas and Fritts, 2001*]. They showed that secondary AGWs radiated symmetrically along the direction of the body force. Deep, horizontally localized and temporally restricted body forces likely generate AGWs with high intrinsic frequencies. They applied the formulation to the AGW breaking event, which was numerically investigated by *Holton and Alexander [1999]* and concluded that highly localized body forces might excite some of the observed secondary waves with both low and high frequencies.

One of the major problems of AGWs is the gravity wave parameterization of the momentum transport in a numerical model. While momentum transport by AGWs is quite important for the global circulation, it is difficult to reproduce AGWs directly in a global numerical model due to their limited spatiotemporal resolutions. Therefore, the parameterization of momentum transport of AGWs is needed. The AGWs generated by orographic sources, which have zero phase speed (relative to the ground), are parameterized in many general circulation models (GCMs) [e.g., *Palmer et al., 1986*;

*McFarlane, 1987; Miller et al. 1989*]. However, *Fritts and Alexander [2003]* pointed out that the properties of non-stationary AGWs and their sources were not well understood. They emphasized the importance of an accurate parameterization, which is capable of quantifying non-stationary AGW intermittency imposed by variable sources and propagation conditions. *Geller et al. [2013]* suggested that the usage of different parameterization schemes could be one of the reasons for the inconsistency among the results from different GCM studies. Figure 1.9 shows the zonal mean absolute momentum fluxes at an altitude of 50 km from different GCM studies. The magnitudes of the momentum fluxes of polar regions are larger in the Antarctic winter than in the Arctic winter. The difference among the momentum fluxes of the four models is also larger in the Antarctic winter. Because the AGWs at this altitude can reach the mesopause through their vertical propagation, the large difference of the momentum flux and its deposition should be basically similar in the mesosphere and mesopause. This result suggests that it is necessary to precisely quantify the AGW momentum transport by observations and to constrain the AGW parameterization in the GCM; hence, the importance of the quantitative analysis and characterization of AGWs is stressed.

## Chapter 2

# Airglow Imaging Observation of Atmospheric Gravity Waves

### 2.1 Mesospheric Airglow

Mesospheric airglows are atmospheric emissions of atoms and molecules at different peak altitudes with a vertical thickness of  $\sim 10$  km. The major mesospheric airglow emissions are the hydroxyl (OH) Meinel bands, sodium D (NaD) lines, oxygen molecular ( $O_2$ ) atmospheric bands, and atomic oxygen (OI) green lines. Here, we introduce OH and Na airglow emissions, which are used in this study. The emission mechanisms are summarized as follows [e.g., *Krasovskij and Šefov, 1965; Chamberlain, 1995*].

OH Meinel airglow at the broad wavelength range of 550 nm–4.4  $\mu\text{m}$  is emitted at  $\sim 87$  km by hydroxyl radicals. The following reactions were proposed by *Bates and Nicolet [1950]*:



The wavelength of the emission in reaction (2.2) depends on the vibrational and rotational level difference between  $OH^*$  and  $OH^{**}$ . This is the reason that the OH Meinel airglow wavelengths are band structures.

Sodium airglow is emitted at an altitude of  $\sim 90$  km by the relaxation of the energy level from  $Na(^2P)$  to  $Na(^2S)$  with the optical wavelength of 589.0 and 589.6

nm. Na(<sup>2</sup>P) is produced by the following reactions.



*Swenson and Gardner* [1998] developed an analytic model, which treated the OH and Na airglow intensity perturbation caused by AGWs. The volume emission rate of the OH (8,3) Meinel Band can be expressed with Eq. (6) described by *Swenson and Gardner* [1998]

$$V_{OH} = \frac{(8.25 \times 10^{-36} \text{cm}^6 \text{s}^{-1})[\text{O}][\text{O}_2]^2(200/T)^2}{(1 + 7.7 \times 10^{-14} \text{cm}^3[\text{O}_2])} [\text{number} \cdot \text{cm}^{-3} \cdot \text{s}^{-1}]. \quad (2.5)$$

This formula shows that the OH emission intensity depends on the atomic oxygen density, molecular oxygen density, and temperature. It should be noted that the density profile of the oxygen atom in the mesosphere is different from the atmospheric density profile, as shown in Figure 2.1. Based on Eqs (29) and (31) described in *Swenson and Gardner* [1998], the relative OH airglow intensity perturbation  $\Delta V_{OH}/\bar{V}_{OH}$  can be described as follows:

$$\frac{\Delta V_{OH}}{\bar{V}_{OH}} \approx -3 \left[ 1 - \frac{z - z_{OH}}{h_{OH}} + \frac{(z - z_{OH})^2}{\sigma^2} \right] \frac{\Delta \rho}{\bar{\rho}} \quad (2.6)$$

where  $\Delta \rho/\bar{\rho}$  is the relative atmospheric density perturbation,  $z$  is the altitude,  $z_{OH}$  is the centroid altitude of the OH airglow emission,  $h_{OH} \approx 3.6$  km, and  $\sigma \approx 8.0$  km. For ground-based observations, airglow emission is observed as the column emission integrated along the line-of-sight. Based on Eq. (33), Krassovsky's ratio is defined as the ratio between the square of the total relative OH intensity perturbation normalized by the OH intensity,  $\left(\frac{\Delta I}{I}\right)^2$ , and the square of the relative temperature perturbation normalized by the temperature,  $\left(\frac{\Delta T}{T}\right)^2$ , as follows:

$$\eta^2 = \left(\frac{\Delta I}{I}\right)^2 / \left(\frac{\Delta T}{T}\right)^2 \quad (2.7)$$

Based on Eqs (A2) and (A3), the relative Na airglow intensity perturbation,  $\Delta V_{Na}/\bar{V}_{Na}$ , can be described in the same way as the relative OH airglow intensity perturbation,

$$\frac{\Delta V_{Na}}{\bar{V}_{Na}} \approx -\frac{1}{(\gamma - 1)} \left[ 1 - \frac{z - z_{Na}}{h_{Na}} \right] \frac{\Delta \rho}{\bar{\rho}} \quad (2.8)$$

where  $\gamma = 1.4$  is the ratio of the specific heat,  $z_{Na}$  is the centroid altitude of the Na airglow emission, and  $h_{Na} \approx 2.5$  km. These equations show that the relative amplitude of the Na and OH airglow intensity perturbation is proportional to the relative atmospheric density perturbation induced by AGWs.

## 2.2 Airglow Imaging Observation

As described previously, the atmospheric density perturbation induced by AGWs is reflected in the airglow intensity fluctuation. *Krassovsky* [1972] first reported that the oscillation of the intensity and the rotational temperature of OH airglow indicate the period and the phase speed similar to those expected from the internal acoustic-gravity wave theory. Early studies of the wave-like feature in the horizontal structure of the airglow caused by AGWs were performed using photographs [*Peterson and Kieffaber*, 1973; *Morreles and Herse*, 1977; *Peterson*, 1979] and TV cameras [*Crawford et al.*, 1975, 1978; *Rothwell et al.*, 1976]. A modern imaging device, a cooled CCD, has been widely used for airglow imaging measurements of AGWs since *Taylor and Hill* [1991] who reported imaging observations during the ALOHA-90 campaign in 1990. In recent years, an InGaAs detector has been used to observe infrared emissions in the mesospheric OH (3,1) band (at  $\sim 1.5$   $\mu\text{m}$ ) [*Pautet et al.*, 2014; *Cai et al.*, 2014].

Here, we introduce the blocking diagram used by *Taylor et al.* [1993]. This is useful to investigate the critical level filtering effect on the vertical propagation of AGWs observed by airglow imaging. Using Eq. (1.10), the intrinsic frequency,  $\Omega$ , can be described as

$$\Omega = \omega - ku_0 = \omega - \omega \frac{u_0}{c_h} \quad (2.9)$$

In the two-dimensional horizontal plane (x, y) with x in the zonal direction and y in the meridional direction, the intrinsic frequency can be expressed as [Taylor et al. 1993]

$$\Omega = \omega - \omega \frac{u_{0x} \cos \phi + v_{0x} \sin \phi}{c_h} \quad (2.10)$$

where  $u_{0x}$  is the zonal wind speed;  $v_{0x}$  is the meridional wind velocity; and  $\phi$  is the azimuth of the horizontal propagation direction, clockwise measured northward. It should be noted that we could use the same  $\Omega$ ,  $\omega$  and  $c_h$  in both the two dimensions used in Subsection 1.2.1 and three-dimensional horizontal plane. Critical level filtering occurs when the component of the background wind speed along the horizontal propagation direction of an AGW equals the horizontal phase speed. In this case, the intrinsic frequency becomes zero. Figure 2.2 is an example of the blocking; the shaded area corresponds to the forbidden regions defined by  $\Omega \leq 0$  at some height below the airglow altitude for each propagation direction and phase speed.

In the past two decades, airglow-imaging observations have been performed and contributed to the understanding of mesospheric AGWs. At the mid-latitude, many studies of AGWs observed by airglow imaging have been performed [e.g., Nakamura et al., 1999; Walterscheid et al., 1999; Hecht et al., 2001; Ejiri et al., 2003; Dou et al., 2010; Kim et al., 2010; Q. Li et al., 2011]. Figure 2.2 shows a profile of the horizontal wind velocities and a polar plot of the phase velocity distribution, with phase speed as the radius and propagation direction as the azimuth. The blocking diagram is overlain in Figure 2.2(b) as the shaded area using the horizontal wind profile and assuming that the AGWs are generated at the ground and reach the observation altitude. The AGWs with phase velocities corresponding to the shaded area cannot reach the observation altitude because of critical level filtering. Taylor et al. [1993] used the blocking diagram to show the effect of critical level filtering on the phase velocity distribution of AGWs. The observed AGWs had phase velocities outside of the shaded area in the blocking diagram. Their result suggested that airglow-imaging observations are useful to

investigate the effect of the critical level filtering on the vertical propagation of mesospheric AGWs. *Nakamura et al.* [1999] performed a statistical study of the horizontal propagation directions of AGWs observed by airglow imagers in Shigaraki, Japan, for 18 months. There was a clear seasonal variation of the dominant propagation direction, with eastward directions in summer and westward directions in winter. These preferential directions are consistent with the critical level filtering by background wind in the middle atmosphere. *Walterscheid et al.* [1999] showed the distribution of the propagation direction of quasi-monochromatic AGWs observed over Adelaide, which was mainly southward in summer and northward in winter. They suggested that the meridional anisotropy in summer could be explained by thermal duct, which allows AGWs to propagate over a long distance by trapping them between two evanescent layers or between an evanescent layer and the ground. *Ejiri et al.* [2003] compared the characteristics of AGWs observed at two stations, Rikubetsu (44°N, 144°E) and Shigaraki (35°N, 136°E), Japan. The AGWs at both stations propagated northward and northeastward in summer and generally westward in winter. They suggested that the meridional propagation might be explained by thermal ducting, except for the northward propagation in Rikubetsu, Japan. Previous studies showed that the propagation characteristics of AGWs and their seasonal variation in the mid-latitude could be affected by critical level filtering in zonal direction and ducting in meridional direction. *Suzuki et al.* [2013b] used the data observed by four identical imagers of the Optical Mesosphere Thermosphere Imagers (OMTI) at Rikubetsu, Sakata (39°N, 140°E), Shigaraki, and Sata (31°N, 131°E) in Japan. They presented a coherent AGW structure with a spatial extent larger than 1800 km measured simultaneously by the four imagers and suggested that this AGW was ducted at airglow altitude.

At low-latitude, airglow imaging measurements of AGWs have also been performed [e.g., *Nakamura et al.*, 2003; *Suzuki et al.*, 2004, 2009a; *Medeiros et al.*, 2005; *Taylor et al.*, 1997; *Li et al.*, 2011]. *Nakamura et al.* [2003] compared the horizontal phase velocity distribution of AGWs observed by airglow imagers at Tanjungsari (108°W, 6.9°S), Indonesia, with distributions of tropospheric clouds estimated by the Geostationary Meteorological Satellite from September 2000 to September 2001. They found that high-altitude clouds were located opposite to the propagation direction of AGWs and critical level filtering was not effective because of weak background wind at

low latitudes. *Medeiros et al.* [2005] carried out airglow imaging observations at three stations, Cachoeira Paulista (23°S, 45°W) in 1999, São João do Cariri (7.5°S, 37°W) in 2001, and Boa Vista (2.8°N, 61°W) in Brazil. They compared the distributions of the AGW propagation direction and lightning activity and concluded that the generation source of the AGWs, which was thought to be tropospheric convective activity, existed in South America during October–December. The distributions of the AGW propagation direction at low latitudes are mainly influenced by the source distribution because of weak wind in the middle atmosphere (Figure 1.3); the AGWs are mainly generated by tropospheric convectivity.

Airglow imaging observations at high latitudes are few and the AGW propagation process and generation mechanism are not clearly understood. *Espy et al.* [2004] derived the momentum flux of AGWs based on a sodium airglow imaging observation over Halley Station (76°S, 27°W) in the Antarctic. The net zonal momentum flux in winter was estimated to be  $4.4 \text{ m}^2\text{s}^{-2}$  on average in westward direction and the meridional momentum flux is  $0.5 \text{ m}^2\text{s}^{-2}$  on average in northward direction. These momentum fluxes are smaller than the wintertime momentum flux at mid-latitude, with a magnitude of  $20 \text{ m}^2\text{s}^{-2}$  and  $12 \text{ m}^2\text{s}^{-2}$  in the westward and northward directions, respectively [*Tang et al.*, 2002]. They showed a large day-to-day variability of the momentum flux with rotation from the northwest to the southeast throughout the winter season, corresponding to background wind variation. However, they did not present the horizontal phase velocity distributions of the observed AGWs. *Bageston et al.* [2009] reported a statistical study of OH airglow imaging observations at the Comandante Ferraz Antarctica Station (62°S, 58°W) over six months from April to October 2007. The phase velocity distribution of the observed AGWs showed that phase speeds of westward-propagating AGWs were up to 40 m/s and the phase speeds of eastward-propagating AGWs reached 120 m/s. This zonal anisotropy could not be noted in observations at mid–low latitudes (Figure 2.3). *Nielsen et al.* [2009] presented a climatological study of AGWs observed by airglow imaging over Halley Station in 2000 and 2001 (Figure 2.4). The phase velocity distribution of AGWs included faster eastward-propagating AGWs and slower westward-propagating AGWs, similar to the result of *Bageston et al.* [2009]. They pointed out that critical level filtering could partly explain the zonal anisotropy of the phase velocity distribution because the AGWs were

observed in the shaded area of the blocking diagram in Figure 2.4. *Suzuki et al.* [2011] reported statistical characteristics of AGWs observed by the airglow imager at the South Pole (90°S). They showed preferential directions (30°E–60°E and 210°E–240°E), although the reason for such preferential directions is not clear. For the Arctic, *Suzuki et al.* [2009b] reported statistical characteristics of AGWs at Resolute Bay during the winter seasons of 2005 and 2006. They extracted small-scale (< 100 km) and larger scale (> 100 km) AGWs. The preferential propagation directions of both AGWs were westward.

As described above, airglow imaging observations have been performed worldwide. These observations could contribute to the clarification of the geographical dependence of AGWs. However, the quantitative comparison of the results derived from airglow imaging observations is difficult due to problems in the analysis method of airglow imaging data, as described in the next section.

## 2.3 Analysis Method for Airglow Imaging Data

Analysis methods for airglow imaging data have been developed over the past three decades. *Hapgood and Taylor* [1982] developed a method to quantify the horizontal propagation parameters of AGWs from airglow images by fitting a set of circles to structures in airglow images. This method has been used in many studies [e.g., *Taylor and Hapgood*, 1988; *Taylor et al.*, 1997]. Traditionally, the statistics of these observations are based on the wave characteristics of individual AGW events, which are detected by visual inspection of outstanding wave-like structures in airglow image data. A keogram, which is created from the central column or row of each time sequential image, such as Figure 2.5, has been used to investigate large-scale AGWs in airglow images. However, such methods are not suitable for analyzing large amounts of data obtained by network observations such as the OMTI for several reasons: (1) the analysis procedure is time-consuming, (2) differences exist in the criteria for the determination of wave events, and (3) the extraction of AGW parameters depends on the work of the people processing the data. The latter two reasons might induce biases in the statistical analysis of wave events.

Power spectral analysis is another statistical method that is frequently used for time

series of data and is applicable to image data. *Hecht et al.* [1994] applied 2-D spectral analysis to airglow imaging data to obtain horizontal wave number spectra of airglow intensity variations. The field of view of their imager is approximately  $100 \times 100 \text{ km}^2$ . *Garcia et al.* [1997] further applied a 2-D Fourier analysis technique to all-sky images of the airglow by determining the imager's attitude using stars, star removal, geographic projection, re-gridding, and flat fielding of the data before the spectral analysis. However, 2-D Fourier analysis can derive only a 2-D horizontal wavenumber spectrum, which determines the horizontal propagation direction of AGWs with  $180^\circ$  ambiguities. *Coble et al.* [1998] developed an analysis technique by using a 3-D fast Fourier transform (FFT) to obtain an unambiguous 2-D spectrum, as shown in Figure 2.5, which contains information on the unambiguous zonal and meridional wavenumbers and has been applied to various airglow imaging datasets [e.g., *Nakamura et al.*, 2001; *Tang et al.*, 2002; *Espy et al.*, 2004]. Spectral analysis can efficiently deal with a large amount of airglow data and consider duration, spatial extent, and magnitude of AGWs independent of work of the people processing the data to determine AGW events and extract AGW characteristics. However, information about the horizontal phase velocity is not notable in the unambiguous 2-D spectrum in the horizontal wavenumber and frequency domain. *Suzuki et al.* [2007b] used spectral analysis for the extraction of AGW events by detecting a peak of power spectrum in the horizontal wavenumber domain. The AGW events could be extracted without human bias, although the duration, spatial extent, and magnitude of AGWs were insufficiently considered.

## 2.4 Antarctic Airglow Imaging Network and Other Data

The Antarctic Gravity Wave Imaging/Instrument Network (ANGWIN), an international observation network among Antarctic stations commenced in 2011, is aimed at investigating AGWs over the Antarctic region by Japan, the United States, the United Kingdom, Australia, and Brazil. The ANGWIN includes airglow imagers installed at Syowa ( $69^\circ\text{S}$ ,  $40^\circ\text{E}$ ), Davis ( $69^\circ\text{S}$ ,  $78^\circ\text{E}$ ), McMurdo ( $78^\circ\text{S}$ ,  $167^\circ\text{E}$ ), Halley, Rothera ( $68^\circ\text{S}$ ,  $68^\circ\text{W}$ ), the South Pole ( $90^\circ\text{S}$ ), and Comandante Ferraz ( $62^\circ\text{S}$ ,  $58^\circ\text{W}$ ), as shown in Figure 2.6.

In this thesis, we used data observed by the imagers at Syowa, Davis, Halley, and McMurdo and wind data from MF radars at Syowa and Davis. The MF radar measures the horizontal wind velocity at 70–100 km by estimating the horizontal drift speed of the weakly ionized atmosphere from a lag among the signals detected with horizontally spaced antennas. The Modern Era-Retrospective Analysis for Research and Applications (MERRA) [*Rienecker et al.*, 2011] is an assimilated numerical model for the reanalysis of data combined with various observation results and is used in this study. The wind and temperature are provided in a  $288 \times 144$  grid with  $1.25^\circ$  longitude and  $1.25^\circ$  latitude resolution, 42 pressure levels, and a temporal resolution of 3 h.

## 2.5 Purpose and Outline of This Thesis

The AGW plays an important role in the vertical coupling of the atmosphere through transport of significant amounts of energy and horizontal momentum into the mesosphere and lower thermosphere. While momentum transport by AGWs is quite important to global circulation, it is difficult to directly reproduce AGWs in a numerical model due to the limited time. Therefore, the precise parameterization of momentum transport of AGWs based on global observation is required. Although airglow-imaging observations have been performed at mid- and low- latitudes, those in the Antarctic are few. The analysis method currently used for airglow imaging data restricts the quantitative comparison of the results.

The purpose of this thesis is to reveal the characteristics of mesospheric AGWs over Syowa and quantitatively investigate differences among the characteristics of AGW phase velocity distributions over the ANGWIN stations focusing on critical level filtering. This study was performed in two steps.

In the first step, we developed a new spectral analysis method to obtain power spectra of the airglow intensity variation in the horizontal phase velocity domain (hereafter referred to as phase velocity spectra) from a series of airglow images by expanding the 3-D analysis described in *Coble et al.* [1998]. This method was suitable for dealing with a large amount of airglow data without the biases of the visual inspection of AGW

events. We applied the spectral analysis to the airglow imaging data obtained at Syowa Station in the Antarctic during the 2011 observation season. This dataset was also analyzed by conventional event analysis (hereafter referred to as event analysis). The results derived from both spectral and event analyses are compared in detail in Chapter 3.

In the second step, we applied the new spectral analysis method to data from the ANGWIN imagers at Syowa, Halley, Davis, and McMurdo between April 6 and May 21, 2013. We showed day-to-day and station-to-station variations at McMurdo and Halley on April 10 and 11, 2013, and averaged spectra of the four stations during the observation period. The phase velocity spectra at Davis and Syowa were compared with background wind from MF radars and MERRA to investigate the AGW generation and propagation processes. In addition, temporal variations during one night and the frequency dependency of the phase velocity spectrum were also investigated.

## Chapter 3

# New Statistical Analysis of Gravity Waves Observed by Airglow Imaging

We developed a new analysis method to obtain the power spectrum in the horizontal phase velocity domain from airglow intensity image data to study AGWs. This method can deal with extensive amounts of imaging data obtained in different years and at various observation sites without biases such as those caused by different event extraction criteria by the person processing the data. The new method was applied to sodium airglow data obtained in 2011 at Syowa Station (69°S, 40°E) in the Antarctic. The results were compared with those obtained from conventional event analysis in which the phase fronts were manually traced to estimate horizontal characteristics such as the wavelengths, phase velocities, and wave periods. The horizontal phase velocity of each wave event in the airglow images corresponds closely to a peak in the spectrum. Both methods produce similar statistical results with respect to the directionality of AGWs. The galactic contamination of the spectrum was examined by calculating the apparent velocity of the stars and found to be limited for phase speeds  $< 30$  m/s. In conclusion, our new method is suitable for deriving the horizontal phase velocity characteristics of AGWs from an extensive amount of imaging data without the biases that are caused by different event extraction criteria by the person processing the data.

## 3.1 Observation

An airglow imager was operated by JARE at the Syowa Station in the Antarctic in 2002 and from 2008 to the present. Here, the data obtained in 2011 by the 52nd JARE were used for analysis. The imager used in 2011 (Figure 3.1) is a part of the OMTIs network [Shiokawa *et al.*, 1999] owned by Nagoya University. The system consists of a fish-eye lens (FL = 24 mm and an aperture of f/4.0) with a field of view (FOV) of 180°, a telecentric lens system, multiple interference filters, and a cooled-CCD camera with a resolution of  $512 \times 512$  pixels. Details of the imaging system are described in Shiokawa *et al.* [2000]. In 2011, airglow- imaging observations were carried out from March 5 to September 30 on 133 nights of which 66 nights exhibited clear skies. The NaD, OH, and OI (630 nm) airglow was observed sequentially by changing the filters using a rotating filter wheel system. Furthermore, background sky images at 572.5 nm were acquired every 30 min. In this study, we used the images of the sodium airglow emission at 589.3 nm because the sodium emission is the least sensitive to auroral contamination [Espy *et al.*, 2004]. The spatial resolution of the sodium image is 0.25 km at the zenith and 2.0 km 30° above the horizon. The exposure time was set to 100 s or 105 s for the Na image and the cadence was 3 min. Hereafter, the observation time of an image is indicated by the time of the beginning of the exposure.

## 3.2 Analysis Methods

In this section, we describe the methods used to obtain the phase velocity spectrum by spectral analysis. The method of deriving the phase velocity distribution by event analysis is also explained and the results are compared with those obtained from the spectral analysis.

### 3.2.1 Spectral Analysis

To obtain the phase velocity spectrum from a series of airglow images, we used several processes including 3-D FFT and coordinate conversion from the horizontal wave number domain to the horizontal phase velocity domain. In this study, Na images excluding background sky images are treated as sequential images; the gaps due to background sky images are ignored. Although it is not the best way, we preferred the computation speed.

Before computing the 3-D FFT of the airglow images, several corrections to the airglow images were made. First, we removed stars from the raw images, as shown in Figure 3.2a, by detecting spike-like structures, as described previously [e.g., *Suzuki et al.*, 2007b]. To remove stars, a median filter with a window size of  $21 \times 21$  pixels was applied to the raw images. The raw brightness count was then replaced by the corresponding count of the median image if the former was larger than the latter by more than 100 counts, where a typical airglow image count including background sky brightness was  $\sim 1000$  counts. Second, we removed the dark counts and offset values of the CCD, which were estimated in the areas near the four corners of the raw images outside the FOV. Third, the image of sodium airglow emission,  $I_{Na}$ , was calculated using the following equation:

$$I_{Na} = I_{raw} - I_{background} \quad (3.1)$$

where  $I_{raw}$  are the raw images after star removal, subtraction of the dark counts, and offset values of the CCD and  $I_{background}$  is the image of the background sky brightness obtained by averaging all images at 572.5 nm acquired every 30 min through the time window and over all azimuthal directions ( $0^\circ$ – $360^\circ$ ). This type of averaging was applied to the images after star removal. The image of the normalized Na perturbation,  $I'_{Na}/\overline{I_{Na}}$ , is calculated as follows:

$$\frac{I'_{Na}}{\overline{I_{Na}}} = \frac{I_{Na} - \overline{I_{Na}}}{\overline{I_{Na}}} = \frac{I_{raw} - \overline{I_{raw}}}{\overline{I_{raw}} - I_{background}} \quad (3.2)$$

where  $\overline{I_{Na}}$  and  $\overline{I_{raw}}$  denote the temporal mean sodium and raw image, respectively, for each time window. The Na airglow perturbation images are then projected and

interpolated onto the geographic coordinate with a size of  $400 \times 400 \text{ km}^2$  using the nearest neighborhood method, assuming that the sodium airglow height is constant. The positions of the stars in the original images are used to calibrate the orientation of the imager. The height of the sodium airglow emission layer is assumed to be 90 km in the present analysis. One pixel in the projected image represents  $1 \times 1 \text{ km}^2$  in geographic coordinates; an image is composed of 160,000 pixels. The detrended image was then calculated by deviation from a plane fitted to the projected image, as shown in Figure 3.2b. Next, the 2-D pre-whitening filter introduced by *Coble et al.* [1998] was applied to each image to reduce the contamination of the higher wave numbers by the side lobes of the large spectral densities at small wave numbers resulting from the data window function of the finite horizontal sampling area. A 2-D Hanning window with a full width of 400 pixels was then applied to each projected image to avoid discontinuity, which might occur when zero-padding extension is performed. A temporal Hanning window is not used to avoid the loss of information contained in a series of airglow images rather than temporal discontinuity. To obtain AGW spectra with higher spatial and temporal wavenumber sampling, the image series, which typically contained 40 images, was implanted at the center of the blank images with a size of  $1024 \text{ pixels} \times 1024 \text{ pixels} \times 256 \text{ images}$ , as shown in Figure 3.2c.

After these preprocessing steps, the phase velocity power spectrum was obtained using the following steps. First, the three-dimensional spectrum as a function of observed frequency,  $\omega$ , zonal wave number,  $k$ , and meridional wave number,  $l$  [hereafter  $(k, l, \omega)$  spectrum] was computed using the 3-D FFT from the image series. This spectrum was recolored using the division by the square of the transfer function of the spatial pre-whitening filter. Figures 3.2d–f show the recolored  $(k, l, \omega)$  spectra of the 21 airglow images observed between 23:00:00 and 24:06:00UT on September 20, 2011, for three selected frequencies at  $1/8$ ,  $1/16$ , and  $1/64 \text{ min}^{-1}$ . Next, the part of the recolored  $(k, l, \omega)$  spectrum corresponding to the range of interest, which means a horizontal wavelengths ranging from 5 to 100 km and periods from 8 to 64 min, was converted into a power spectrum in the  $v_x$ ,  $v_y$ , and  $\omega$  domains [hereafter the  $(v_x, v_y, \omega)$  spectrum], where  $v_x$  and  $v_y$  are the zonal and meridional components of the horizontal phase velocity, respectively. The relationship between these coordinates is given by

$$v_x = \frac{\omega k}{k^2 + l^2} \quad (3.3)$$

$$v_y = \frac{\omega l}{k^2 + l^2}. \quad (3.4)$$

For the conversion, the volume element in the  $v_x$ ,  $v_y$ , and  $\omega$  domains  $dv_x dv_y d\omega$  is given by

$$dv_x dv_y d\omega = J \cdot dk dl d\omega, \quad (3.5)$$

where

$$J = \begin{vmatrix} \frac{\partial v_x}{\partial k} & \frac{\partial v_x}{\partial l} & \frac{\partial v_x}{\partial \omega} \\ \frac{\partial v_y}{\partial k} & \frac{\partial v_y}{\partial l} & \frac{\partial v_y}{\partial \omega} \\ 0 & 0 & 1 \end{vmatrix}, \quad (3.6)$$

is the Jacobian determinant. Figures 3.2g–i show the  $(v_x, v_y, \omega)$  power spectra converted from the  $(k, l, \omega)$  spectra, where Figures 3.2g–i correspond to the cross sections at the periods of 8, 16, 64 min (frequency = 1/8, 1/16, 1/64 min<sup>-1</sup>), respectively. Finally, the  $(v_x, v_y, \omega)$  spectrum is integrated in the frequency domain from 1/8 to 1/64 min<sup>-1</sup> and a 2-D power spectrum in the  $v_x$  and  $v_y$  domains is obtained, as shown in Figure 3.2j. The velocity resolution depends on the frequency of interest and the size of the time window and ranges from 0.017 m/s to 28 m/s in case of a 2-h window, for example.

The temporal data window encompassing the selected airglow images for these spectra was determined using the following two conditions. First, a data window had to include more than 20 successive airglow images without cloud or aurora contamination. Second, the AGW events mentioned in the Subsection 3.2.2 had to be included in the data window for comparison with the results of the event analysis. For the statistical analysis presented in Subsection 3.3.2, a different set of data windows was selected to satisfy only the first condition.

### 3.2.2 Event Analysis

Figures 3.3a and b show examples of images obtained at 23:24 and at 23:51UT on September, 2011, after performing the projection process onto the geographic coordinates in the same way as in the spectral analysis. Note that Figure 3.3a is the same image as shown in Figure 3.2b but plotted for a larger area. First, we investigated a series of images that showed wave-like structures in the airglow intensity, which could be considered to be an AGW packet. Next, we selected two images in which the wavefronts of the AGW could be clearly distinguished, as shown in Figure 3.3. Then, five dots were marked on each of the two consecutive AGW wavefronts (Figure 3.3a). For one of the two phase fronts, a straight line (line A) was fitted to five dots by a least squares fit. The mean distance between line A and the dots on the wavefront B was calculated and considered to be the horizontal wavelength. In Figure 3.3b, the wavefront A moved to the position indicated by C. The five dots on wavefront C were also sampled and the mean distance from the line A was regarded as the distance of the wave propagation during the time interval between the two images. The phase speed was determined from the distance and elapsed time between exposures and the propagation direction was determined to be perpendicular to line A without 180-° ambiguity. The error of the event analysis was estimated to be ~2 m/s. In a time series of images in Figure 3.3a, two phase velocities were calculated for the two independent wave events. These are the events mentioned above, with phase lines A and B, and another event indicated by a white ellipse in Figure 3.3a. The two phase velocities are shown in Figure 3.2j by the white dots with solid black lines.

Event analyses were performed on all data without aurora and clouds obtained at Syowa in 2011; 80 wave events were detected in total. Figure 3.4 shows the distribution of the AGW parameters estimated for the 80 events. The duration of each event ranges from 18 min to 5 h. The horizontal wavelengths displayed in Figure 3.4a were distributed between 10 and 60 km; ~80% of the waves had horizontal wavelengths between 20 and 40 km. Figure 3.4b indicates that the phase speed ranged from 0 m/s to 150 m/s; ~70% of the waves had phase speeds between 0 and 60 m/s. The observed period in Figure 3.4c varied between 3 and 240 min and was shorter than 45 min for 93% of the waves. Twenty-four events have observed periods shorter than 8 min, which is the lower limit for the spectral analysis. Figure 3.4d shows that 66% of the waves propagated

southward or westward (azimuth between  $135^\circ$  and  $315^\circ$ ). The distributions of the horizontal wavelength, phase speed, and observed period are generally consistent with the results of previous studies at high latitudes [e.g., *Nielsen et al.*, 2009; *Bageston et al.*, 2009; *Suzuki et al.*, 2009b, 2011] and mid- to low- latitudes [e.g., *Wrasse et al.*, 2006].

### 3.3 Results and Discussion

In this section, we present and compare the results of the spectral and event analyses for four data windows. We also discuss the statistical results from the spectral and event analyses applied to the data at Syowa Station in 2011 and the effects of the galaxy on the velocity spectrum by calculating the apparent velocity of the stars and galaxy projected onto geographic coordinates.

#### 3.3.1 Comparison Between Spectral and Event Analyses

Using the spectral analysis described in Subsection 3.2.1, 30 phase velocity spectra were derived from the data obtained at Syowa Station in 2011. In this Subsection, we compare the phase velocity spectrum for the four data windows shown in Figures 3.5b, d, f, and h (colored) with the phase velocities (white dots with solid black lines) calculated by the event analyses for the corresponding four data windows. Airglow images (after star removal, flat-fielding, and projection to the geographic coordinates, as shown in Figure 3.2b) at the center time of each data window are also shown in Figures 3.5a, c, e, and g.

For the first example obtained at 19:13–21:15 UT on May 8, 2011, the event analysis selected one event that was clearly observed in Figure 3.5a, with wavefronts aligned in the NS direction. The phase speed and propagation direction of the azimuth were determined to be 39 m/s and  $324^\circ$ , respectively, as shown in Figure 3.5b as a white dot. The color plot (Figure 3.5b) shows the phase velocity spectrum. It features a broad peak at 10–70 m/s and  $235^\circ$ – $30^\circ$ . It is evident that the phase velocity of the event corresponds

to the peak in the spectrum. This correspondence indicates that the wave-like structure observed in a series of images is represented by a peak in the phase velocity spectrum, as observed in previous 2-D spectral analyses in the horizontal wave number domain [e.g., *Garcia et al.*, 1997]. Although no other waves were selected by the event analysis, another peak was observed at 20–150 m/s and 45°–180° in the spectrum. This peak likely corresponds to eastward-propagating waves, which are visible in the corresponding movie. However, the inability of the event analysis to capture a wave corresponding to this peak in the spectrum was due to the lack of clarity of the wavefronts in the still images.

In the second example (data obtained at 14:20–19:17 UT on July 3, 2011), three events were identified by the event analysis. The phase speeds and propagation directions were (90 m/s, 55°), (30 m/s, 282°), and (92 m/s, 112°), as indicated in Figure 3.5d. The clear peak in the phase velocity spectrum at 10–50 m/s and 270°–360° seemed to correspond to the second event (30 m/s, 282°). The other two events corresponded roughly to peaks in the spectrum but were not completely consistent with these peaks. The slight differences are probably due to the fact that the event analysis determined parameters only from parts of the wavefronts in the airglow images.

For the third example obtained at 20:24–21:51 UT on August 29, 2011 (Figure 3.5f), it is apparent that one event with a phase speed of 33 m/s and a propagation direction of the azimuth of 343° agreed with the notable enhancement in the phase velocity spectrum at 10–50 m/s and 270°–360°. There was another peak at 10–20 m/s and 180°–270°; no corresponding events were extracted by the event analysis. This peak might not represent the intensity variation of AGWs but was likely caused by galaxy alignment in the NW–SE direction around  $(x, y) = (100 \text{ km}, 250 \text{ km})$ , as shown in Figure 3.5e. The effects of the galaxy on the phase velocity spectrum will be discussed in Subsection 3.3.3. In Figure 3.5f, the spectral enhancement is evident at 20–30 m/s and 45°–135°, which also agrees with the waves visible in a movie of the airglow images. However, the waves were too faint to be extracted by the event analysis.

The fourth example obtained at 22:08–23:26 UT on September 19, 2011, shows a very broad enhancement in the phase velocity spectrum at 20–110 m/s and 135°–270° (Figure 3.5h). The broadness is likely due to the existence of several waves with

different phase speeds and propagation directions and curvature of their wavefronts in the series of images. During the event analysis, one event was selected, which had a phase speed and azimuthal propagation direction of 78 m/s and  $149^\circ$ , respectively. This example indicates that event analysis is not suitable for cases with a complex wave structure.

For a more detailed comparison, we calculated the full width at half maximum (FWHM) values of the peaks indicated in Figure 3.5 corresponding to the wave events, except for the eastward-propagating wave events in the second example. The FWHM values range from 10 to 30 m/s. As a result, there are three phase velocities of the wave events within the range of each FWHM among these four events.

In summary, all waves in the 30 data windows selected by the event analysis corresponded to peaks or enhancements in the spectra. Furthermore, using spectral analysis, we found additional peaks in the phase velocity spectra that were too faint to be detected by the event analysis. In addition, the phase velocity spectra are more suitable to describe complex wave structures and dynamics. This study suggests that the phase velocity power spectrum is more useful for the investigation of horizontal propagation characteristics of AGWs that are visible as intensity variations in the airglow images.

### 3.3.2 Average Spectrum

Statistical analysis of AGW parameters, particularly those related to horizontal propagation, is very important for the determination of the source and vertical propagation processes. Application of spectral analysis to statistical studies could reduce the time required for the analysis and the biases caused by the people processing the data. It would also allow for the analysis of large amounts of data obtained at various observation sites and/or long-term observations. Here, we compare the statistics of spectral and event analyses applied to the same airglow imaging dataset at Syowa Station obtained in 2011 and discuss the advantages of spectral analysis for statistical studies.

Figure 3.6a shows the distribution of the horizontal phase velocity extracted by event

analyses. A cluster of westward-propagating waves (azimuth between  $180^\circ$  and  $360^\circ$ ) is clearly notable; the majority of the wave have phase speeds  $< 50\text{--}60$  m/s. Eastward-propagating (azimuth between  $0^\circ$  and  $180^\circ$ ) waves are characterized by phase speeds  $> 50\text{--}60$  m/s. Figure 3.6b shows the average phase velocity spectrum from 2011 for 40 data windows; each window more contains 20 successive airglow images without clouds or auroral contamination. The average spectrum also shows a similar anisotropy in the directionality. A broad enhancement in the westward sector (azimuth between  $180^\circ$  and  $360^\circ$ ) at phase speeds  $< 50\text{--}60$  m/s can also be noted and the density is significantly larger than in the eastward sector. However, the distribution of moderate spectral densities ( $>10^{-9.5}$   $\text{s}^2/\text{m}^2$ ) is much wider in the eastward sector than in the westward sector. The former extends up to 150 m/s, while the latter is mainly confined to 100 m/s. Such similarities between the event and spectral analyses suggest that by introducing the phase velocity spectrum, we can perform statistical studies of horizontal phase velocity distributions more efficiently in a much shorter time frame with smaller biases induced by the people processing the data. It should be noted that northward-propagating waves (azimuth between  $330^\circ$  and  $30^\circ$ ) detected by the event study are rare; however, there appears to be northward spectral density, indicating that the waves are not completely blocked in these directions as one would infer from the event study. The horizontal phase velocity spectrum is capable of providing the true horizontal phase velocity distribution of observed AGWs, which leads to a more accurate interpretation of the critical level filtering. Our new spectrum-based technique has a great advantage over conventional event analyses used in previous studies.

### 3.3.3 Effects of the Galaxy on the Phase Velocity Spectrum

The galaxy or faint stars cause contamination in the airglow imaging data, especially at visible and near- infrared wavelengths. However, the effect of such contamination can be estimated because the motion of stars in the sky is a known fixed parameter and a function of the azimuth and zenith angles. Based on the image data projected onto the geographic coordinates, the apparent stellar motion could be obtained, assuming a virtual height of 90 km in this study. Thus, the velocity of a star at any pixel in the image could be precisely calculated as a time-invariant vector. The magnitude and

direction of this star motion are plotted in Figure 3.7a. The apparent speeds of the galaxy ranged between 0 and 30 m/s. In Figure 3.7b, the apparent velocity vectors are plotted over the image in the geographic coordinates averaged for 14:20–19:17 UT on July 3, 2011. The effect of the galaxy on the airglow image can be estimated more specifically if the region of the galaxy in the image is specified. For example, the brightest part of the galaxy in Figure 3.5e is located in the west (at approximately  $x, y = 100 \text{ km}, 250 \text{ km}$ ) of the image, indicated by a white ellipse. The corresponding apparent star velocity in Figure 3.7a has a southwestward direction, with a magnitude of 10–20 m/s. Therefore, the spectral peak found in southwestward direction with a speed of 10–20 m/s in Figure 3.4f is considered to be due to the contamination of the galaxy in the airglow image. Although it is desirable to decrease the galaxy contamination in the airglow images, its effect is limited and can be separated from the spectra of AGWs because the apparent speed of the galaxy in the geographic coordinate at Syowa Station is slower than 30 m/s and the major part is slower than 20 m/s. Thus, the conclusions in Subsections 3.3.1 and 3.3.2 based on Figures 3.5 and 3.6 are unaffected by the contamination of the galaxy.

For more precise analyses, the galaxy image in the airglow could be reduced using optical filters. Alternatively, the spectrum of a galaxy image could be calculated from the images of the galaxy itself, without the airglow. Such images could be obtained from the background sky image by rotational filter wheel airglow imagers. Once the galaxy spectrum is estimated, the contamination of the galaxy can be removed by subtracting the galaxy spectra from the spectra of observed airglow images in the horizontal phase velocity domain.

### 3.3.4 Discussion of the Anisotropic Distribution of Phase Velocities

We showed in Subsection 3.3.2 that there is significant anisotropy in the phase velocity distribution. Here, we compare the results with observations at a different location over the Antarctic. *Nielsen et al.* [2009] reported the horizontal phase velocity distribution of AGW events observed in 2000 and 2001 at Halley ( $76^\circ\text{S}, 27^\circ\text{W}$ ) in the Antarctic by OH airglow imaging. *Nielsen et al.* [2009, Figure 10] showed a very similar distribution to our analysis (Figure 3.6), that is, a cluster of westward-propagating waves with phase

speeds  $< 50\text{--}60$  m/s and dominance of eastward-propagating waves for phase speeds  $> 50\text{--}60$  m/s. They noted the lack of eastward-propagating waves with slow phase speeds, which they attributed to the critical level filtering of the AGWs generated by tropospheric sources of the eastward polar jet with a typical wind speed of 50-60 m/s. However, our result is at odds with their suggestion of critical level filtering in terms of a smaller number of waves with slow eastward phase speeds observed in Figures 3.6b and c. This inconsistency might be due to the difference in the ability to detect faint waves in airglow images between the event and spectral analyses and indicates the advantage of our new technique, which provides the horizontal phase velocity distribution of AGWs. Our finding of dominant eastward-propagating fast AGWs, also noted in *Nielsen et al.* [2009, Figure 10], could be interpreted as the effect of the eastward jet in the stratosphere, which is another possible source region of AGWs in addition to the troposphere. However, it is impossible to definitely determine the wave source based on a single airglow observation; more observational and modeling studies should be performed.

### 3.4 Conclusions

We developed a new spectral analysis method to obtain power spectra of the airglow intensity variation caused by short-period small-scale AGWs in the horizontal phase velocity domain. This method was applied to airglow imaging data obtained at the Syowa Station, Antarctic, in 2011 and compared with single-wave event analysis. The horizontal phase velocities of AGW events selected by the event analysis were consistent with peaks in the phase velocity spectra for 30 data windows containing more than 20 successive clear-sky aurora-free images. This suggests that the phase velocity spectrum is useful for investigating the horizontal propagation characteristics of AGWs, which are shown as intensity variations in the airglow images. The statistical results of both analyses show the eastward offset of the horizontal phase velocity distribution of AGWs. Both spectral and event analyses showed (1) a cluster of westward-propagating slow ( $<50\text{--}60$  m/s) waves and (2) the dominance of eastward-propagating waves with faster speeds (no complete absence of slower waves in this direction), which could be

interpreted as the existence of a stratospheric source in the polar night jet. The effect of the galaxy on the spectrum was discussed by calculating the apparent velocity of the galaxy and stars in geographic coordinates. The effect was limited to phase velocities slower than 30 m/s.

These results show that the current method of horizontal phase velocity spectrum creation is suitable for investigating horizontal propagation characteristics, especially statistical characteristics, of AGWs in airglow images and can deal with large amounts of data in a short amount of time without human biases. Furthermore, our new spectrum-based technique has the great advantage of providing true horizontal phase velocity distribution of observed AGWs, which leads to a more accurate interpretation of the critical level filtering compared with conventional event analyses used in previous studies. The application of this method to an extensive amount of airglow image data observed at various observation sites distributed across the globe would improve the understanding and modeling efforts of the global behavior of AGWs in the MLT region at the top of the middle atmosphere.

## Chapter 4

# Characteristics of Mesospheric Gravity Waves over the Antarctic

We obtained horizontal phase velocity distributions of gravity waves at ~90 km altitude from four ANGWIN airglow imagers. The results from the airglow imagers at Syowa, Halley, Davis, and McMurdo were compared using the new statistical analysis method for the observation period between April and May 2013. Significant day-to-day and site-to-site differences were found. The two-monthly average of the phase velocity spectrum showed a preferential westward direction at Syowa, McMurdo, and Halley but no preferential direction at Davis. The AGW energy estimated by  $I^2/I$  was ~5 times larger at Davis and Syowa than at McMurdo and Halley. We also compared the phase velocity spectrum at Syowa and Davis with the background wind field and found that only the directionality over Syowa could be explained by critical level filtering of the waves. This suggests that the eastward-propagating gravity waves over Davis could have been generated above the polar night jet. The comparison of nighttime variations of the phase velocity spectra with background wind measurements also suggested that the effect of critical level filtering could not explain the temporal variation of gravity wave directionality well; other reasons, such as the variation of wave sources, should be taken into account. The directionality was dependent on the gravity wave periods.

## 4.1 Observation and Analysis

We used data obtained by four imagers of the ANGWIN network: a Na imager at Syowa and three nearly identical broadband IR imagers operated at Davis, Halley, and McMurdo, as described in Table 1. The Na imager at Syowa (Figure 4.1a) is equipped with a CCD camera (HAMAMATSU C-4880-72) with  $512 \times 512$  pixels and a lens of a Fish-eye Nikkor (F1.4 and  $f = 6$  mm) with a field of view of  $180^\circ$ . Details of the imaging system are described in *Taguchi et al.* [2004]. The Na airglow at 589.0 and 589.6 nm was observed to avoid auroral contamination, together with background sky images at 572.5 nm. The exposure time and cadence of the Na airglow images were 45 s and 1 min, respectively. Every 15 min a background sky image was observed. During the period of background observation, the Na image was interpolated using the adjacent two images. The observation was performed during nighttime (the sun is at least  $12^\circ$  below the horizon) without moonlight. The three IR imagers (Figure 4.1b) are equipped with a  $320 \times 256$ -pixel InGaAs detector, which is sensitive to wavelengths from 0.9 to 1.7  $\mu\text{m}$ . This part of the spectrum comprises several OH emission bands, especially the bright (3,1) and (4,2) bands ( $> 100$  kR), allowing us to use a short ( $\sim 2.5$  s) exposure time and a high acquisition cadence (1 image every 10 s). A Fujinon E185C046H-1 C-mount fish-eye lens installed in these imagers enables the observation of the whole sky in one image. A PC with a Windows OS automatically controls the system through the USB (Universal Serial Bus) port. Data were acquired during the entire winter season, when the sun is at least  $8^\circ$  below the horizon, even in the presence of moonlight. For this initial study, the period between April 6 and May 21, 2013, was selected for analyses of simultaneous observation periods by investigating clear sky statistics at the Syowa Station. We then selected datasets of successive images without clouds or auroral contamination lasting for more than one hour and created time windows for the analyses. Figures 4.2a–d show a summary of the time windows for our analyses bounded by the observation time at each site. Figure 4.2e shows the periods of clear sky for all four stations. Each station had seven to nine analysis windows and the total observation time for analyses at one station was 20–30 hours. The details of the sky condition statistics are summarized in Table 2.

We applied the spectral analysis method developed in Chapter 3 to the data observed at

each of the four different stations to derive phase velocity spectra. This new technique can be used to display the distribution of the phase velocity and direction. Importantly, the intensity of the spectral component includes information about the AGW amplitudes in the airglow images, duration of the AGW event, and spatial extent of the wave packet. Another advantage is that, compared with conventional manual analysis methods, it provides objective results and requires a shorter analysis time.

Although the basic spectral data analysis procedure is the same as described in Chapter 3, several changes have been applied as follows. For the OH and Na airglow, images of  $I'/I$ , the airglow intensity perturbation normalized by the temporal mean of the airglow images, were projected onto the geographic coordinate system, assuming mean emission heights of 87 and 90 km, respectively. The projection onto the geographic coordinate system used an area of  $256 \times 256 \text{ km}^2$  with  $1\text{-km}^2$  pixel size; subsequently, a 3-D array with a size of  $1024 \text{ pixels} \times 1024 \text{ pixels} \times 240 \text{ images}$  was created using zero-padding to improve the interval of the spectrum with respect to wavenumber and frequency. It should be noted that the sampling interval of the Utah State University imagers was 10 s; therefore, six images were averaged to obtain 1-min interval images compatible with the Syowa measurement cadence. Based on the preprocessed images, we obtained a 3-D spectrum as a function of frequency, zonal wavenumber, and meridional wavenumber by using 3-D discrete Fourier transformation [Coble *et al.*, 1998]. Next, the 3-D spectrum was converted to the phase velocity domain. Finally, the 3-D phase velocity spectrum was integrated in the frequency domain and a 2-D phase velocity spectrum was calculated. We extracted spectral components with horizontal wavelengths of 10–100 km, periods of 8–60 min, and phase speeds of 0–150 m/s and regarded them as representative for AGWs within these analysis ranges.

## 4.2 Results and Discussion

### 4.2.1 Station-to-Station and Day-to-Day Variation

Figures 4.3a and b and 4.4a and b show example phase velocity spectra results at Davis observed during the intervals of 15:36–20:15 UT on April 10 and 19:06–21:44 UT on

April 11, 2013, respectively. On April 10 (Figure 4.3a), the spectral power of the phase speeds  $< 60$  m/s was stronger in the westward direction ( $150^{\circ}$ – $320^{\circ}$ ), and weaker in the northward direction ( $320^{\circ}$ – $10^{\circ}$ ). However, for spectral components with phase speeds  $> 60$  m/s the spectral power was larger in the eastward direction ( $30^{\circ}$ – $180^{\circ}$ ) and weaker in the westward direction ( $180^{\circ}$ – $360^{\circ}$ ). On the next day, April 11 (Figure 4.3b), the spectrum was more uniform with respect to the azimuth of the phase speeds  $< 70$  m/s. Enhancements in the southeastward ( $80^{\circ}$ – $180^{\circ}$ ) and westward ( $190^{\circ}$ – $350^{\circ}$ ) directions were also observed for phase speeds of 20–70 m/s and  $< 50$  m/s, respectively.

Figures 4.3c and d and 4.4c and d show the wave spectra for the same two-day interval obtained at McMurdo from 9:15–13:43 UT on April 10, 2013, and 11:08–12:45 UT on April 11, 2013, respectively. On April 10 (Figure 4.3c), the spectrum exhibited two peaks: one (strong) with phase speeds of 20–60 m/s at an azimuth of  $320^{\circ}$ – $10^{\circ}$  and the other (weaker) with phase speeds of 10–40 m/s at an azimuth of  $180^{\circ}$ – $230^{\circ}$ . On the next day, the wave spectrum (Figure 4.3d) exhibited three distinct peaks in the same phase speed range of 20–40 m/s at  $0^{\circ}$ – $30^{\circ}$ ,  $140^{\circ}$ – $180^{\circ}$ , and  $240^{\circ}$ – $300^{\circ}$  in azimuth (i.e., almost North, South, and West). The regions at  $30^{\circ}$ – $140^{\circ}$  also indicate faster waves with phase speeds of 50–100 m/s propagating mainly eastward.

These four spectra in Figure 4.3 demonstrate strong day-to-day variations of the wave directionality between April 10–11 at Davis and McMurdo and a difference in the directionality between the two stations on the same day. This suggests that the directionality of AGWs over the Antarctic is highly variable in time and space.

In Figures 4.5 and 4.6, we compare the average phase velocity spectra observed from April 6 to May 12, 2013. The spectrum at Syowa (Figure 4.5a), averaged over nine nights, showed an enhanced region in the westward direction ( $180^{\circ}$ – $80^{\circ}$ ) for phase speeds  $< 60$  m/s, whereas an enhancement in the eastward direction was found for phase speeds  $> 70$  m/s. This directionality is very similar to that previously reported in Chapter 3 for the Syowa Station in 2011.

The spectrum at Davis (Figure 4.5b), averaged over eight nights, was more uniform with respect to the phase speeds  $< 50$  m/s compared with the other spectra in Figure 4.5.

At McMurdo an averaged spectrum was obtained for seven nights of observations

(Figure 4.5c). A weak peak in the northward direction ( $330^{\circ}$ – $360^{\circ}$ ) with phase speeds of 20–50 m/s was found, which was similar to the spectrum on April 10, 2013, as shown in Figure 4.3c. Another enhancement can also be noted in the phase speeds  $< 40$  m/s at an azimuth of  $210^{\circ}$ – $330^{\circ}$ . The AGW (northward) on 10 April had a large spectral power and greatly contributed to the averaged spectrum. An AGW with large spectral power carries large momentum, because measured AGW power is proportional to duration, spatial extent and the square of wave amplitude. Thus, an AGW with large momentum greatly affects the averaged spectrum. The case on 10 April is a good example of the ability of spectrum analysis to express AGW energy as spectral power.

The averaged spectrum at Halley derived based on seven nights (Figure 4.5d) showed a southward broad enhancement in the phase speeds  $< 70$  m/s at an azimuth of  $110^{\circ}$ – $220^{\circ}$ . Westward enhancement at an azimuth of  $210^{\circ}$ – $330^{\circ}$  and with phase speeds  $< 30$  m/s was also recognized.

Among the four averaged spectra, the more uniform directionality observed at Davis was exceptional. The other three stations exhibited preferential propagation, primarily in the westward direction, and a lack of waves in the southeastward direction at Syowa, in the eastward direction at McMurdo, and in the northeastward direction at Halley (possibly caused by the critical level filtering of background wind). This topic will be discussed in more detail in Sections 4.2 and 4.3.

Next, we examined the averaged gravity wave energy by integrating the power spectra shown in Figure 4.5 for all the phase speeds between 0–150 m/s. This integrated value corresponds to the variance of  $I'/I$  and represents the gravity wave energy because  $I'/I$  is proportional to the relative temperature perturbation by AGWs (i.e.,  $T'/T$ ), as described in Section 2.1. The resultant “wave power” at each station is plotted as a function of latitude in Figure 4.7. It is clear that the spectral power is smaller at higher latitudes. The spectral power at Davis is 5–6 times larger than that at McMurdo, which is located  $9^{\circ}$  further south of Davis. *Yamashita et al.* [2009] compared the potential energy of gravity waves in the stratosphere (30–45-km altitude) observed by lidar at Rothera ( $67.5^{\circ}$ S) and the South Pole ( $90^{\circ}$ S; their Figure 4.7c). The potential energy in May at Rothera was 5 times larger than that at the South Pole, with the two stations located  $22.5^{\circ}$  apart in latitude. It is interesting to note that a similar factor of energy difference

(~5 times) was achieved by only  $9^\circ$  of difference in latitude in the mesopause region. The significant decrease of the wave energy at mesopause heights between Davis and McMurdo could be due to the fact that the AGWs analyzed in our airglow observations had shorter periods ( $< 60$  min, i.e.  $< 10$  times the buoyancy period) and propagated more vertically than the waves observed by lidar (with typical periods of several hours, propagating more horizontally) [Lu *et al.*, 2009; 2015b; Chen *et al.*, 2016]. If the major AGW sources are located around the meteorological disturbances near the Antarctic continent (e.g. a storm track at the latitude range of  $50^\circ\text{S}$ - $60^\circ\text{S}$  [Trenberth, 1991]), the AGW energy observed over Davis and Syowa in the mesosphere could be significantly larger than at the other two stations, McMurdo and Halley. On the other hand, inertial AGWs can propagate more horizontally and the latitudinal difference could be smaller. Alexander (1998) pointed out that the global variations of the AGW activity could be largely explained by background wind effects without variations in AGW sources based on a ray-tracing model. More observational data and modeling is needed to investigate this further.

#### 4.2.2 Comparison with the Blocking Diagram

In Figure 4.8, we show the directionality of the phase velocity spectra at Syowa and Davis and discuss the effect of background wind derived from MERRA and MF radar observations [Tsutsumi *et al.*, 2001]. The MERRA data are reanalysis data with  $288 \times 144$  grids (i.e.,  $1.25^\circ$  longitude and  $1.25^\circ$  latitude resolution), 42 pressure levels between 1000 and 0.1 hPa, and a temporal resolution of 3 h [Rienecker *et al.*, 2011]. We selected these two stations because of the availability of MF radar winds. The blocking diagram described by Taylor *et al.* [1993] shows a phase velocity distribution of AGWs, which cannot reach the airglow altitude due to critical level filtering. We derived a blocking diagram from wind profiles of MERRA (altitude of 0–64 km) and MF radar observations (altitudes of 70–90 km at Syowa and 70–86 km at Davis).

Figure 4.8a shows a phase velocity spectrum obtained at Syowa at 18:38–21:48 UT on May 3, 2013. The peak of the spectrum was observed for phase speeds of 10–30 m/s, primarily in the northward direction. In comparison, the power in the eastward and northeastward directions was rather small. The second panel (Figure 4.8b) plots the

combined wind profiles using the 18:00 UT data from MERRA and the Syowa MF radar data between 18:00 and 19:00 UT on the same day. The zonal wind was positive (i.e., eastward) between the ground and 90-km altitude, with a strong eastward peak at 55 km with a magnitude of 90 m/s. The meridional wind was weakly negative (southward) and gradually became stronger at altitudes up to 80 km (~20 m/s). The corresponding blocking diagram is given in Figure 4.8c. A major part of the blocked area was observed in the eastward direction and agreed well with the wave spectra (Figure 4.8a), where the spectral power in the eastward direction was generally very weak.

Figures 4.8d–e show a similar set of plots for data obtained two days later on May 5, 2013. The spectrum (Figure 4.8d) showed directionality, with a more enhanced region in the northward-northeastward direction and lower power in the southeastward-eastward direction. The blocking diagram in Figure 4.8f shows that AGWs propagating in northward–northeastward direction can reach the Na airglow layer from the ground and AGWs propagating in southeastward–eastward direction are blocked, which is consistent with the directionality shown in Figure 4.8d.

Figures 4.8g–i display the results of a similar analysis for Davis on April 21, 2013. The spectrum observed at 21:40–00:27 UT (Figure 4.8g) exhibited strong enhancement in wave activity in almost all directions, except towards the north. The wind profiles from MERRA and MF radar winds between altitudes of 0 km and 85 km showed eastward wind with a weak meridional component, similar to Syowa. The resultant blocking diagram in Figure 4.8i suggests that the eastward-propagating AGWs should be significantly blocked. This is inconsistent with the observed directionality shown in Figure 4.8g.

An example of the next day at Davis, April 22 (Figures 4.8j–l), indicates a situation very similar to that in Figures 4.8g–i. The directionality was omni-directional; however, the blocking diagram indicated restricted vertical propagation only for eastward propagating AGWs.

The lack of eastward-propagating AGWs over Syowa in Figures 4.8a and d is consistent with the inference that the AGWs were generated below the stratosphere and restricted to propagate vertically by critical level filtering due to the strong polar night jet. On the

other hand, the directionalities in the phase velocity spectra over Davis in Figures 4.8g and j were inconsistent with the blocking diagrams shown in Figures 4.8i and l. This suggests that the AGWs observed over Davis with an eastward propagation direction might have been generated at higher altitudes above which critical level filtering of the polar night jet was not effective, although the relative location of Davis and the polar night jet is similar to that of Syowa and the polar night jet. This would also explain the more uniform directionality of the averaged wave spectrum at Davis (Figure 4.4b) described in Section 4.2.1. There are several studies suggesting AGW generation in the stratosphere based on lidar observations [e.g. Lu et al., 2015b]. However, these studies could not identify the altitude at which AGWs were generated. Our study is successful in specifying an altitude of AGW generation, because airglow imaging technique can derive phase velocity distribution including information of critical level filtering.

#### 4.2.3 Temporal Variation on the Night of May 11–12, 2013

The ground-based airglow imaging technique has the advantage of more temporally continuous observations at a fixed observation site than satellite airglow imaging observations (e.g., VISI of ISS-IMAP [Sakanoi et al., 2011]). Here, we show the analysis of nighttime variations of the hourly mean phase velocity spectra and compare them with their corresponding blocking diagrams. Figures 4.9a-i show hourly mean phase velocity spectra for nine hours between 15:00 UT on May 11 and 00:00 UT on May 12, 2013, at the Syowa Station.

The spectrum at 15:00–16:00 UT on May 11, 2013, at Syowa (Figure 4.9a) shows enhancement in the northwestward direction ( $270^{\circ}$ – $350^{\circ}$ ) for phase speeds  $< 60$  m/s. The blocking diagram from MERRA (0–64 km, blue line) in Figure 4.9a covers the eastward direction, whereas the blocked region from MF radar (70–90 km, red line) is between the northward, eastward, and southwestward directions with phase speeds  $< 30$  m/s. The observed direction of the enhancement in the phase velocity spectrum is consistent with these combined blocking diagrams. It is also interesting that there was some enhancement in the northeastward, eastward, and southeastward directions just outside the blocking diagram (plotted in blue) at phase speeds of  $\sim 60$ – $120$  m/s. An hour later, the region of enhancement of the spectrum in the northwestward direction

expanded to the azimuth of  $250^{\circ}$ – $70^{\circ}$  with phase speeds up to 70 m/s, as shown in Figure 4.9b. For the next few hours, the enhancement became stronger, as plotted in Figures 4.9c–e. A comparison of the Figures 4.9a and d shows that the expansion of the enhancement direction from northwestward to a larger region from northeast to southwest is consistent with the shrinking of the blocked area over the northeastward and southwestward azimuth range. In Figures 4.9f and g, the enhancement in the westward direction extended southward for phase speeds  $< 50$  m/s, which is consistent with the reduction in the MF radar-blocked region of the southwestward direction. After the enhancement of the same region in Figure 4.9g, at 22:00–23:00 UT, the enhancement in northward and southward directions disappeared and the dominant region maintained westward direction ( $210^{\circ}$ – $330^{\circ}$ ) for phase speeds  $< 70$  m/s, as shown in Figure 4.9h.

In summary, the phase velocity spectra exhibited enhanced regions mostly to the west, with the weakest power towards the southeast, for phase speeds up to 70 m/s throughout the night. The weak region corresponded well to the blocked area due to critical level filtering. The agreement between the variation of directionality and blocking diagram among Figures 4.9a, d, and g also suggests that critical level filtering by background winds significantly controls the directionality variation over the course of a night. However, Figures 4.9g and 4h show no corresponding variation between spectra and blocking diagrams. This difference between before and after 22:00 UT might be due to the source variation rather than variation of propagation conditions. Thus, the azimuthal extent and temporal variation of the spectra in one night cannot be explained by critical level filtering of the background wind field alone; source variations are also important.

#### 4.2.4 Wave Period Dependency of the Directionality

In this Subsection, we investigate the difference in the directionality between different observed wave periods by dividing the phase velocity spectrum into six period bands. The period bands were selected to be 8–11, 11–15, 15–22, 22–30, 30–43, and 43–60 min; each period band has the same bandwidth normalized by the center period. Figures 4.10 and 4.11 show the phase velocity spectra for these different period bands (a–f and h–m) and the phase velocity spectrum integrated for the entire 8–60-min band (g and n).

The first example (Figures 4.10a–g) was observed at 15:36–20:15 UT on April 10, 2013, at Davis. The spectrum in Figure 4.10g exhibits spectral enhancement at the azimuth of  $180^{\circ}$ – $310^{\circ}$  for phase speeds of 10–70 m/s, which can also be noted for all period bands in Figures 4.10b–f. The enhancement in the southwestward direction ( $180^{\circ}$ – $310^{\circ}$ ) with phase speeds up to 50 m/s was stronger for longer wave periods such as 15–60 min. This suggests that the AGWs corresponding to this enhancement had a broad spectrum with respect to the wave period.

The second example (Figures 4.10h–n) was observed at 17:21–21:13 UT on April 17, 2013, at Davis. The spectrum for the wave periods of 8–60 min (Figure 4.10n) shows three enhanced regions: in northeastward ( $20^{\circ}$ – $90^{\circ}$ , 20–90 m/s), southward ( $130^{\circ}$ – $220^{\circ}$ , 10–60 m/s), and westward ( $220^{\circ}$ – $300^{\circ}$ , 0–80 m/s) directions. The northeastward enhancement appeared for the 8–60-min band period (Figures 4.10h–m), while the southward enhancement was clearly due to the 22–60-min band period (Figures 4.10k–m). The westward enhancement occurred for the 8–30-min band period (Figures 4.10h–k) but it was shifted slightly southward for the 30–42-min band period (Figure 4.10l). This enhancement seems to have merged with the southward enhancement (Figure 4.10m) for the 43–60 min-band period, where only two enhanced regions could be recognized. Thus, the spectra on April 17 (Figures 4.10h–n) appear to show different directionality depending on the wave period ranges, which is quite different from the spectra on April 10 (Figures 4.10a–g).

The third example (Figures 4.11a–g) was observed at 17:03–20:23 UT on April 7, 2013, at Syowa. The enhancement in the northwestward direction became stronger for longer periods, suggesting the existence of AGWs with a period out of the range for the analysis parameters in the current study.

The fourth example (Figures 4.11h–n) was observed 18:10–21:21 UT on May 12, 2013, at Syowa. The spectrum for the 8–11-min band (Figure 4.11h) exhibited an enhancement in westward direction ( $240^{\circ}$ – $340^{\circ}$ ) for phase speeds of 30–70 m/s, which was broader in azimuth for the 22–60-min band (Figures 4.11k–m) and moved to slower phase speeds in the 8–30-min band (Figures 4.11h–k).

Our results show that spectral power in Figures 4.11a–g and 4.11h–n were larger in the 22–60-min band than in the 8–22-min band, although the result in Chapter 3 showed

that the AGW periods observed at Syowa in 2011 derived by conventional event analysis were mostly distributed in periods  $< 20$  min. This suggests that the spectral analysis method can be used to more appropriately derive the horizontal phase velocity distribution of AGWs with longer periods ( $> 20$  min) compared with the conventional event analysis method.

### 4.3 Conclusions

We applied a new spectral analysis method to airglow data observed by several ANGWIN imagers at sites around the Antarctic continent. The results from four stations, Syowa, Halley, Davis, and McMurdo, were compared using data obtained over an early winter period between April 6 and May 21, 2013. The results obtained for two consecutive nights at two different sites showed significant day-to-day and site-to-site differences. The two-month averages of the phase velocity distribution at four stations showed a preferential propagation direction, primarily towards the west, at Syowa, McMurdo, and Halley. The comparison with the blocking diagrams suggests that these directionalities could be caused by critical level filtering of the background wind field due to the strong polar night jet. However, the directionality at Davis is almost uniform and quite different from that of the other three stations. The blocking diagrams at Syowa and Davis show a common feature; eastward-propagating AGWs generated near the ground cannot reach the airglow altitudes. The observed phase velocity spectra are consistent with the blocking diagram at Syowa but not with that at Davis. The inconsistency between the observed phase velocity spectra and blocking diagram suggests that the AGWs around the mesopause over Davis might be generated above the core of the polar night jet, where critical level filtering by the polar night jet is not effective. A possible source for these waves could be secondary wave generation, although more data are needed to reach a definitive conclusion. We also examined the averaged AGW energy by integrating the averaged power spectra for all phase speeds between 0–150 m/s. The results show that the spectral power at Davis was 5–6 times larger than that at McMurdo, which is located  $9^\circ$  further south of Davis. One of the explanations is that the major AGW sources are located around the Antarctic continent.

The detailed variations of the phase velocity spectra during one night at hourly intervals at Syowa were compared with the blocking diagrams. It was found that the hourly variations of the power spectrum depend not only on the critical level filtering but also on other factors such as source variations. The phase velocity spectrum for different wave periods revealed the variation of the directionality with the wave period and the variation of the dominant wave period for each spectral component. We show that the spectral analysis technique allows us to represent the wave period dependence and short-period variation of directionality and the AGW power in the phase velocity domain. This study is the first successful application of the new spectral analysis method developed in Chapter 3 to airglow data observed by different instruments at multiple stations.

# Chapter 5

## Summary and Conclusions

This thesis is devoted to investigating the characteristics of mesospheric AGWs over the Antarctic observed with the ANGWIN imager network by developing a new spectral analysis method.

In Chapter 1, we introduced the Earth's atmospheric structure and atmospheric waves including AGWs. The AGWs, generated in the lower atmosphere, can propagate to the mesosphere and lower thermosphere, transport a large amount of energy and momentum, and release them in various altitude regions. Among many parameters characterizing gravity waves, the horizontal phase velocity is of importance for the discussion of the vertical propagation and where the momentum is released.

In Chapter 2, we mentioned airglow-imaging observations of AGWs. Near the mesopause region, OH and other airglow imaging has been used to investigate the horizontal structures of AGWs for more than two decades. However, the generation source and propagation conditions of AGWs observed by airglow imaging, especially in the Antarctic, are not fully understood. Although huge amounts of airglow image data have been obtained at various observation sites worldwide, time-consuming manual procedures have been used to extract the horizontal propagation characteristics from airglow data. This causes difficulties in obtaining a global map of AGW characteristics in the mesopause region. In this thesis, we aim to reveal the climatology of mesospheric AGWs over Syowa (Chapter 3) and quantitatively investigate differences among horizontal phase velocity distributions of mesospheric AGWs over the four ANGWIN stations focusing on critical level filtering (Chapter 4).

In Chapter 3, we developed a new spectral analysis method to obtain power spectra of the airglow intensity variation caused by short-period small-scale AGWs in the horizontal phase velocity domain. This method can deal with extensive amounts of imaging data obtained in different years and at various observation sites without bias caused by different event extraction criteria of the person who processed the data. This

method was applied to the airglow imaging data obtained at the Syowa Station in the Antarctic in 2011. The results were compared with the single-wave event analysis. The horizontal phase velocities of the AGW events selected by the event analysis were consistent with peaks in the phase velocity spectra for the 30 data windows containing more than 20 successive clear-sky aurora-free images. This suggested that the phase velocity spectrum is useful for the investigation of the horizontal propagation characteristics of AGWs when analyzing intensity variations in airglow images. The statistical results of both analyses showed the eastward offset of the horizontal phase velocity distribution of AGWs. Both spectral and event analyses showed (1) a cluster of westward-propagating slow ( $< 50\text{--}60$  m/s) waves and (2) the dominance of the eastward-propagating waves with high speeds (no complete absence of slower waves in this direction), which could be interpreted as the existence of a stratospheric source in the polar night jet. The effect of the galaxy on the spectrum was discussed by calculating the apparent velocity of the galaxy and stars in the geographic coordinates. The effect was limited to phase velocities less than 30 m/s. These results show that the current method of horizontal phase velocity spectrum creation is suitable for the investigation of the horizontal propagation characteristics, especially statistical characteristics, of AGWs in airglow images and can deal with large amounts of data in a short amount of time without human biases.

In Chapter 4, we applied the new spectral analysis method to the airglow data observed by ANGWIN imagers. The results from the airglow imagers at four stations, Syowa, Halley, Davis, and McMurdo, have been compared for the observation period between April 6 and May 21, 2013. The results obtained for the two consecutive nights (April 10–11) at the two different sites (Davis and McMurdo) showed significant day-to-day and site-to-site differences. The two-month averages of the phase velocity distribution at four stations showed a preferential propagation direction, primarily westward, and the lack of waves in southeastward direction at Syowa, eastward direction at McMurdo, and northeastward direction in Halley. This might be caused by critical level filtering of the background wind. However, the directionality at Davis was quite different and almost uniform with respect to the azimuth. The blocking diagrams at Syowa and Davis derived from MERRA and MF radar suggested that the eastward-propagating AGWs generated near the ground could not reach the airglow altitudes. The observed phase

velocity spectra were consistent with this scenario at Syowa but not at Davis. The eastward-propagating AGWs in the phase velocity spectra at Davis suggested that the AGWs over Davis could be generated above the stratosphere, where critical level filtering by the polar night jet was not effective. The nocturnal variation of hourly phase velocity spectra calculated between 15:00 UT on May 11 and 00:00 UT on May 12, 2013, at Syowa was compared with the blocking diagrams calculated from MERRA and MF radar wind. We found that it is difficult to explain the variations of the hourly power spectrum by considering critical level filtering alone. The phase velocity spectrum with different wave periods revealed the variations of the directionality with wave periods and dominant wave periods for phase velocity spectral components. It should be noted that this study represents the first successful application of the new spectral analysis method developed in Chapter 3 to data observed by the airglow-imaging network.

With respect to the extension of this study and future work, we would like to point out three issues.

(1) Analysis of a wider spectral range of both frequency and horizontal scale

This technique has already been applied to examine AGWs with longer horizontal wavelengths (100–200 km) and longer periods (1–2 h), as shown in the appendix. The spectral ranges can be further expanded to lower frequency and larger horizontal scale. Such an expansion will be useful to perform comparisons with other instruments or GCMs. This expansion is also important because *Sato et al.* [2017] recently suggested that AGWs with horizontal wavelengths  $> 100$  km and periods  $> 1$  h are more important for the momentum transport into the mesosphere than small-scale ( $< 100$  km) and short-period ( $< 1$  h) AGWs.

(2) Analysis of a large amount of ANGWIN imager data for the complete understanding of gravity wave characteristics over the Antarctic

In this study, ANGWIN data of two months have been analyzed for four stations. The ANGWIN network consists of more stations and a large amount of imager data has already been accumulated for many years. As future work of ANGWIN, further analysis is needed to understand the continental-scale characteristics of AGWs in the Antarctic.

The unique directionality of AGWs at Davis and their generation source are also interesting topics of future research. For this purpose, the large amount of data observed at other stations of ANGWIN should be analyzed using the new technique.

(3) The distribution of the new technique in the international airglow imager community and various imaging communities in different disciplines

The software package of the new spectral analysis technique developed here has already been distributed to the Utah State University and Nagoya University and is being applied to the dataset obtained by the ANGWIN and OMTI networks [*Takeo et al.*, under review]. The standardization of this method and its dissemination in the airglow community will lead to an expansion of the analysis to the international airglow imager network and would contribute to the quantitative understanding of the global AGW distribution and their variations. Time-series analysis of space-borne airglow-imaging observations could also be a promising target for the application of the technique. Moreover, this method can be applied to the analysis of any consecutive image dataset such as Traveling Ionospheric Disturbances (TIDs) found in the Total Electron Content (TEC) map observed by GPS networks. This technique has also great potential in dealing with various physical data of different disciplines.

To summarize this study, we compared the phase velocity distributions over four Antarctic stations. The results show that critical level filtering could explain a part of the phase velocity distributions and their time variations. It is clearly shown that the averaged phase velocity spectrum at Davis is inconsistent with the blocking diagram, while the other three averaged spectra seem to be affected by critical level filtering. This unique characteristic at Davis suggests that the AGWs over Davis might be generated above the stratosphere. This result is very important for the improvement of AGW parameterization because AGWs in GCMs are treated as tropospheric origin. Furthermore, our new spectrum-based technique and its application to other airglow imagers will greatly contribute to the investigation of the time and space intermittency of mesospheric AGWs and improvement of AGW parameterization.

# Appendix

Figure A1 (a) is a phase velocity spectrum obtained from artificial test data as shown in Figure A1 (b) containing two waves with the same periods of 20 min, horizontal wavelengths of 20 km and 40 km, phase speeds of 17 m/s and 33 m/s, and northwestward and southwestward propagation directions, respectively. The test data have a spatial size of  $400 \times 400 \text{ km}^2$  with a resolution of  $1 \times 1 \text{ km}^2$  in geographic coordinates and consists of consecutive 60 images with a 1-min sampling interval (1-h duration). In Figure A1 (a), two independent peaks are seen at the expected phase velocities. It is confirmed that the new spectral analysis method estimates an accurate spectrum. Other weak peaks are also noted in the northeast and southeast directions. These weak peaks have spectral powers of  $\sim 1\%$  of the primary peak and might be a result of spectral power leaks due to side lobe. Figure A1 (c) is the phase velocity spectrum derived from the same test data mentioned above except for a spatial size of airglow images ( $200 \times 200 \text{ km}^2$ ) as shown in Figure A1 (d). It is notable that the peaks are broader approximately twice than the peaks in Figure A1 (a). This is caused by a difference of the image size which corresponds to a spatial size of the AGW packet. This result suggests that AGW packets with a larger spatial size have an shaper peaks in spectra.

The airglow imaging technique has been mainly used for the analysis of short-period AGWs ( $< 1 \text{ h}$ ). However, AGWs have a broader period range between the Brunt-Väisälä period ( $\sim 6 \text{ min}$  at the mesopause altitude) and the inertia period ( $\sim 12.9 \text{ h}$  at  $69^\circ\text{S}$ ). Thus, it is required in the new spectral analysis to treat AGWs with a period  $> 1 \text{ h}$ . Here, the new analysis method was applied to extract AGWs with longer periods and horizontal wavelengths from airglow observations. Figure A2 compares phase velocity spectra with different ranges of horizontal wavelength and period. The spectral power is stronger in northward direction and weaker in southward direction in both Figures A2 (a, b), while Figures A2 (c, d) have a different directionality in northwestward direction and eastward direction, respectively. This result suggests that different spectral ranges of interest could affect the directionality of gravity waves.

Figure A3 shows the averaged horizontal wavelength spectra from the data at Syowa

and Davis during the observation period of April 6 and May 21, 2013, because the airglow data in 2013 seem to be noisy compared with the data in 2011. The spectra in Figure A3 were calculated from the 3-D spectra in horizontal wavenumber and frequency domain by averaging them in azimuth and frequency direction. The spectral densities in Figure A3 increase in proportion to the  $3-5/3$ th power of the horizontal wavelength in the range of the horizontal wavelengths 10–256 km. In the range of the horizontal wavelength  $> 256$  km, the spectral densities decrease because the range is out of the image size (256 km). The spectral density in the range of the horizontal wavelength  $< 10$  km decreases only at Syowa. Because the white noise uniformly distributes on each component of the  $(k, l, \omega)$  spectra, the spectral densities of the imager's random noise integrated in azimuth direction increase in proportion to the horizontal wavelength. Thus, the noise of the imager at Syowa in the range of horizontal wavelength  $< 10$  km is greater than the airglow signal. This result suggests that spectral densities obtained by all the four imagers had a sufficient signal-to-noise ratio in the horizontal wavelength range of interest (10–100 km).

We discussed the effects of the galaxy on the phase velocity spectrum in Subsection 3.3.3. Here we extend the discussion to other latitudes. The virtual star velocities at the altitude of 90 km are shown at the four latitudes of Figure 3.7 in Figure A4. This figure indicates that the virtual star velocities reach 45 m/s at  $0^\circ$  and 20 m/s at  $90^\circ\text{N}$  at the edge of the geographical coordinate. This result shows that the virtual star velocities become larger at lower latitudes.

# References

- Alexander, M.J., 1998, Interpretations of observed climatological patterns in stratospheric gravity wave variance, *J. Geophys. Res.*, 103(D8), 8627–8640, doi:10.1029/97JD03325.
- Aumann, H.H., et al., 2003, AIRS/AMSU/HSB on the Aqua mission: design, science objectives, data products, and processing systems, *IEEE Trans. Geosci. Remote Sens.*, 41, 253–264, doi:10.1109/TGRS.2002.808356.
- Bageston, J.V., C. M. Wrasse, D. Gobbi, H. Takahashi, and P. B. Souza, 2009, Observation of mesospheric gravity waves at Comandante Ferraz Antarctica Station (62°S), *Ann. Geophys.*, 27(6), 2593–2598, doi:10.5194/angeo-27-2593-2009.
- Bates, D. R., and M. Nicolet, 1950, The photochemistry of atmospheric water vapor, *J. Geophys. Res.*, 55(3), 301–327, doi:10.1029/JZ055i003p00301.
- Blamont, J. E., M. L. Chanin, and G. Megie, 1972, Vertical distribution and temperature profile of the nighttime atmospheric sodium layer by laser backscattering, *Ann. Geophys.*, 28, 833-838.
- Cai, X, T. Yuan, Y. Zhao, P.-D. Pautet, M. J. Taylor, and W. R. Pendleton Jr, 2014, A coordinated investigation of the gravity wave breaking and the associated dynamical instability by a Na lidar and an Advanced Mesosphere Temperature Mapper over Logan, UT (41.7°N, 111.8°W), *J. Geophys. Res.*, 119, 6852–6864, doi:10.1002/2014JA020131.
- Chamberlain, J. W., 1995, *Physics of the Aurora and Airglow*, American Geophysical Union, doi: 10.1002/9781118668047.
- Chanin, M.-L., and A. Hauchecorne, 1981, Lidar observation of gravity and tidal waves in the stratosphere and mesosphere, *J. Geophys. Res.*, 86(C10), 9715–9721, doi:10.1029/JC086iC10p09715.

Charney, J. G, and P. G. Drazin, 1961, Propagation of planetary-scale disturbances from the lower into the upper atmosphere, *J. Geophys. Res.*, 66(1), 83–109, doi:10.1029/JZ066i001p00083.

Chen, C., X. Chu, J. Zhao, B. R. Roberts, Z. Yu, W. Fong, X. Lu, J. A. Smith (2016), Lidar observations of persistent inertia-gravity waves with periods of 3–10 h in the Antarctic middle and upper atmosphere at McMurdo, *J. Geophys. Res. Space Physics.*, 10.1002/2015JA022127.

Coble, M, G. C. Papen, and C. S. Gardner, 1998, Computing two-dimensional unambiguous horizontal wavenumber spectra from OH airglow images, *IEEE Trans. Geosci. Remote Sens.*, 36(2), 368–382, doi:10.1109/36.662723.

Crawford, J., Rothwell, P. and Wells, N., 1975, Airborne television observations of airglow clouds in the near infrared, *Nature*, 257, 650.

Crawford, J., Rothwell, P. and Taylor, M. J, 1978, ASSESS 2 : a simulated mission of Spacelab. Review article,, *Nature*, 257, 17.

Dou, X., T. Li, Y. Tang, J. Yue, T. Nakamura, X. Xue, B. P. Williams, and C. - Y. She, 2010, Variability of gravity wave occurrence frequency and propagation direction in the upper mesosphere observed by the OH imager in Northern Colorado, *J. Atmos. Sol. Terr. Phys.*, 72(5–6), 457–462, doi:10.1016/j.jastp.2010.01.002.

Ejiri, M. K., K. Shiokawa, T. Ogawa, K. Igarashi, T. Nakamura, and T. Tsuda, 2003, Statistical study of short-period gravity waves in OH and OI nightglow images at two separated sites, *J. Geophys. Res.*, 108(D21), 4679, doi:10.1029/2002JD002795.

Espy, P. J., G. O. L. Jones, G. R. Swenson, J. Tang, and M. J. Taylor, 2004, Seasonal variations of the gravity wave momentum flux in the Antarctic mesosphere and lower thermosphere, *J. Geophys. Res.*, 109, D23109, doi:10.1029/2003JD004446.

Espy, P. J., et al., 2006, Regional variations of mesospheric gravity-wave momentum flux over Antarctica, *Ann. Geophys.*, 24(1), 81-88, doi:10.5194/angeo-24-81-2006.

- Fleming, E.L., S. Chandra, M.R. Schoeberl and J.J. Barnett, 1988, Monthly mean global climatology of temperature, wind, geopotential height, and pressure for 0-120 km, NASA Tech. Memo. NASA TM-100697, 85 pp, doi:10.1016/0273-1177(90)90230-W.
- Franke, S. J., X. Chu, A. Z. Liu, and W. K. Hocking, 2005, Comparison of meteor radar and Na Doppler lidar measurements of winds in the mesopause region above Maui, Hawaii, *J. Geophys. Res.*, 110, D09S02, doi:10.1029/2003JD004486.
- Fritts, D. C., and M. J. Alexander, 2003, Gravity wave dynamics and effects in the middle atmosphere, *Rev. Geophys.*, 41(1), 1003.
- Fritts, D. C., and R. A. Vincent, 1987, Mesospheric momentum flux studies at Adelaide, Australia: Observations and a gravity wave/tidal interaction model, *J. Atmos. Sci.*, 44, 605–619.
- Gardner, C. S., and M. J. Taylor, 1998, Observational limits for lidar, radar, and airglow imager measurements of gravity wave parameters, *J. Geophys. Res.*, 103(D6), 6427–6437, doi:10.1029/97JD03378.
- Gardner, C. S., M. S. Miller, and C. H. Liu, 1989, Rayleigh lidar observations of gravity wave activity in the upper stratosphere at Urbana, Illinois, *J. Atmos. Sci.*, 46, 1838–1854, doi:10.1175/1520-0469(1989)046<1838: RLOGW>2.0.CO;2.
- Geller, M. A., et al., 2013, A Comparison between Gravity Wave Momentum Fluxes in Observations and Climate Models, *J. Clim.*, 26, 6383–6405, doi:10.1175/JCLI-D-12-00545.1.
- Gerrard, A. J., T. J. Kane, and J. P. Thayer, 2000, Year-round temperature and wave measurements of the Arctic middle Atmosphere for 1995– 1998, *Geophys. Monogr.*, 123(22), 213–219.
- Garcia, F., M. J. Taylor, and M. Kelley, 1997, Two-dimensional spectral analysis of mesospheric airglow image data, *Appl. Opt.*, 36(29).
- Hapgood, M., M. J. Taylor, 1982, Analysis of airglow image data, *Ann. Geophys.*, 38, 805–813.

- Hauchecorne, A, and Chanin, M.-L., 1980, Density and temperature profiles obtained by lidar between 35 and 70 km, *Geophys. Res. Lett.*, 7: 565–568, doi:10.1029/GL007i008p00565.
- Hecht, J. H., T. J. Kane, R. L. Walterscheid, C. S. Gardner, and C. A. Teplky, 1993, Simultaneous nightglow and Na lidar observations at Arecibo during the AIDA-89 campaign, *J. Atmos. Sol. Terr. Phys.*, 55, 409–423, doi:10.1016/0021-9169(93)90077-C.
- Hecht, J. H., R. L. Walterscheid, and M. N. Ross, 1994, First measurements of the two-dimensional horizontal wavenumber spectrum from CCD images of the nightglow, *J. Geophys. Res.*, 99(A6), 11,449 – 11,460.
- Hecht, J. H., R. L. Walterscheid, M. P. Hickey, and S. J. Franke, 2001, Climatology and modeling of quasi-monochromatic atmospheric gravity waves observed over Urbana Illinois, *J. Geophys. Res.*, 106(D6), 5181–5195, doi:10.1029/2000JD900722.
- Hoffmann, L., X. Xue, and M. J. Alexander, 2013, A global view of stratospheric gravity wave hotspots located with Atmospheric Infrared Sounder observations, *J. Geophys. Res.*, 118, 416–434, doi:10.1029/2012JD018658.
- Holton, J. R., and M. J. Alexander, 1999, Gravity waves in the mesosphere generated by tropospheric convection, *Tellus, Ser., A-B*, 51, 45–58.
- Holton, J. R., , 1982, The role of gravity wave induced drag and diffusion in the momentum budget of the mesosphere, *J. Atmos. Sci.*, 39, 791–799.
- Juramy, P., M. L. Chanin, G. Mégie, G. F. Toulinov, and Y. P. Doudoradov, 1981, Lidar sounding of the mesospheric sodium layer at high latitude, *J. Atmos. Terr. Phys.*, 43, 209–215.
- Kim, Y., C. Lee, J. K. Chung, J. H. Kim, and H. Y. Chun, 2010, Seasonal Variations of Mesospheric Gravity Waves Observed with an Airglow All-sky Camera at Mt. Ohyun, Korea (36°N), *J. Astron. Space Sci.*, 27(3), 181–188, doi:10.5140/JASS.2010.27.3.181.

- Kirchoff, V. W. J. H., and B. R. Clemesha, 1973, Atmospheric sodium measurements at 23°S, *J. Atmos. Terr. Phys.*, 35, 1493-1498.
- Krassovskij, V. I., N.N.Šefov, 1965, Airglow, *Space Sci. Rev.*, 4(2), 176–198, doi:10.1007/BF00173881.
- Krassovsky, V. I., 1972, Infrasonic variations of OH emissions in the upper atmosphere, *Ann. Geophys.*, 28, 739–746.
- Li, Z., A. Z. Liu, X. Lu, G. R. Swenson, and S. J. Franke, 2011, Gravity wave characteristics from OH airglow imager over Maui, *J. Geophys. Res.*, 116, D22115, doi:10.1029/2011JD015870.
- Lindzen, R. S., 1981, Turbulence and stress owing to gravity wave and tidal breakdown, *J. Geophys. Res.*, 86(C10), 9707–9714, doi:10.1029/JC086iC10p09707.
- Liu, A. Z., W. K. Hocking, S. J. Franke, and T. Thayaparan, 2002, Comparison of Na lidar and meteor wind measurements at Starfire Optical Range, NM, USA, *J. Atmos. Terr. Phys.*, 64, 31–40, doi:10.1016/S1364-6826(01)00095-5.
- Lu, X., A. Z. Liu, G. R. Swenson, T. Li, T. Leblanc, and I. S. McDermid (2009), Gravity wave propagation and dissipation from the stratosphere to the lower thermosphere, *J. Geophys. Res.*, 114, D11101, doi:10.1029/2008JD010112.
- Lu, X., C. Chen, W. Huang, J. A. Smith, X. Chu, T. Yuan, P.-D. Pautet, M. J. Taylor, J. Gong, and C. Y. Cullens (2015), A coordinated study of 1 h mesoscale gravity waves propagating from Logan to Boulder with CRRL Na Doppler lidars and temperature mapper, *J. Geophys. Res. Atmos.*, 120, 10,006–10,021, doi:10.1002/2015JD023604.
- Manson, A. H., and C. E. Meek, 1993, Characteristics of gravity waves (10 min-6 hours) at Saskatoon (52°N, 107°W): Observations by the phase coherent medium frequency radar, *J. Geophys. Res.*, 98, 20,357–20,367.
- Manson, A. H., 1990, Gravity Wave Horizontal and Vertical Wavelengths: An Update of Measurements in the Mesopause Region (~80–100 km), *J. Atmos. Sci.*, 47, 2765–2773, doi:10.1175/1520-0469(1990)047<2765:GWHAVW>2.0.CO;2.

Matsuno, T., 1982, A quasi one-dimensional model of the middle atmosphere circulation interacting with internal gravity waves, *J. Meteorol. Soc. Jpn.*, 60, 215–226.

McFarlane, N. A., 1987, The effect of orographically excited gravity wave drag on the general circulation of the lower stratosphere and troposphere, *J. Atmos. Sci.*, 44, 1775–1800, .

Medeiros, A. F., H. Takahashi, R. A. Buriti, K. M. Pinheiro, and D. Gobbi, 2005, Atmospheric gravity wave propagation direction observed by airglow imaging in the South American sector, *J. Atmos. Sol. Terr. Phys.*, 67, 1767–1773, doi:10.1016/j.jastp.2005.03.015.

Miller, M. J., T. N. Palmer, and R. Swinbank, 1989, Parameterization and influence of subgridscale orography in general circulation and numerical weather prediction models, *MAP Handbk.*, 40, 84–109.

Miller, M. J., et al., 2015, Upper atmospheric gravity wave details revealed in nightglow satellite imagery, *Proceedings of the National Academy of Sciences*, , doi:10.1073/pnas.1508084112.

Moreels, G., and M. Herse, 1977, Photographic evidence of waves around the 85 km level, *Planet. Space Sci.*, 25, 265–273.

Nakamura, T., T. Tsuda, M. Yamamoto, S. Fukao, and S. Kato, 1993, Characteristics of gravity waves in the mesosphere observed with the middle and upper atmosphere radar, 1, Momentum flux, *J. Geophys. Res.*, 98, 8899–8910.

Nakamura, T., T. Tsuda, S. Fukao, A. H. Manson, C. E. Meek, R. A. Vincent, and I. M. Reid, 1996, Mesospheric gravity waves at Saskatoon (52°N), Kyoto (35°N), and Adelaide (35°S), *J. Geophys. Res.*, 101, 7005–7012.

Nakamura, T., A. Higashikawa, T. Tsuda, and Y. Matsushita, 1999, Seasonal variations of gravity wave structures in OH airglow with a CCD imager at Shigaraki, *Earth Planets Space*, 51(7), 897–906, DOI: 10.1186/BF03353248.

Nakamura, T., T. Tsuda, R. Maekawa, M. Tsutsumi, K. Shiokawa, and T. Ogawa, 2001, Seasonal variation of gravity waves with various temporal and horizontal scales in the

MLT region observed with radar and airglow imaging, *Adv. Space Res.*, 27(10), 1737–1742, doi:10.1016/S0273-1177(01)00310-6.

Nakamura, T., T. Aono, T. Tsuda, G. A. Admiranto, E. Achmad, and Suranto, 2003, Mesospheric gravity waves over a tropical convective region observed by OH airglow imaging in Indonesia, *Geophys. Res. Lett.*, 30(17), 1882, doi:10.1029/2003GL017619.

Nappo, C.J., 2012, *An Introduction to Atmospheric Gravity Waves*, 2nd Edition, Academic Press: San Diego, CA.

Nielsen, K., M. J. Taylor, R. E. Hibbins, and M. J. Jarvis, 2009, Climatology of short-period mesospheric gravity waves over Halley, Antarctica (76°S, 27°W), *J. Atmos. Sol. Terr. Phys.*, 71(8–9), 991–1000, doi:10.1016/j.jastp.2009.04.005.

Nielsen, K., M. J. Taylor, R. E. Hibbins, M. J. Jarvis, and J. M. Russell III, 2012, On the nature of short-period mesospheric gravity wave propagation over Halley, Antarctica, *J. Geophys. Res.*, 117, D05124, doi:10.1029/2011JD016261.

Nozawa, S., et al., 2014, Variations of the neutral temperature and sodium density between 80 and 107 km above Tromsø during the winter of 2010–2011 by a new solid-state sodium lidar, *J. Geophys. Res.*, 119, 441–451, doi:10.1002/2013JA019520.

Palmer, T. N., G. J. Shutts, and R. Swinbank, 1986, Alleviation of a systematic westerly bias in general circulation and numerical weather prediction models through an orographic gravity wave drag parameterization, *Q. J. R. Meteorol. Soc.*, 112, 1001–10039, .

P.-D. Pautet, M. J. Taylor, W. R. Pendleton, Y. Zhao, T. Yuan, R. Esplin, and D. McLain, 2014, Advanced mesospheric temperature mapper for high-latitude airglow studies, *Appl. Opt.*, 53, 5934–5943 , doi:10.1364/AO.53.005934.

Perwitasari, S, et al., 2015, Coordinated airglow observations between IMAV/VISI and a ground-based all-sky imager on concentric gravity wave in the mesopause, *J. Geophys. Res.*, 120(A11), 9706–9721, doi:10.1002/2015JA021424.

Peterson, A. W., and L. M. Keiffaber, 1973, Infrared photography of OH airglow structures, *Nature*, 242:321–322.

- Peterson, A. W., 1979, Airglow events visible to the naked eye, *Appl. Opt.*, 18, 3390.
- Li Q., J. Xu, J. Yue, W. Yuan, and X. Liu, 2011, Statistical characteristics of gravity wave activities observed by an OH airglow imager at Xinglong, in northern China, *Ann. Geophys.*, 29, 1401–1410, doi:10.5194/angeo-29-1401-2011.
- Rauthe, M., M. Gerding, J. Höffner, and F.-J. Lübken, 2006, Lidar temperature measurements of gravity waves over Kühlungsborn (54°N) from 1 to 105 km: A winter-summer comparison, *J. Geophys. Res.*, 111, D24108, doi:10.1029/2006JD007354.
- Richter, E. S., and C. F. Sechrist, 1979, A meteor ablation-cluster ion atmospheric sodium theory, *Geophys. Res. Lett.*, 6: 183–186, doi:10.1029/GL006i003p00183.
- Rienecker, M. M., et al., 2011, MERRA: NASA's modern-era retrospective analysis for research and applications, *J. Clim.*, 24(14), 3624–3648, doi:10.1175/JCLI-D-11-00015.1.
- Rothwell, P., J. Crawford and N. Benjamin, 1976, Image Intensifying TV Observations in the 1975 Spacelab Assess Mission, *Atmospheric Physics from Spacelab*, 61, 343-355.
- Sakanoi, T, Y. Akiya, A. Yamazaki, Y. Otsuka, A. Saito, and I. Yoshikawa, 2011, Imaging observation of the earth's mesosphere, thermosphere and ionosphere by VISI of ISS-IMAP on the international space station, *IEEJ Trans. on Fundamentals and Materials*, 131, 12, pp.983-988, doi:10.1541/ieejfms.131.983.
- Satomura, T., and K. Sato, 1999, Secondary generation of gravity waves associated with the breaking of mountain waves, *J. Atmos. Sci.*, 56, 3847–3858.
- Sato, K., M. Kohma, M. Tsutsumi, and T. Sato, 2017, Frequency spectra and vertical profiles of wind fluctuations in the summer Antarctic mesosphere revealed by MST radar observations, *J. Geophys. Res. Atmos.*, 122, 3–19, doi:10.1002/2016JD025834.
- Senft, D. C., and C. S. Gardner, 1991, Seasonal variability of gravity wave activity and spectra in the mesosphere region at Urbana, *J. Geophys. Res.*, 96, 17,229–17,264, doi:10.1029/91JD01662.

She, C. Y., H. Latifi, J. R. Yu, R. J. Alvarez II, R. E. Bills, and C. S. Gardner, 1990, Two - frequency lidar technique for mesospheric Na temperature measurements, *Geophys. Res. Lett.*, 17, 929-932.

Shiokawa, K., Y. Katoh, M. Satoh, M. Ejiri, T. Ogawa, T. Nakamura, T. Tsuda, and R. Wiens, 1999, Development of optical mesosphere thermosphere imagers (OMTI), *Earth Planets Space*, 51, 887–896.

Shiokawa, K., Y. Katoh, M. Satoh, M. K. Ejiri, and T. Ogawa, 2000, Integrating-sphere calibration of all-sky cameras for nightglow measurements, *Adv. Space Res.*, 26(6), 1025–1028.

Suzuki, S., K. Shiokawa, Y. Otsuka, T. Ogawa, and P. Wilkinson, 2004, Statistical characteristics of gravity waves observed by an all-sky imager at Darwin, Australia, *J. Geophys. Res.*, 109, D20S07, doi:10.1029/2003JD004336.

Suzuki, S., K. Shiokawa, Y. Otsuka, T. Ogawa, K. Nakamura, and T. Nakamura, 2007a, A concentric gravity wave structure in the mesospheric airglow images, *J. Geophys. Res.*, 112, D02102, doi:10.1029/2005JD006558.

Suzuki, S., et al., 2007b, Gravity wave momentum flux in the upper mesosphere derived from OH airglow imaging measurements, *Earth Planets Space*, 59(5), 421–428.

Suzuki, S., K. Shiokawa, A. Z. Liu, Y. Otsuka, T. Ogawa, and T. Nakamura, 2009a, Characteristics of equatorial gravity waves derived from mesospheric airglow imaging observations, *Ann. Geophys.*, 27, 1625–1629.

Suzuki, S., K. Shiokawa, K. Hosokawa, K. Nakamura, and W. K. Hocking, 2009a, Statistical characteristics of polar cap mesospheric gravity waves observed by an all-sky airglow imager at Resolute Bay, Canada, *J. Geophys. Res.*, 114, A01311, doi:10.1029/2008JA013652.

Suzuki, S., M. Tsutsumi, S. E. Palo, Y. Ebihara, M. Taguchi, and M. Ejiri, 2011, Short-period gravity waves and ripples in the South Pole mesosphere, *J. Geophys. Res.*, 116, D19109, doi:10.1029/2011JD015882.

Suzuki, S., S. L. Vadas, K. Shiokawa, Y. Otsuka, S. Kawamura, and Y. Murayama, 2013a, Typhoon-induced concentric airglow structures in the mesopause region, *Geophys. Res. Lett.*, 40, 5983–5987, doi:10.1002/2013GL058087.

Suzuki, S., K. Shiokawa, Y. Otsuka, S. Kawamura, and Y. Murayama, 2013b, Evidence of gravity wave ducting in the mesopause region from airglow network observations, *Geophys. Res. Lett.*, 40, 601–605, doi:10.1029/2012GL054605.

Swenson, G. R., and C. S. Gardner, 1998, Analytical models for the responses of the mesospheric OH\* and Na layers to atmospheric gravity waves, *J. Geophys. Res.*, 103, 6271–6294, doi:10.1029/97JD02985.

Swenson, G. R., M. J. Taylor, P. J. Espy, C. S. Gardner, and X. Tao, 1995, ALOHA-93 measurements of intrinsic AGW characteristics using the airborne airglow imager and ground-based Na wind/temperature lidar, *Geophys. Res. Lett.*, 22, 2841–2844.

Taguchi, M., M. Ejiri, and K. Tomimatsu, 2004, A new all-sky optics for aurora and airglow imaging, *Adv. Polar Upper Atmos. Res.*, 18, 140–148.

Takahashi, T., et al., 2014, A case study of gravity wave dissipation in the polar MLT region using sodium LIDAR and radar data, *Ann. Geophys.*, 32, 1195-1205, doi:10.5194/angeo-32-1195-2014.

Takahashi, T., et al., 2015, A case study on generation mechanisms of a sporadic sodium layer above Tromsø (69.6°N) during a night of high auroral activity, *Ann. Geophys.*, 33, 941–953, doi:10.5194/angeo-33-941-2015.

Takeo, D., K. Shiokawa, H. Fujinami, Y. Otsuka, T. S. Matsuda, M. K. Ejiri, T. Nakamura, and M. Yamamoto, Sixteen-year variation of horizontal phase velocity and propagation direction of mesospheric and thermospheric waves in airglow images at Shigaraki, Japan, submitted to *J. Geophys. Res. Atmos.*.

Tanaka, Y., et al., 2013, Analysis software for upper atmospheric data developed by the IUGONET project and its application to polar science, *Adv Polar Sci*, 24(4): 231-240, doi: 10.3724/SP.J.1085.2013.00231.

Tang, J., A. Z. Liu, and G. R. Swenson, 2002, High frequency gravity waves observed in OH airglow at Starfire Optical Range, NM: Seasonal variations in momentum flux, *Geophys. Res. Lett.*, 29(20), 1966, doi:10.1029/2002GL015794.

Taylor, M. J., and M. Hapgood, 1988, Identification of a thunderstorm as a source of short period gravity waves in the upper atmospheric nightglow emissions, *Planet. Space Sci.*, 36(10), 975–985.

Taylor, M. J., and M. J. Hill, 1991, Near infrared imaging of hydroxyl wave structure over an ocean site at low latitudes, *Geophys. Res. Lett.*, 18, 1333-1336, doi:10.1029/91GL01299.

Taylor, M. J., P. J. Espy, D. J. Baker, R. J. Sica, P. C. Neal, and W. R. Pendleton Jr., 1991a, Simultaneous intensity, temperature, and imaging measurements of short period wave structure in the OH nightglow emission, *Planet. Space Sci.*, 39, 1171–1188.

Taylor, M. J., D. N. Turnbull, R. P. Lowe, 1991b, Coincident imaging and spectrometric observations of zenith OH nightglow structure, *Geophys. Res. Lett.*, 18, 1349–1352.

Taylor, M. J., E. H. Ryan, T. F. Tuan, and R. Edwards, 1993, Evidence of preferential directions for gravity wave propagation due to wind filtering in the middle atmosphere, *J. Geophys. Res.*, 98(A4), 6047–6057, doi:10.1029/92JA02604.

Taylor, M. J., M. B. Bishop, and V. Taylor, 1995a, All-sky measurements of short period waves imaged in the OI(557.7 nm), Na(589.2 nm), and near-infrared OH and O<sub>2</sub>(0,1) nightglow emissions during the ALOHA-93 campaign, *Geophys. Res. Letts.*, 22, 2833–2836.

Taylor, M. J., Y. Y. Gu, X. Tao, C. S. Gardner, and M. B. Bishop, 1995b, An investigation of intrinsic gravity wave signatures using coordinated lidar and nightglow imaging measurements, *Geophys. Res. Letts.*, 22, 2853–2856.

Taylor, M. J., W. R. Pendleton Jr., S. Clark, H. Takahashi, D. Gobbi, and R. A. Goldberg, 1997, Image measurements of short-period gravity waves at equatorial latitudes, *J. Geophys. Res.*, 102(D22), 26,283–26,299, doi:10.1029/96JD03515.

Taylor, M. J., et al., 2009, Characteristics of mesospheric gravity waves near the magnetic equator, Brazil, during the SpreadFEx campaign, *Ann. Geophys.*, 27, 461-472, doi:10.5194/angeo-27-461-2009.

Trenberth, K. (1991), Climate Diagnostics from Global Analyses: Conservation of Mass in ECMWF Analyses. *J. Climate*, 4, 707–722, doi: 10.1175/1520-0442(1991)004<0707:CDFGAC>2.0.CO;2.

Tsuda, T, Y. Murayama, M. Yamamoto, S. Kato, and S. Fukao, 1990, Seasonal variation of momentum flux in the mesosphere observed with the MU radar, *Geophys. Res. Lett.*, 17, 725–728.

Tsuda, T. T., et al., 2011, Fine structure of sporadic sodium layer observed with a sodium lidar at Tromsø, Norway, *Geophys. Res. Lett.*, 38, L18102, doi:10.1029/2011GL048685.

Tsutsumi, M, and T. Aso, 2005, MF radar observations of meteors and meteor-derived winds at Syowa (69°S, 39°E), Antarctica: A comparison with simultaneous spaced antenna winds, *J. Geophys. Res.*, 110, D24111, doi:10.1029/2005JD005849.

Tsutsumi, M., T. Aso, and M. Ejiri., 2001, Initial results of Syowa MF radar observations in Antarctica, *Adv. polar up. atmos. Res.*, 15, 103-116.

Vadas, S. L., and D. C. Fritts, 2001, Gravity wave radiation and mean responses to local body forces in the atmosphere, *J. Atmos. Sci.*, 58, 2249–2279.

Vadas, S. L., D. C. Fritts, and M. J. Alexander, 2003, Mechanism for the generation of secondary waves in wave breaking regions, *J. Atmos. Sci.*, 60, 194–214, doi:10.1175/1520-0469(2003)060<0194:MFTGOS>2.0.CO;2.

Vincent, R. A., and D. C. Fritts, 1987, A climatology of gravity waves in the mesosphere and lower thermosphere over Adelaide, Australia, *J. Atmos. Sci.*, 44, 748–760.

Vincent, R. A., and I. M. Reid, 1983, HF Doppler measurements of mesospheric momentum fluxes, *J. Atmos. Sci.*, 40, 1321– 1333.

Vincent, R. A., 1984, Gravity-wave motions in the mesosphere, *J. Atmos. Sol. Terr. Phys.*, 46(2), 119–128, doi:10.1016/0021-9169(84)90137-5.

Walterscheid, R. L., J. H. Hecht, R. A. Vincent, I. M. Reid, J. Woithe, and M. P. Hickey, 1999, Analysis and interpretation of airglow and radar observations of quasi-monochromatic gravity waves in the upper mesosphere and lower thermosphere over Adelaide, Australia Analysis and interpretation of airglow and radar observations of quasi-monochromatic gravity waves in the upper mesosphere and lower thermosphere over Adelaide, Australia(35°S, 138°E), *J. Atmos. Sol. Terr. Phys.*, 61, 461–478, doi:10.1016/S1364-6826(99)00002-4.

Whiteway, J. A., and A. I. Carswell, 1994, Rayleigh lidar observations of thermal structure and gravity wave activity in the high Arctic during a stratospheric warming, *J. Atmos. Sci.*, 51, 3122 – 3136, doi:10.1175/1520-0469(1994)051<3122:RLOOTS>2.0.CO;2.

Wilson, R., M. L. Chanin, and A. Hauchecorne, 1991, Gravity waves in the middle atmosphere observed by Rayleigh lidar 2. Climatology, *J. Geophys. Res.*, 96, 5169–5183, doi:10.1029/90JD02610.

Wrasse, C. M., et al., 2006, Mesospheric gravity waves observed near equatorial and low–middle latitude stations: Wave characteristics and reverse ray tracing results, *Ann. Geophys.*, 24(12), 3229–3240, doi:10.5194/angeo-24-3229-2006.

Yamada, Y., H. Fukunishi, T. Nakamura, and T. Tsuda, 2011, Break-down of small-scale quasi-stationary gravity wave and transition to turbulence observed in OH airglow, *Geophys. Res. Lett.*, 28, 2153–2156.

Yamashita, C., X. Chu, H.-L. Liu, P. J. Espy, G. J. Nott, and W. Huang, 2009, Stratospheric gravity wave characteristics and seasonal variations observed by lidar at the South Pole and Rothera, Antarctica, *J. Geophys. Res.*, 114, D12101, doi:10.1029/2008JD011472.

Yue, J., et al., 2009, Concentric gravity waves in the mesosphere generated by deep convective plumes in the lower atmosphere near Fort Collins, *J. Geophys. Res.*, 114, D06104, doi:10.1029/2008JD011244.

Yue, J., Miller, L. Hoffmann, and W. Straka III, 2014, Stratospheric and mesospheric concentric gravity waves over tropical cyclone Mahasen: Joint AIRS and VIIRS satellite observations, *J. Atmos. Sol. Terr. Phys.*, 119, 83-90, doi:10.1016/j.jastp.2014.07.003.

This thesis is based on the following papers:

Matsuda, T. S., T. Nakamura, M. K. Ejiri, M. Tsutsumi, and K. Shiokawa (2014), New statistical analysis of the horizontal phase velocity distribution of gravity waves observed by airglow imaging, *J. Geophys. Res. Atmos.*, 119, 9707–9718, doi:10.1002/2014JD021543.

Matsuda, T. S., T. Nakamura, M. K. Ejiri, M. Tsutsumi, Y. Tomikawa, M. J. Taylor, Y. Zhao, P. -D. Pautet, D. J. Marphy, T. Moffat-Griffin, Characteristics of mesospheric gravity waves over Antarctica observed by ANGWIN (Antarctic Gravity Wave Instrument Network) imagers using 3-D spectral analyses, submitted to *J. Geophys. Res. Atmos.*

# Tables

Table 4.1. Summary of the four airglow imagers used in this study; mLat represents the geomagnetic latitude.

Station	Lat, Lon	mLat	Institution	Airglow	Sampling		Detector Size
					Interval	Exposure	
Syowa (Japan)	69°S, 40°E	66S	NIPR	Na (589.0, 589.6nm)	1min	45s	512x512
Davis (Australia)	69°S, 78°E	77S	Utah State Univ.	OH (0.9-1.7μm)	10s	3s	320x256
McMurdo (USA)	78°S, 167°E	81S	Utah State Univ.	OH (0.9-1.7μm)	10s	3s	320x256
Halley (UK)	76°S, 27°W	67S	Utah State Univ.	OH (0.9-1.7μm)	10s	3s	320x256

\*The sampling intervals of the three imagers of Utah State University at Davis, Halley, and McMurdo are converted to one minute by averaging six images. We assume that the emission altitudes of Na and OH are 90 km and 87 km, respectively.

Station	Cloud [hour]	Aurora [hour]	Clear sky [hour]	Table
Syowa	151.8	79.8	32.3	4.2
Davis	252.2	62.0	21.3	Sky
McMurdo	271.8	22.0	22.6	conditi
Halley	285.5	0.00	22.2	on

cs at the four stations for April 6–May 21, 2013.



# Figures

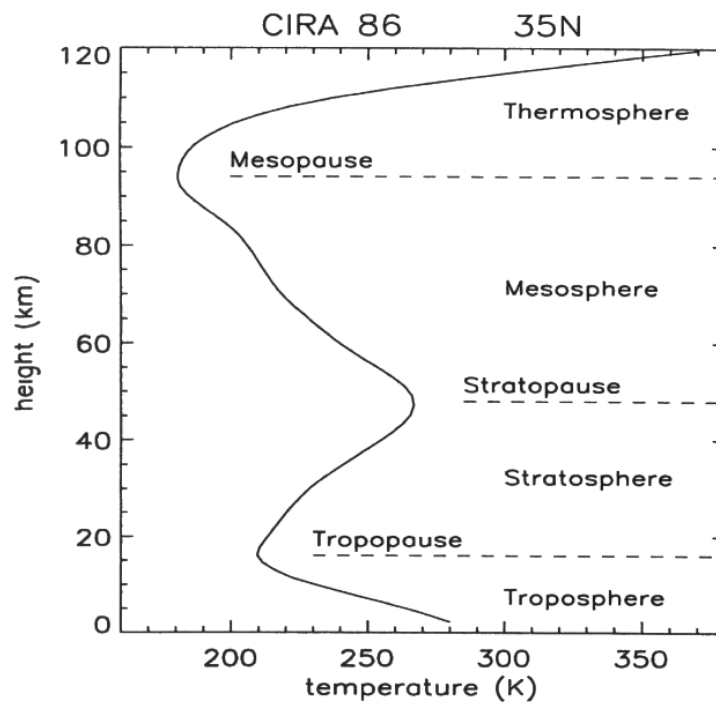


Figure 1.1: Vertical structure of the annual mean temperature of the Earth's atmosphere at 35°N from CIRA86 (COSPAR International Reference Atmosphere 1986) [Fleming *et al.*, 1988]

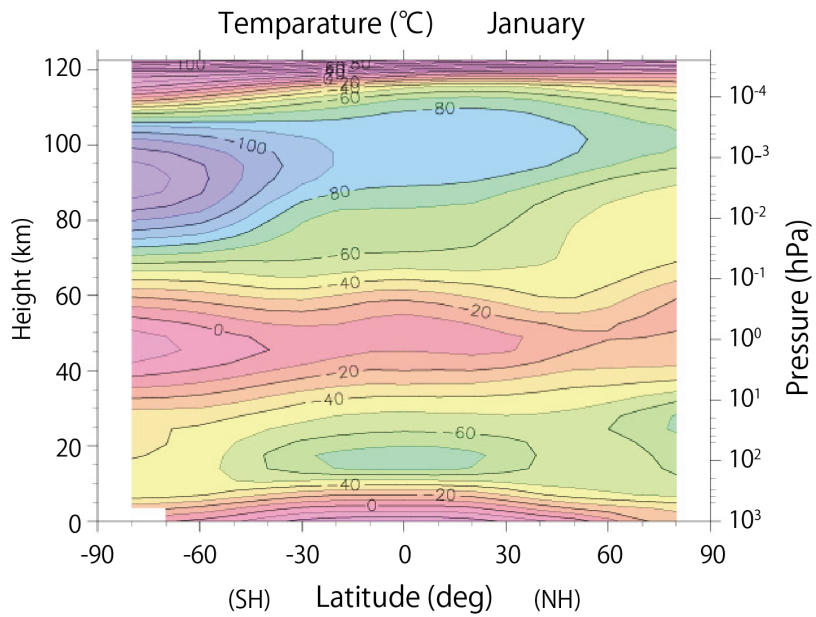


Figure 1.2: Zonal mean temperature in January from CIRA86 [Fleming *et al.*, 1988] as a function of the latitude and height. (Plot taken from <http://www-aos.eps.s.u-tokyo.ac.jp/~kaoru/Research/middle-atmosphere/index3.html>)

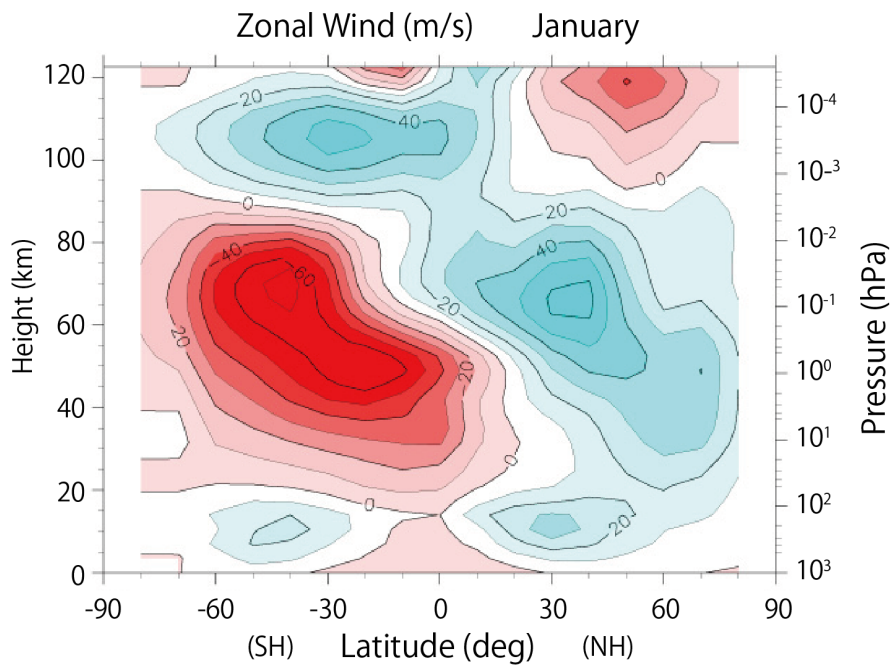


Figure 1.3: Zonal mean zonal wind in January from CIRA86 [Fleming *et al.*, 1988] as a function of the latitude and height. (Plot taken from <http://www-aos.eps.s.u-tokyo.ac.jp/~kaoru/Research/middle-atmosphere/index3.html>)

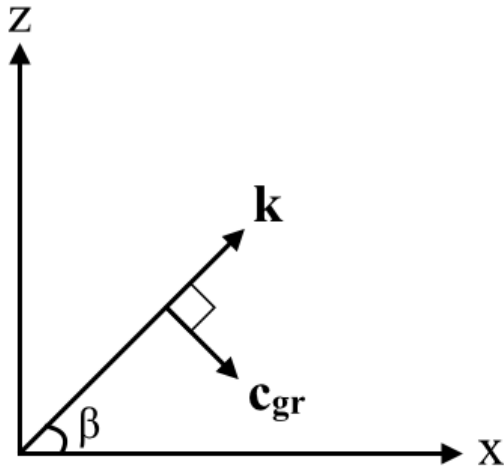


Figure 1.4: Relation between the wave number vector ( $\mathbf{k}$ ) and group velocity vector ( $\mathbf{C}_{gr}$ ) for an AGW;  $\beta$  is the angle of the wave number vector in the horizontal direction.

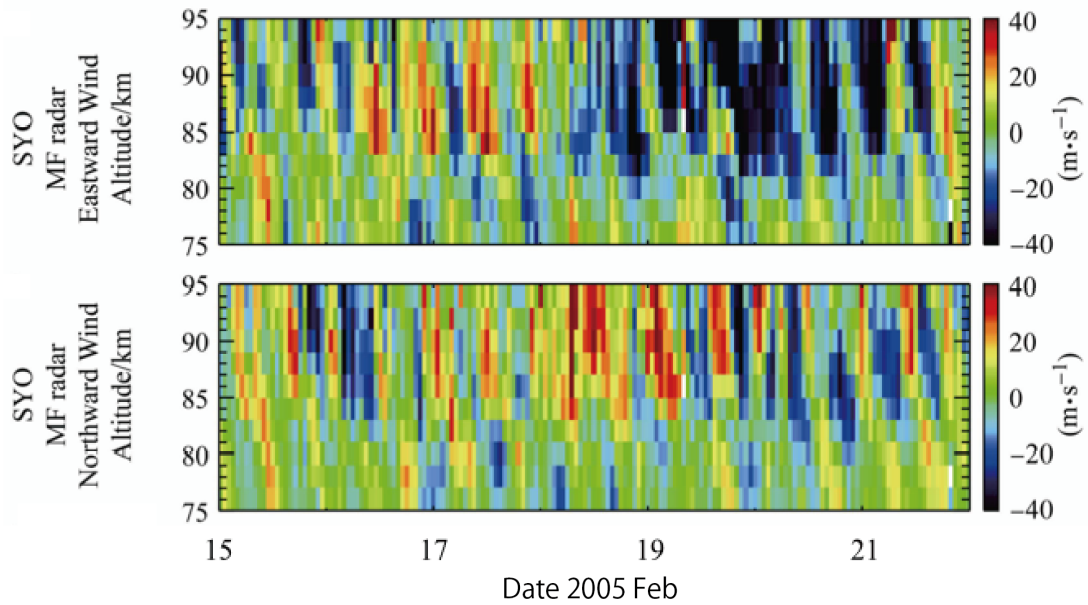


Figure 1.5: Time–height sections of (top) zonal and (bottom) meridional winds observed with the MF radar at the Syowa Station, Antarctic [Tanaka *et al.*, 2013].

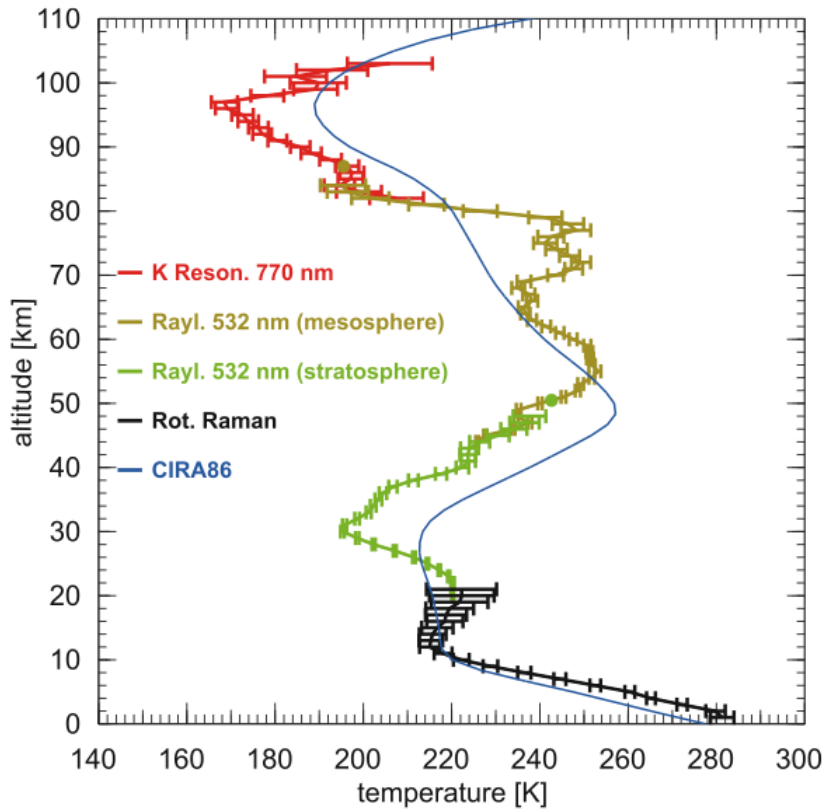


Figure 1.6: Vertical temperature profile above Kühlungsborn observed by a combination of two different lidars on November 12, 2003, 19:45-20:45 UT [Rauthe et al., 2006].

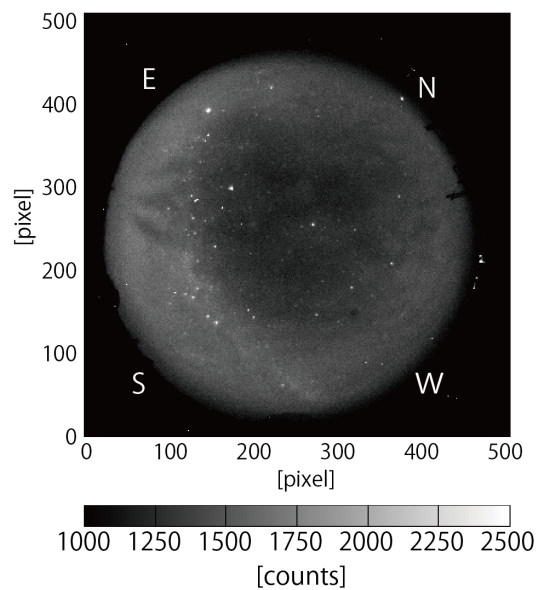


Figure 1.7: An example of an all-sky sodium airglow image with a size of  $512 \times 512$  pixels obtained at 23:24 UT on September 20, 2011, at the Syowa Station, Antarctica.

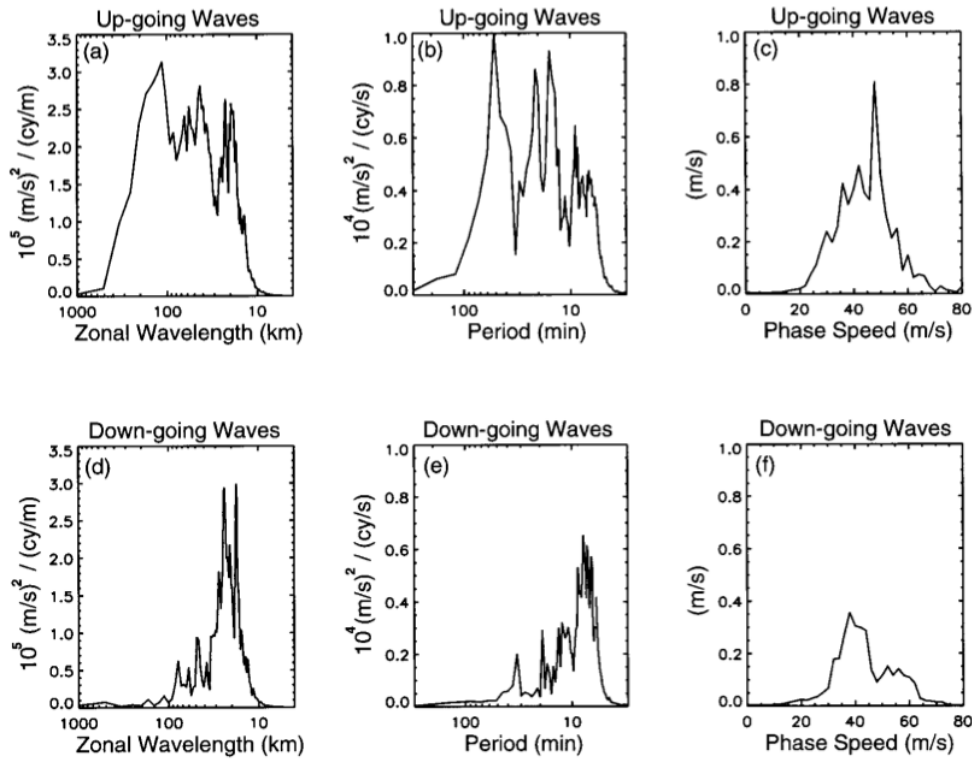


Figure 1.8: Power spectral density of the vertical wind velocities in the numerical model in the horizontal wavelength, period, and zonal phase speed domains [Holton and Alexander, 1999]. The up- and downgoing waves are separately plotted in the top and bottom panels. The power spectral density was derived from the region at the altitude of 60–70 km and the eastern half of the domain with a 2048-km width.

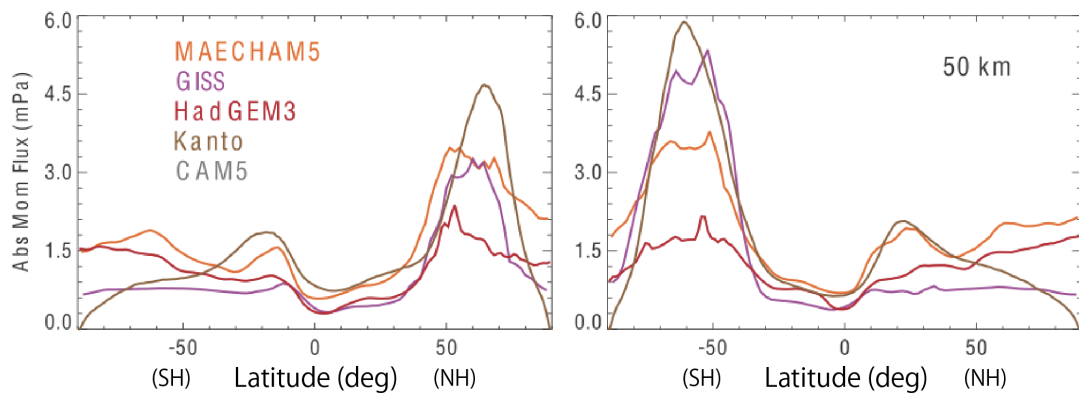


Figure 1.9: Comparison of the zonal mean absolute momentum fluxes by AGWs from HadGEM3, MAECHAM5, a version of the GISS model, Kanto model, and the CAM5 model at altitudes of 50 km for January (left) and July (right) of 2006 [Geller et al., 2013].

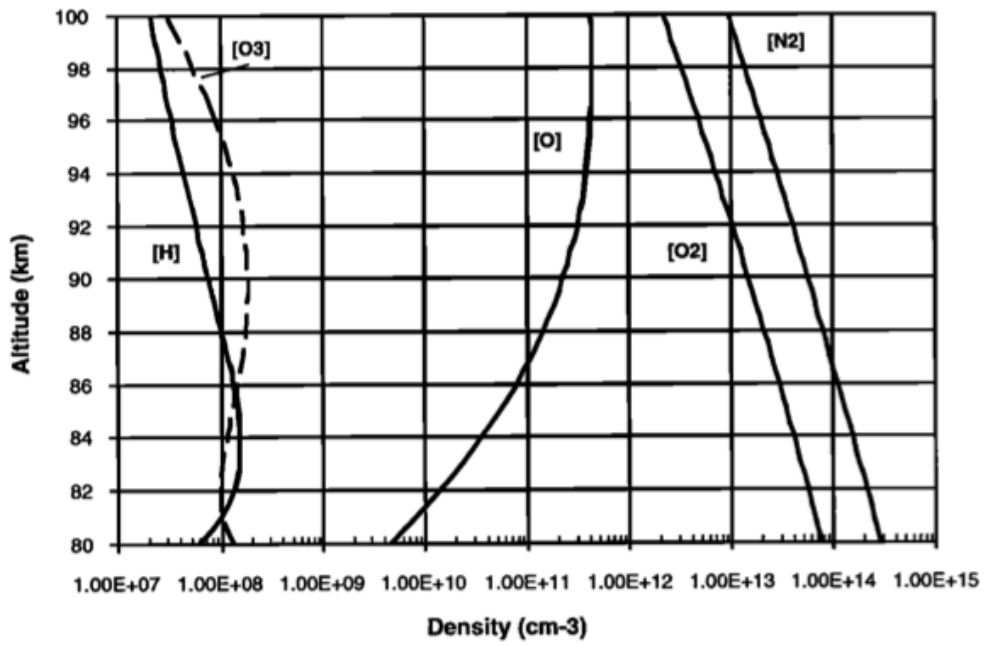


Figure 2.1: MSIS O, N<sub>2</sub>, O<sub>2</sub>, H, and computed O<sub>3</sub> profiles [Swenson and Gardner et al., 1998].

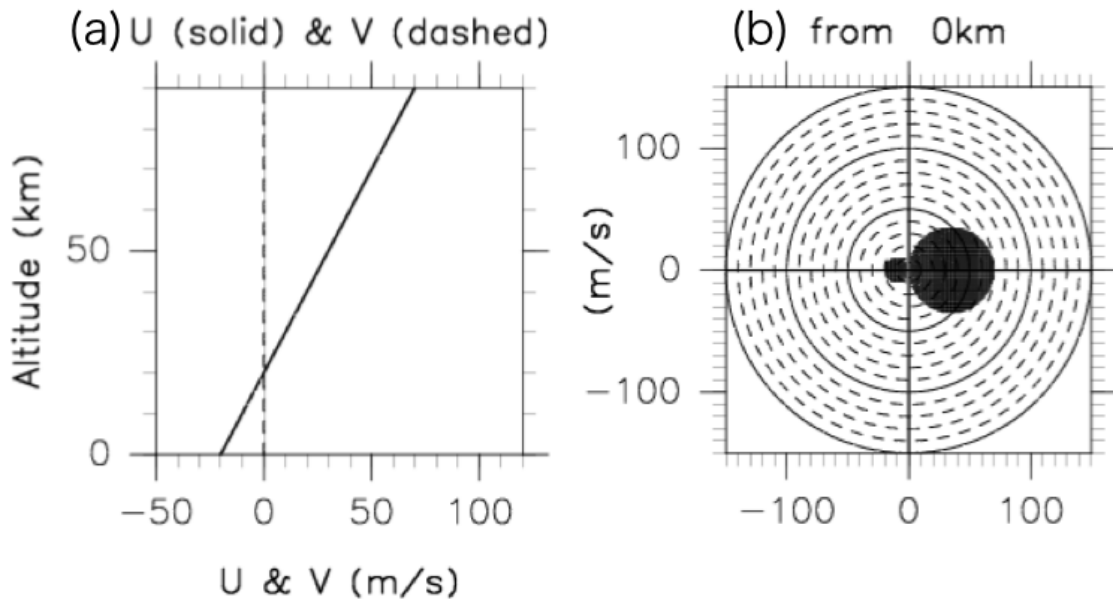


Figure 2.2: (a) Horizontal wind velocity profiles and (b) polar plot of the phase velocity.

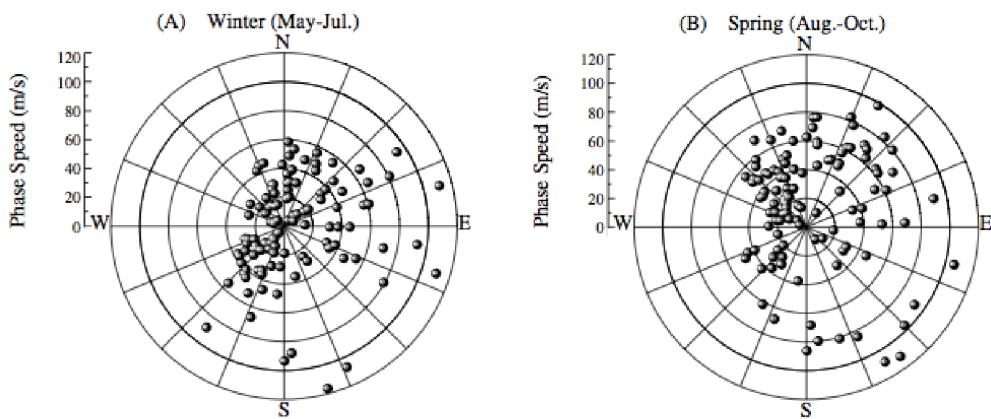


Figure 2.3: Phase velocity distribution of AGWs at 87 km observed by the airglow imager at Comandante Ferraz in 2007 [*Bageston et al.*, 2009].

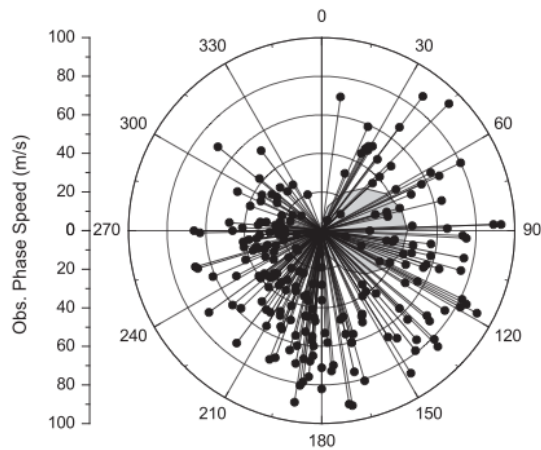


Figure 2.4: Phase velocity distribution of AGWs at 87 km observed by the airglow imager at Halley in 2000 and 2001 with a blocking diagram (shaded area) [Nielsen *et al.*, 2009].

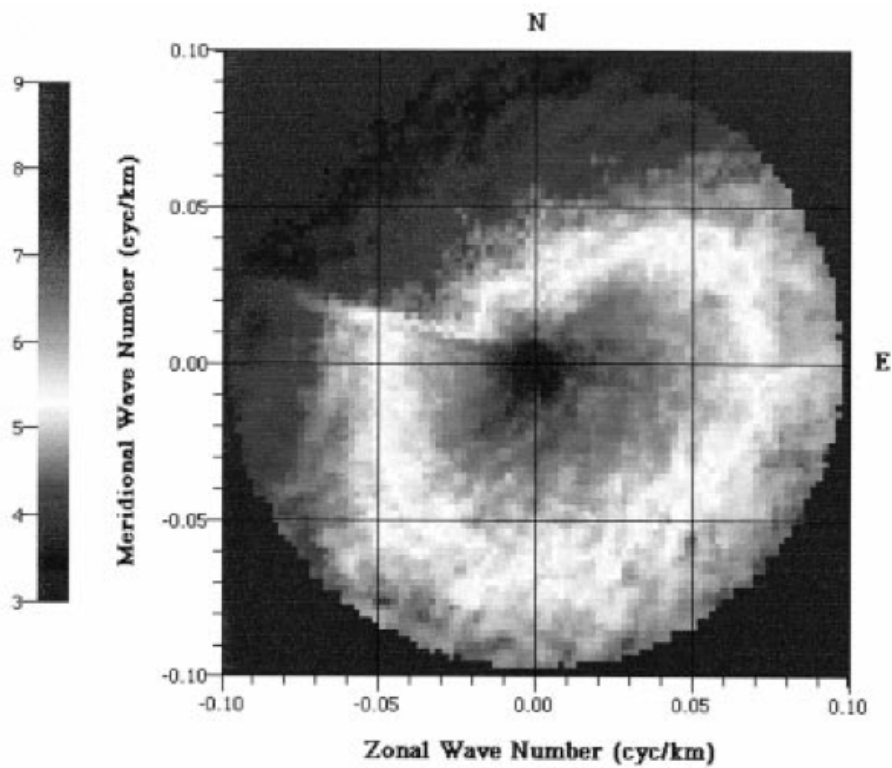


Figure 2.5: Contour plot of the unambiguous 2-D horizontal wavenumber spectrum at Starfire Optical Range (35°N, 107°W) on February 3, 1995 [Coble *et al.*, 1999]. The color scale represents the log of the square of the magnitude (cyc/m)<sup>2</sup>.

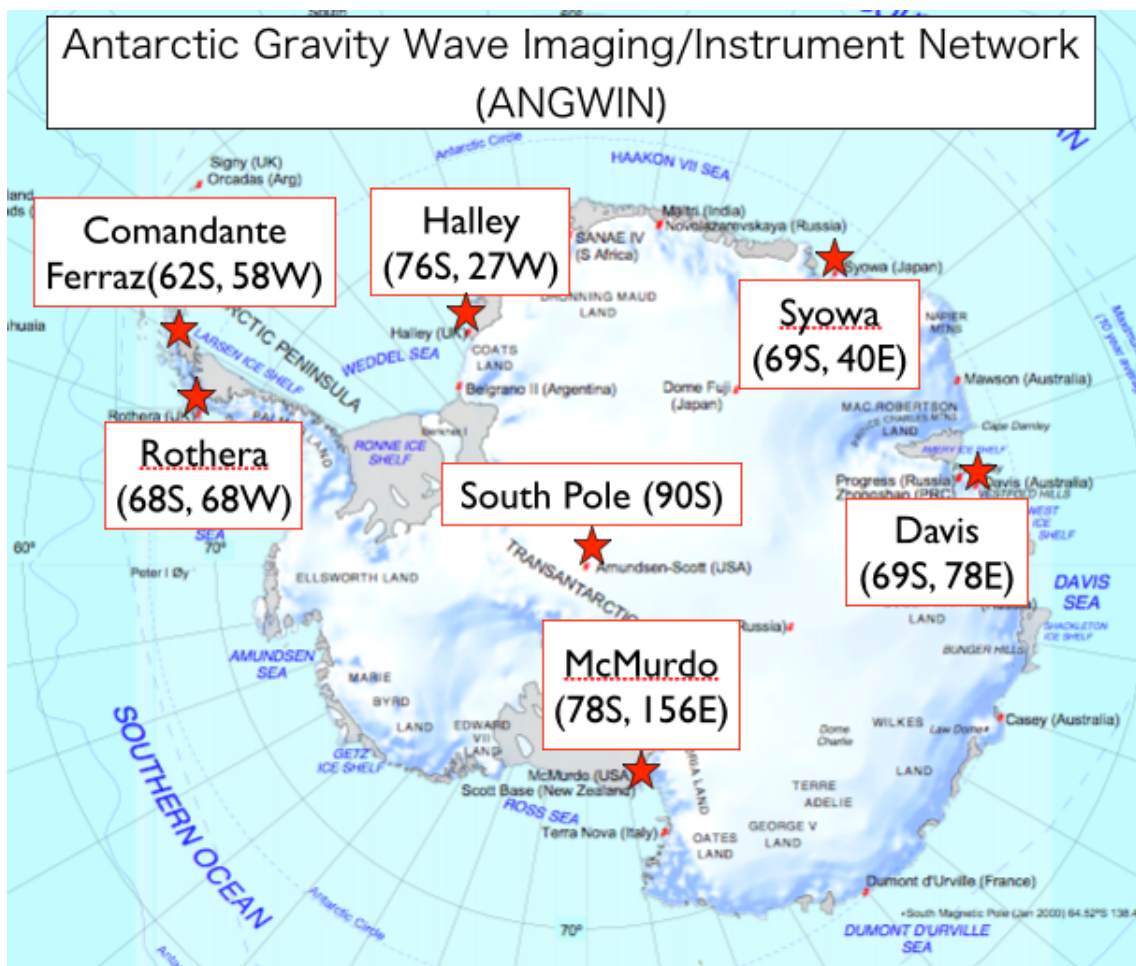


Figure 2.6: Map of the ANGWIN sites.

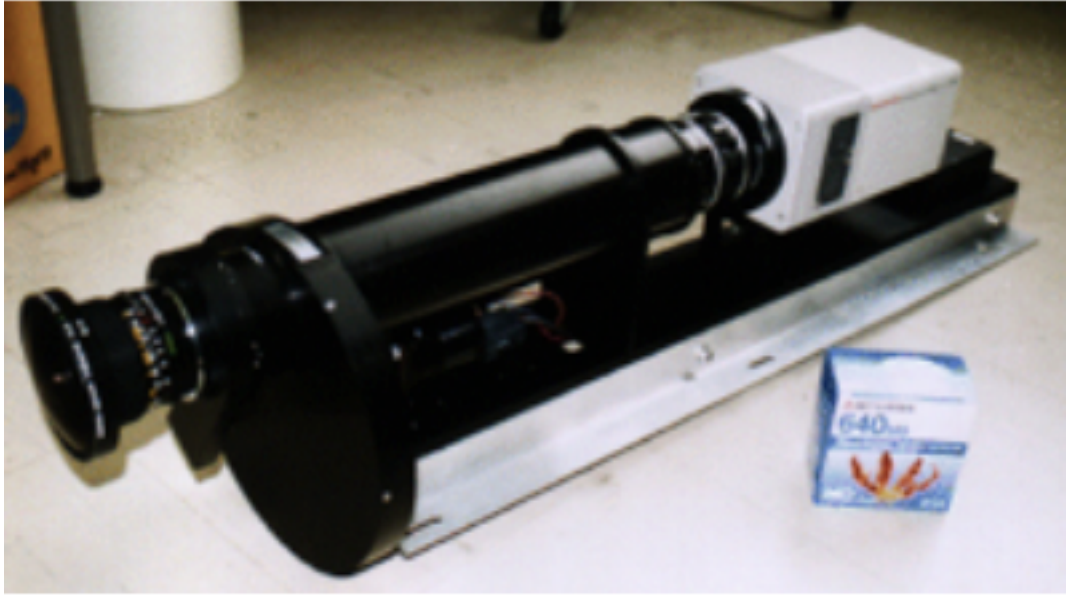


Figure 3.1: View of the all-sky imager of the Optical Mesosphere Thermosphere Imagers used in this study (OMTIs [Shiokawa *et al.*, 1999]).

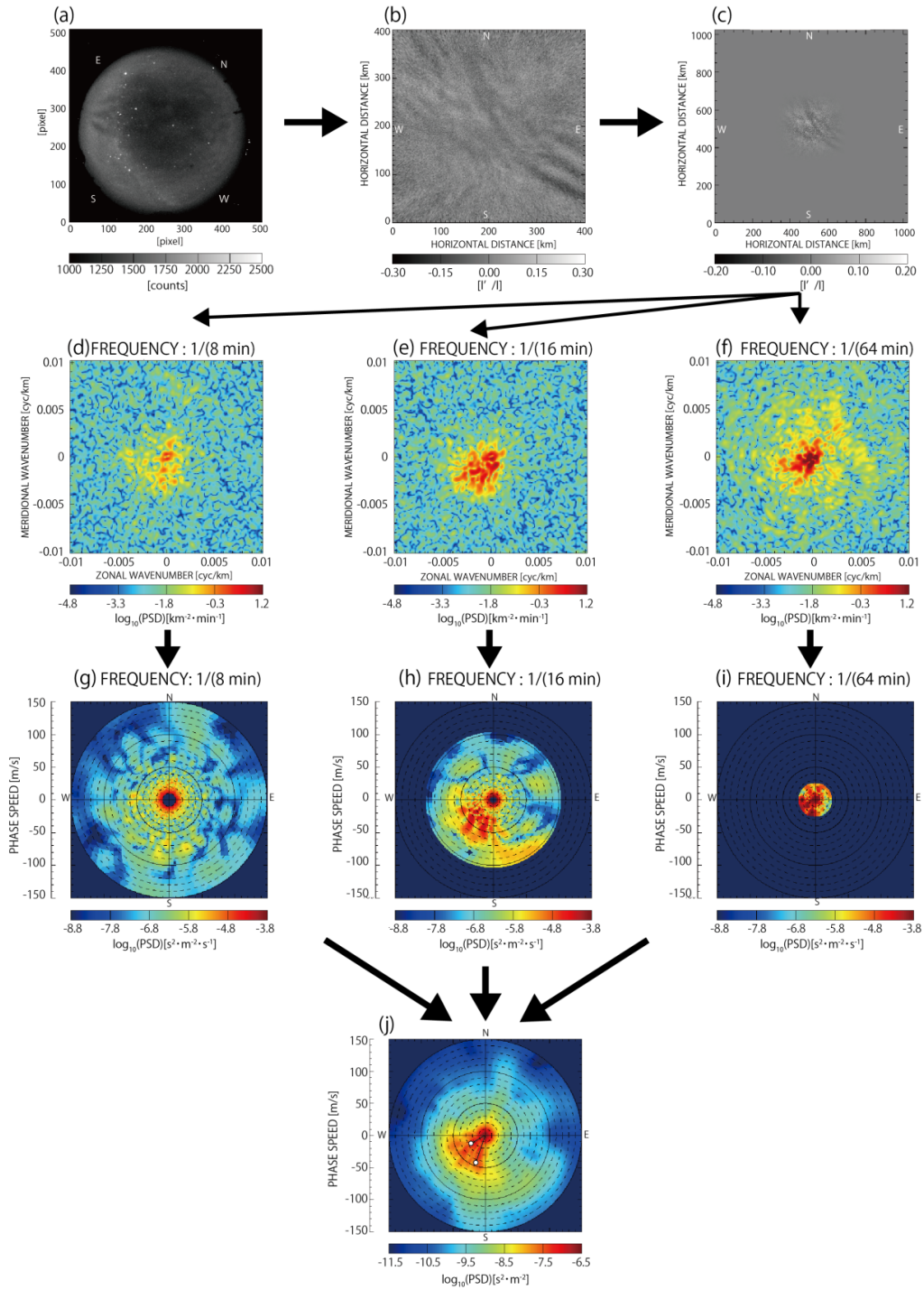


Figure 3.2: (a) Sodium airglow image with a size of  $512 \times 512$  pixels obtained at 23:24:00 on September 20, 2011, at the Syowa Station, Antarctic. (b) Processed image. (c) Image implanted at the center of the blank images. (d–f) Recolored power spectrum in the  $k$  and  $l$  domains. (g–i) The  $(v_x, v_y, \omega)$  power spectrum. (j) Power spectrum in the  $v_x$  and  $v_y$  domains.

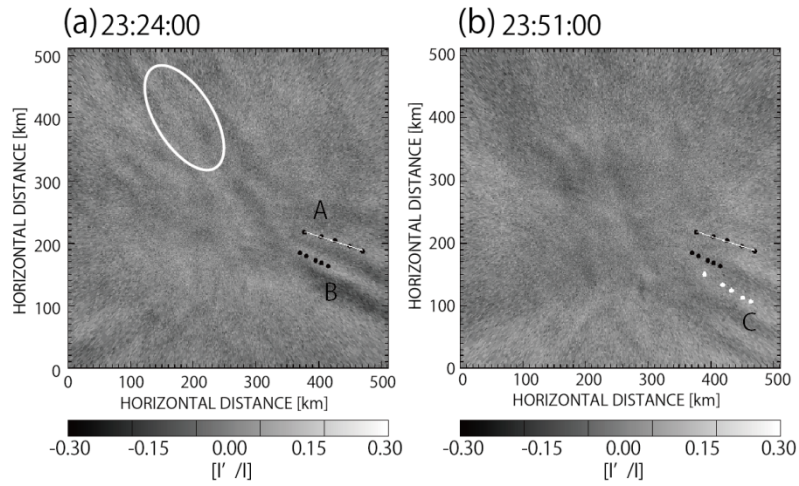


Figure 3.3: Airglow images captured at (a) 23:24:00 and (b) 23:51:00 on September 20, 2011. These images were used to extract wave parameters by event analysis (see text).

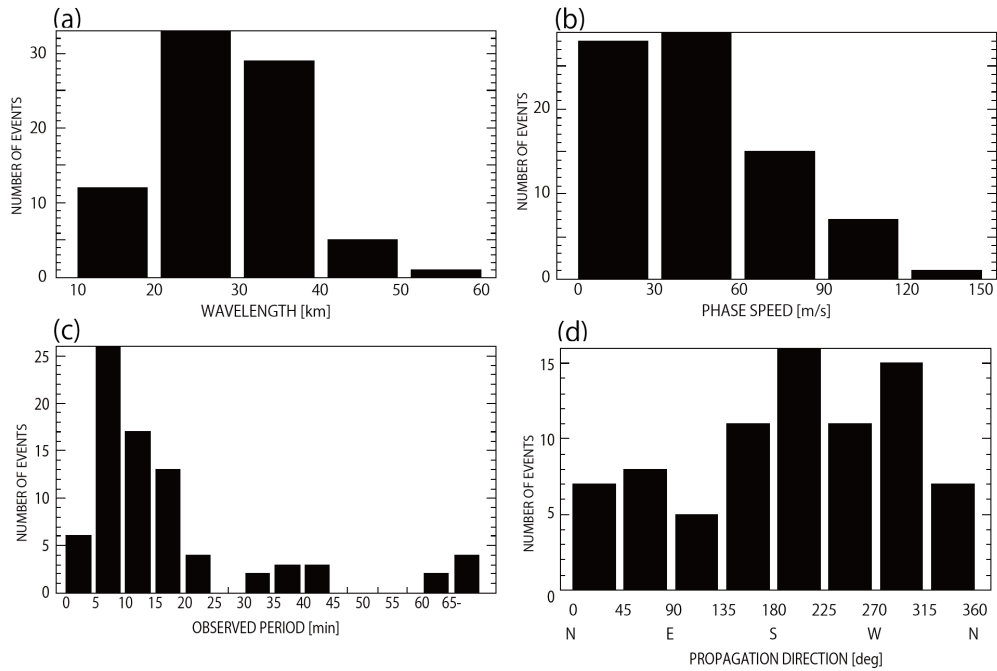


Figure 3.4: Distributions of the gravity wave parameters extracted by event analysis for the data from 2011 at the Syowa Station. (a) Horizontal wavelength, (b) horizontal phase speed, (c) observed wave period, and (d) horizontal propagation direction.

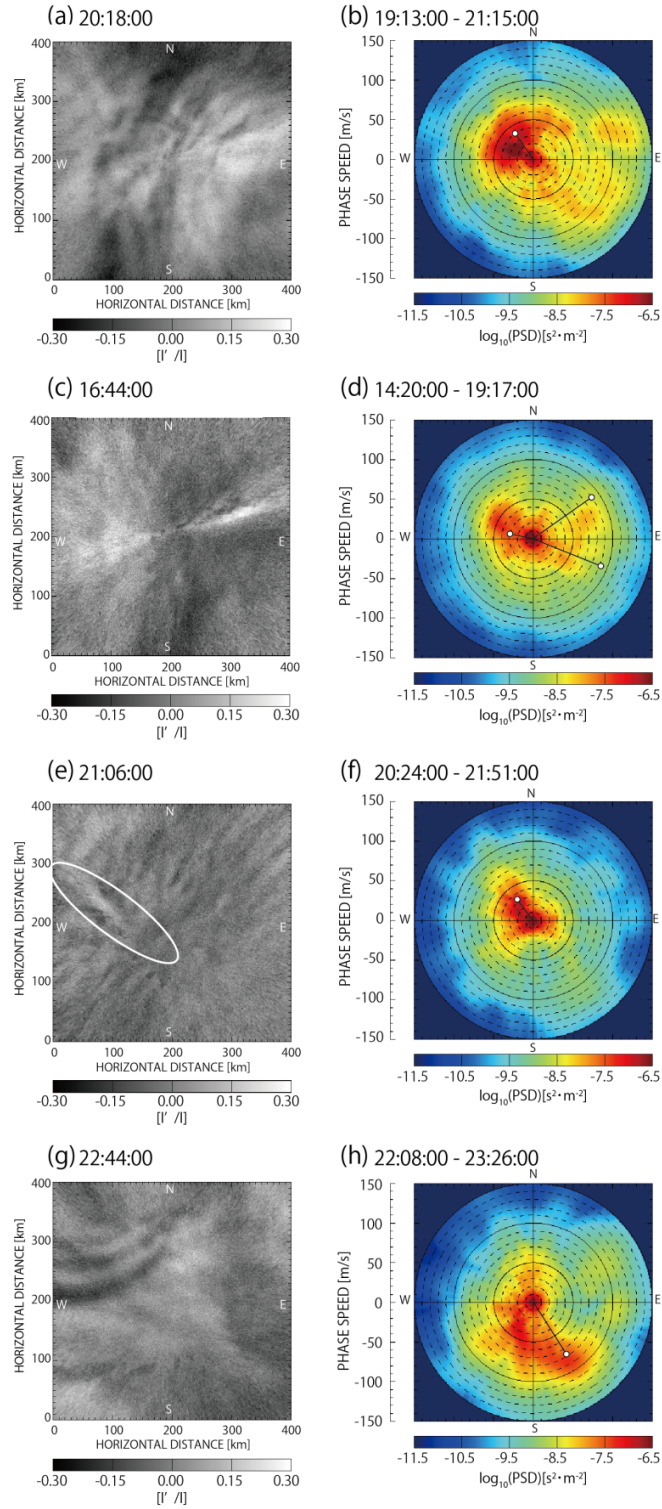


Figure 3.5: (a, c, e, and g) Airglow images processed in the same way as Figure 3.2b. (b, d, f, and h) Phase velocity power spectra for the corresponding time windows. White dots with solid black lines indicate the phase velocities determined by the event analysis.

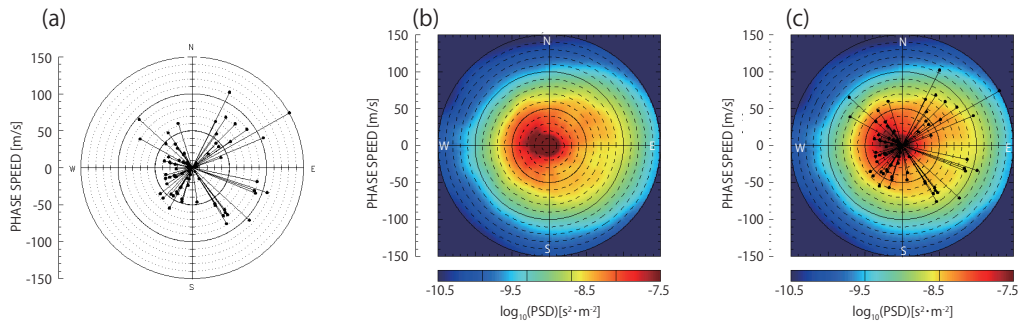


Figure 3.6: (a) Distribution of horizontal phase velocities observed in 2011 extracted by event analyses. (b) The average power spectrum of airglow intensity variations in the horizontal phase velocity domain in 2011. (c) Same as (b) with an overlay of (a).

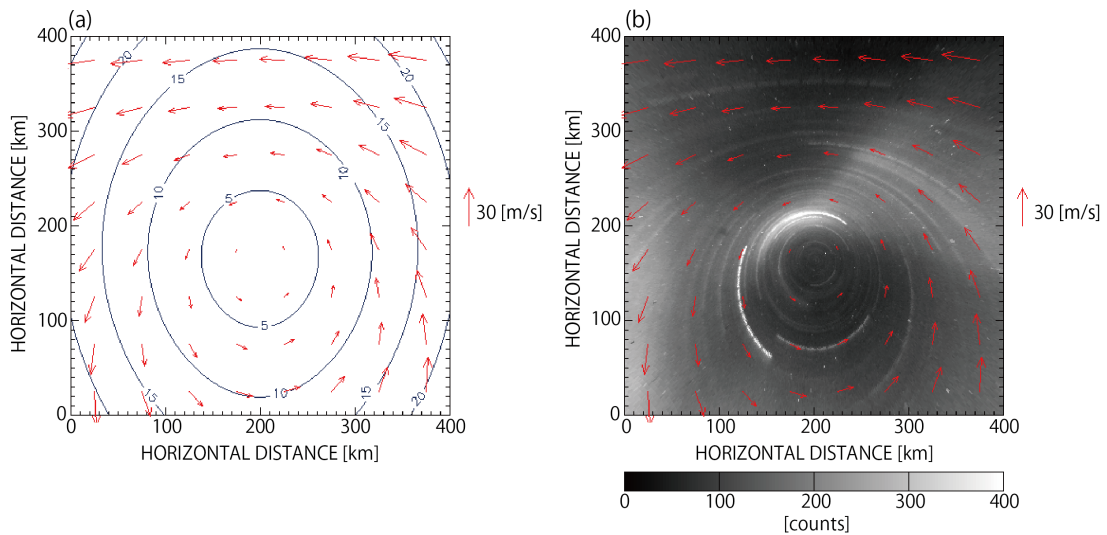
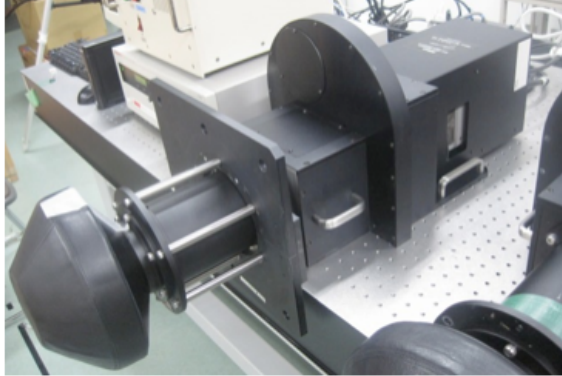


Figure 3.7: The apparent speed of stars assuming the virtual height of 90 km in the image data projected onto the geographic coordinates. (a) Contour plot of the apparent speed with apparent velocity vectors (red arrows). (b) Averaged airglow images processed in the same way as Figure 3.2b but without the removal of stars. The red arrows are the same as in (a).

(a)



(b)



Figure 4.1: (a) View of the all-sky imager at Syowa, and (b) an example picture of airglow imagers used at Davis, Halley, and McMurdo.

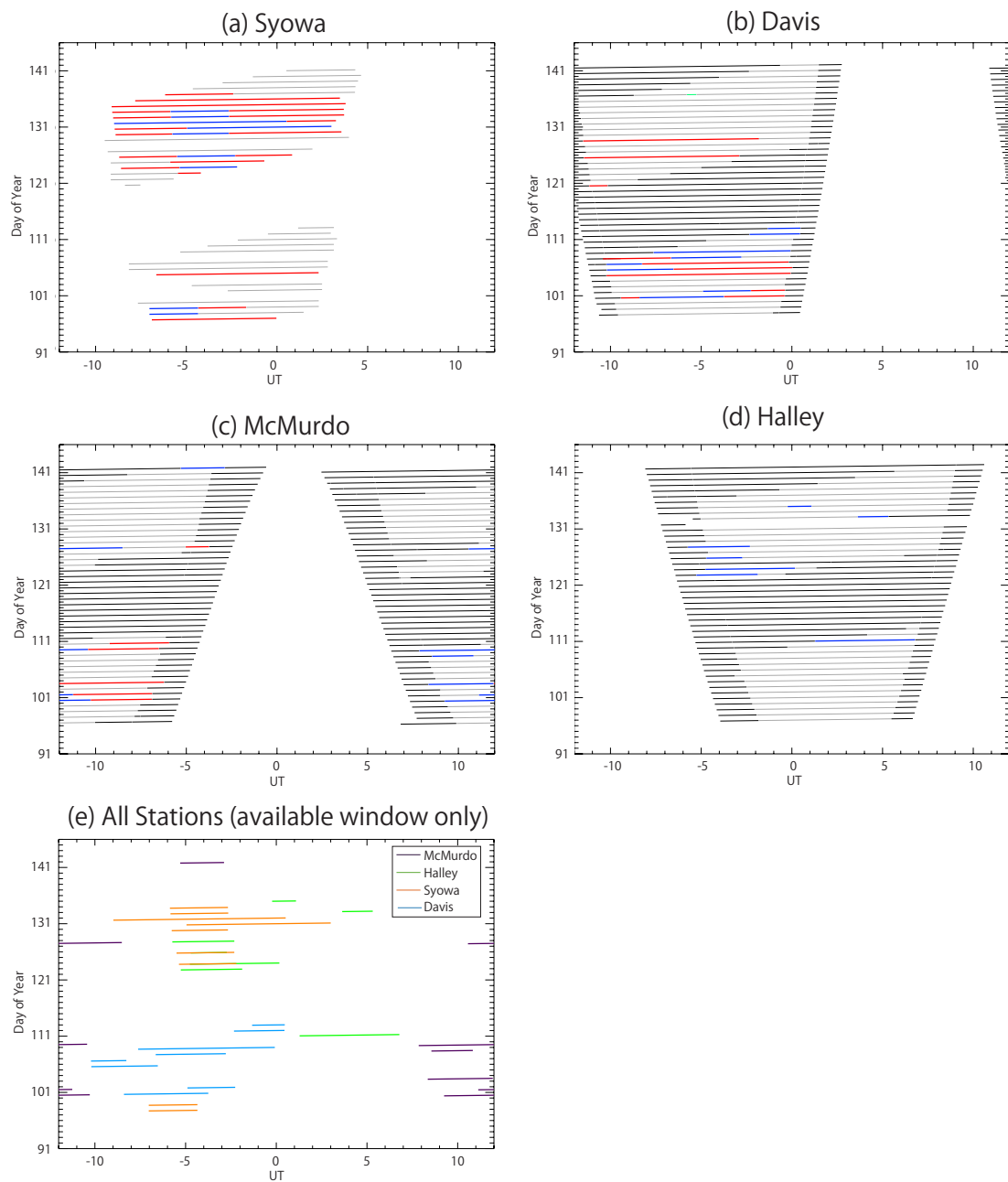


Figure 4.2: (a–d) Observation time of imagers at each ANGWIN site used in this study. The horizontal axis is the time of day in UT. The vertical axis is the day of the year in 2013. The color shows the sky condition. Blue, red, and gray represent clear sky, auroral contamination, and cloudy, respectively. The thick black lines indicate twilight or moonlight. (e) Summary of the time of clear sky at the four stations. Different colors show different observation sites.

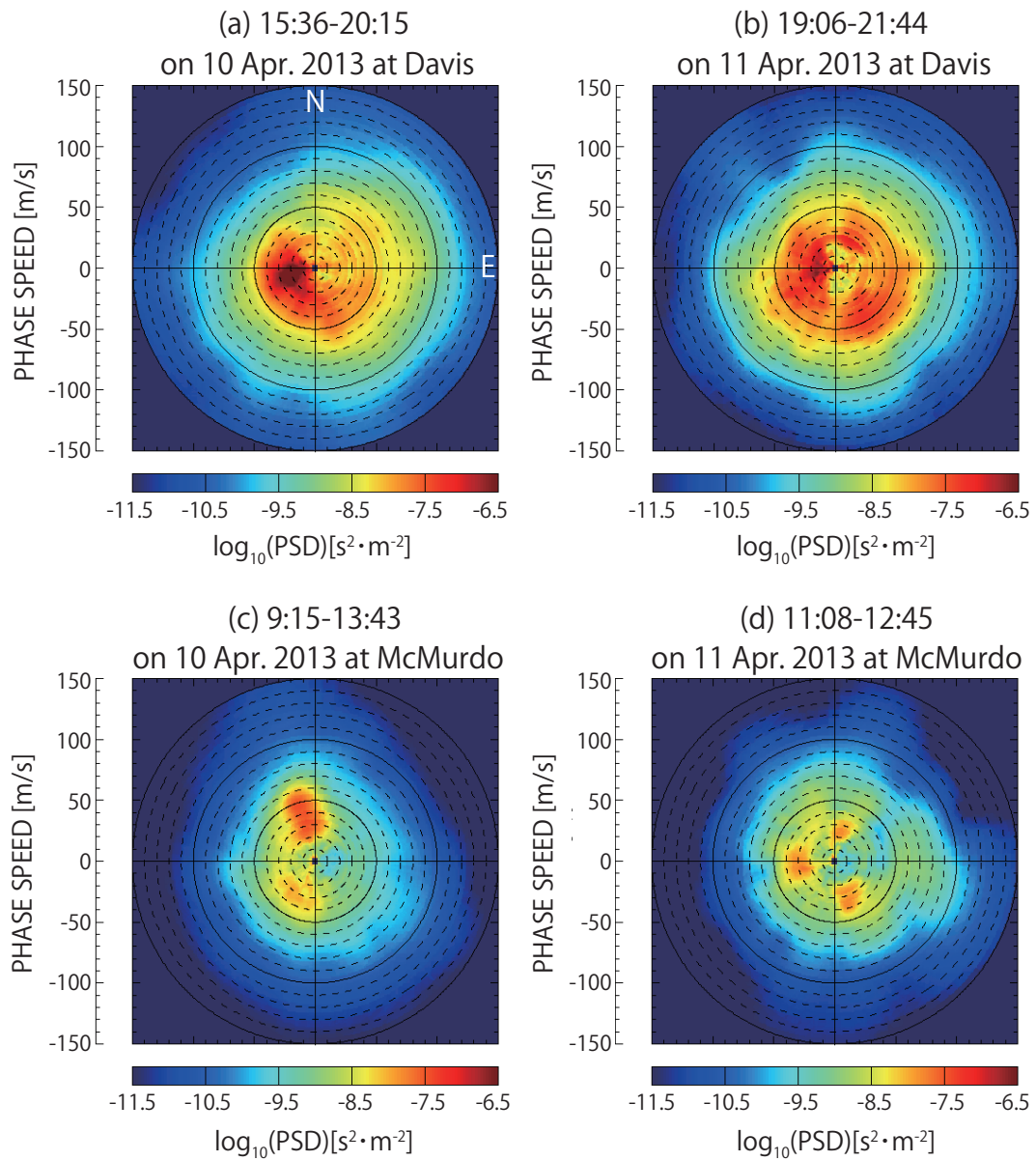


Figure 4.3: Phase velocity spectra of two consecutive nights, April 10 (left) and 11 (right), 2013, at Davis (top) and McMurdo (bottom).

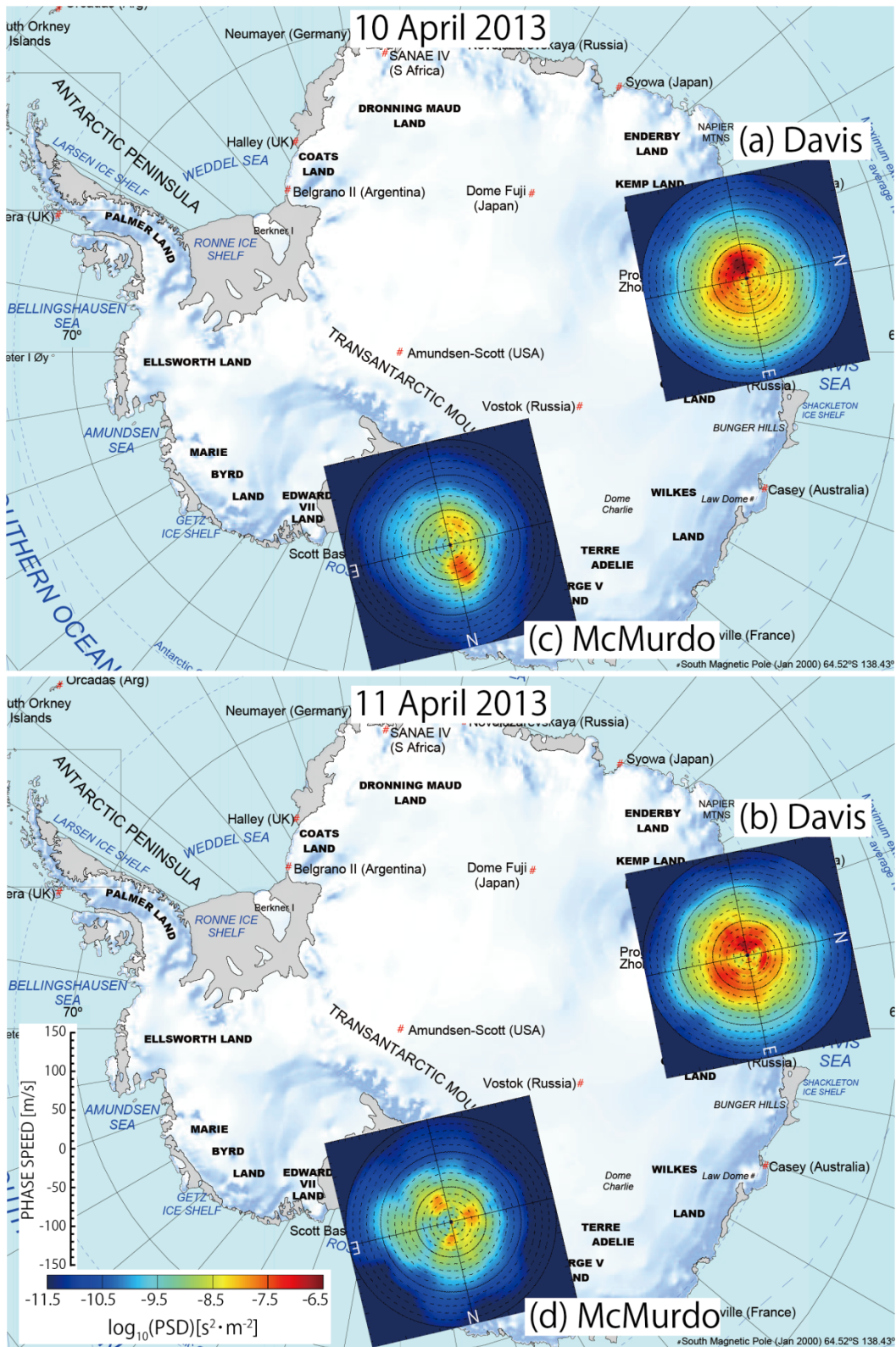


Figure 4.4: Phase velocity spectra, which are the same as Figure 4.3, except for being overlain on the map of the Antarctic.

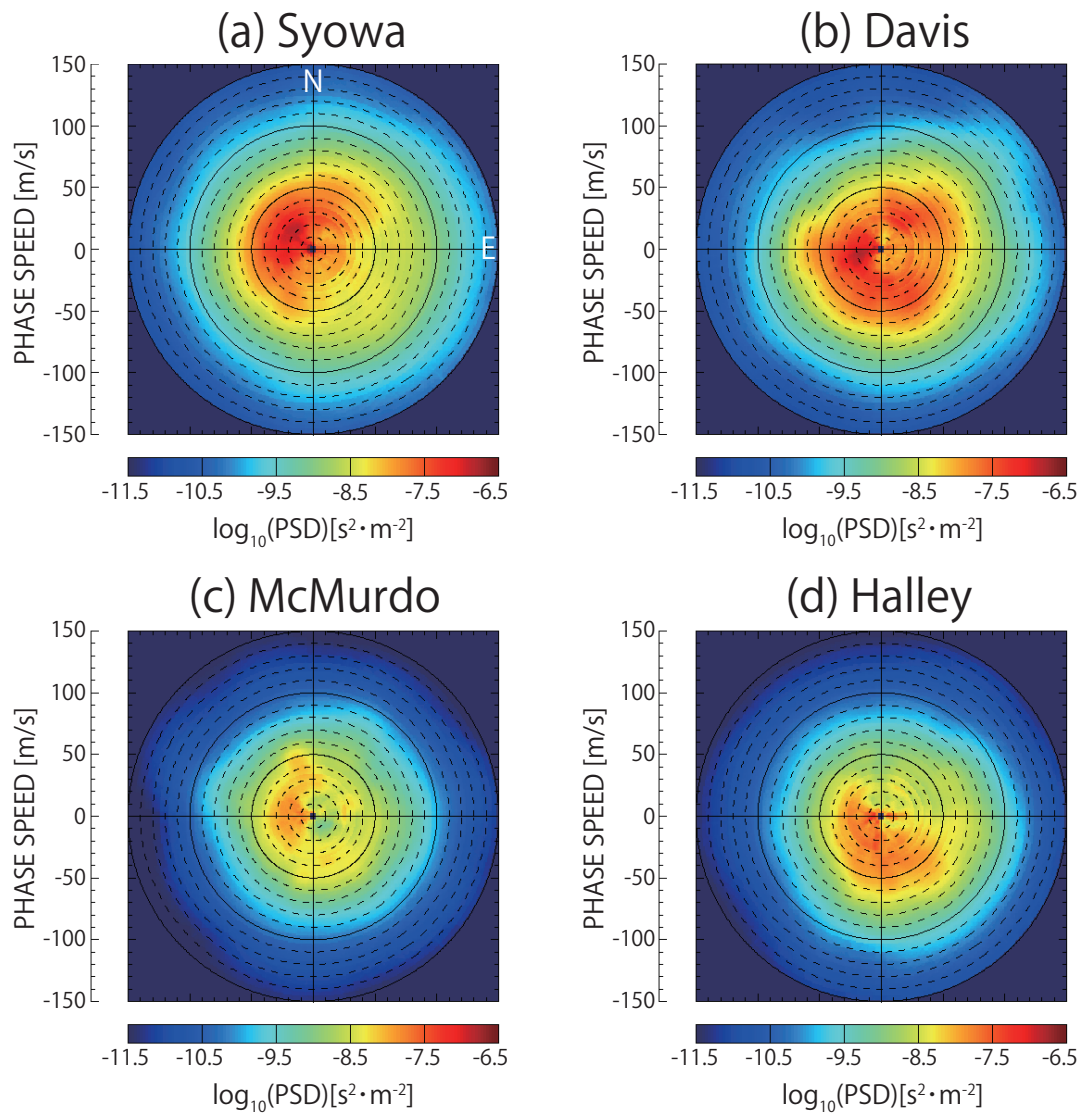


Figure 4.5: Phase velocity spectra averaged for the clear sky nights between April 6 and May 21, 2013, observed at (a) Syowa, (b) Davis, (c) McMurdo, and (d) Halley.

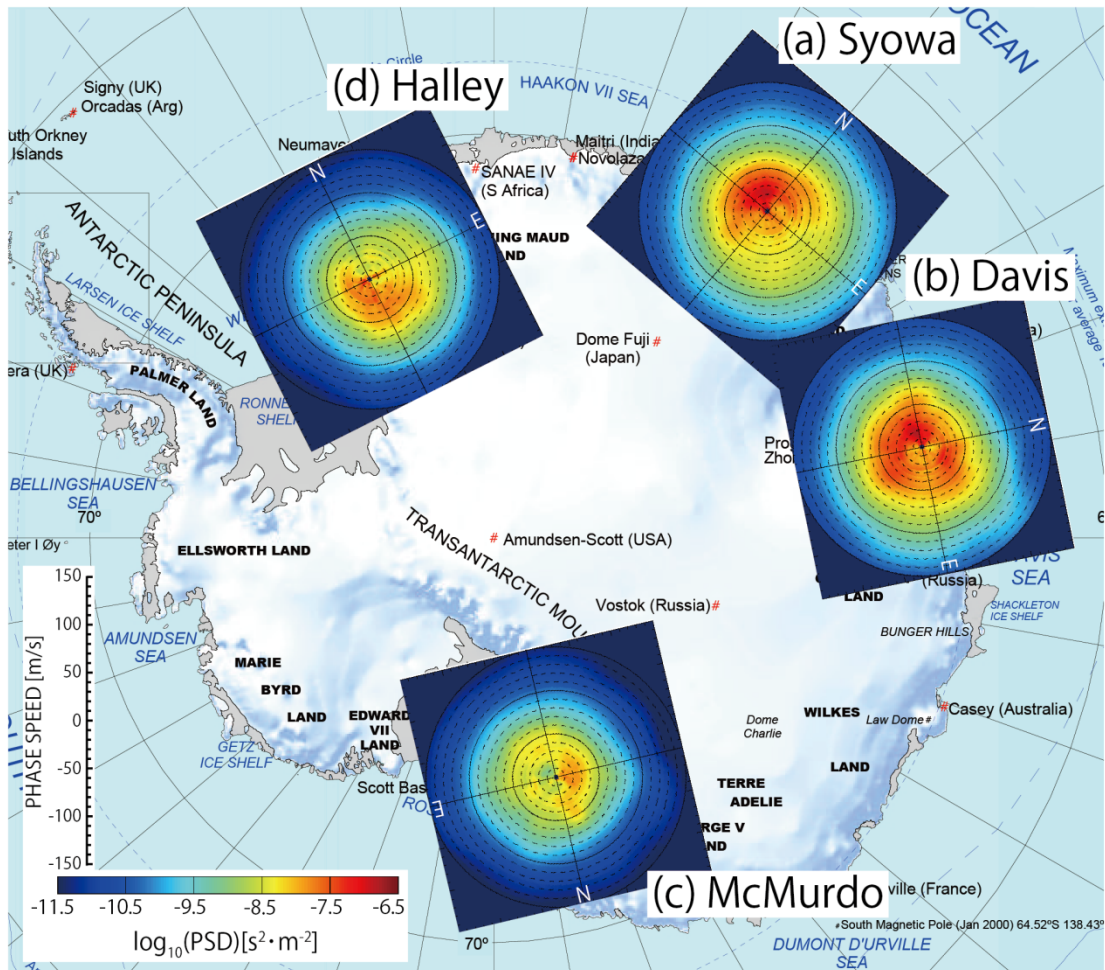


Figure 4.6: Phase velocity spectra, which are the same as Figure 4.5, except for being overlain on the map of the Antarctic.

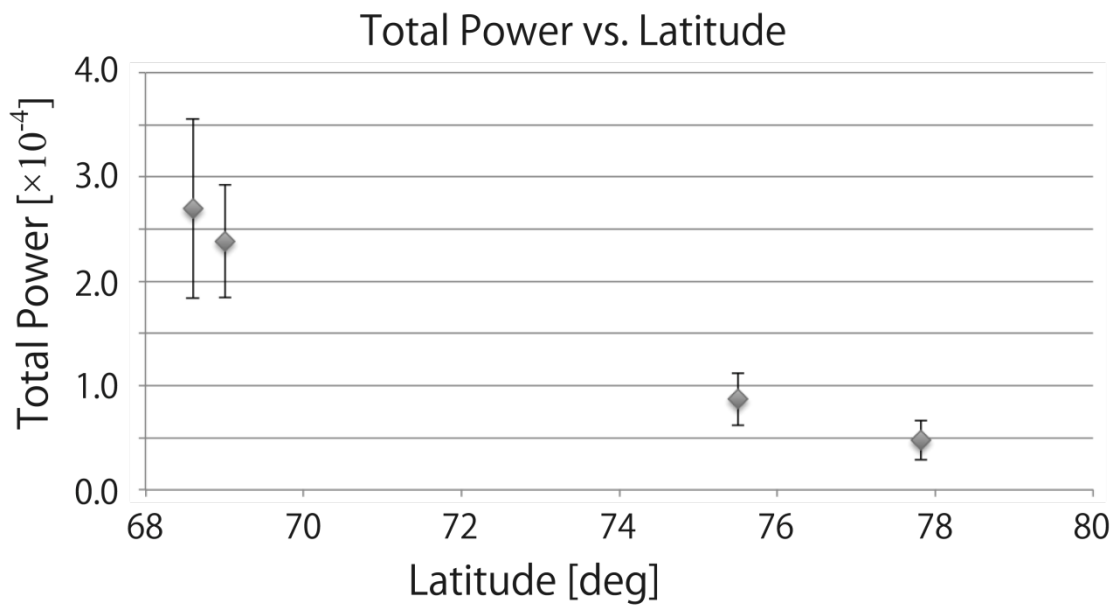


Figure 4.7: Total power of the averaged spectra, which corresponds to the variance of relative intensity variations,  $I'/I$ , plotted as a function of latitude. The error bar shows the standard deviation of nightly averaged data.

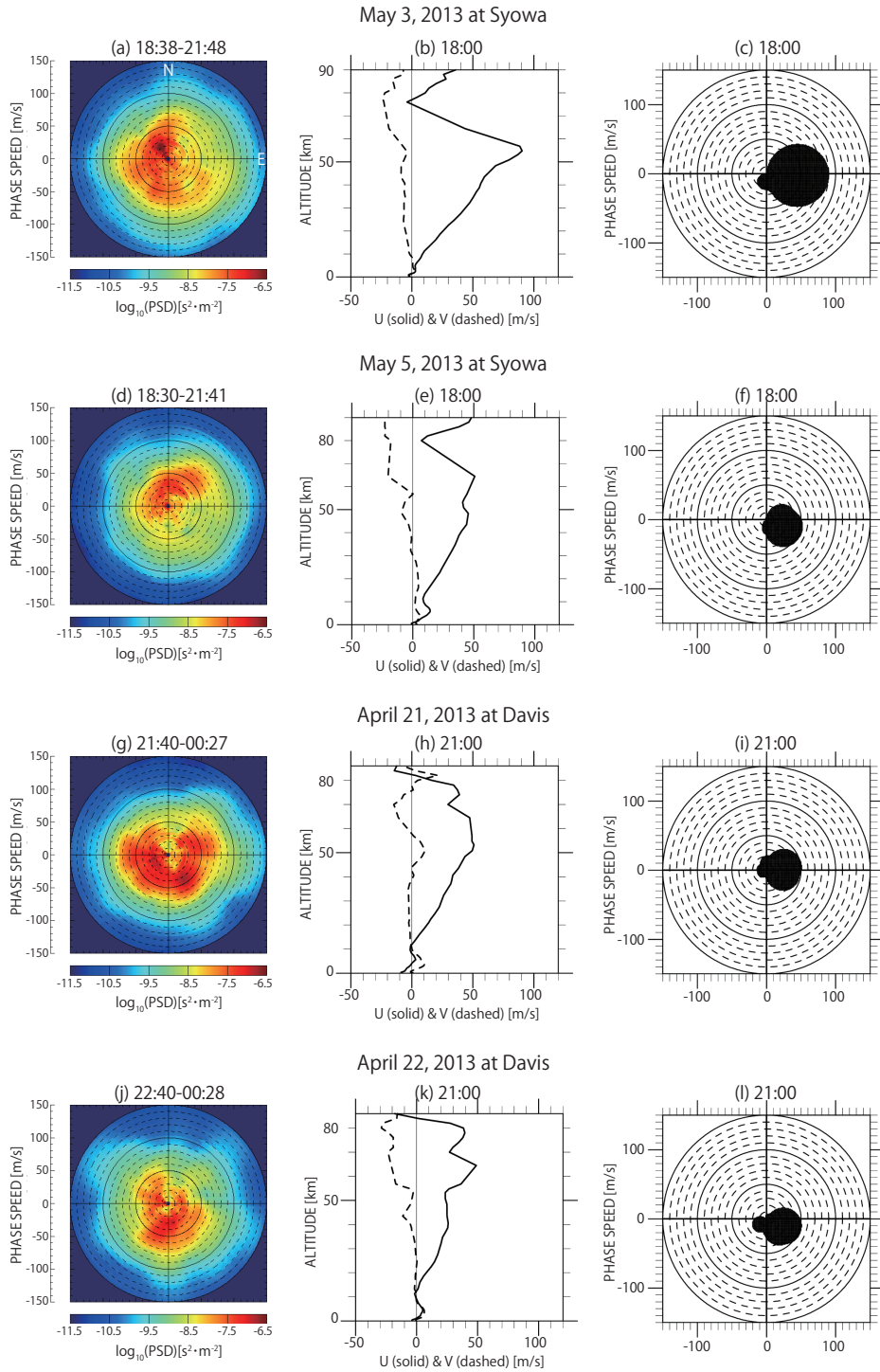


Figure 4.8: (a) Phase velocity spectra at 18:38–21:48 UT on May 3, 2013, at Syowa. (b) Zonal (solid) and meridional (dashed) wind velocity profiles at 18:00 UT on May 3, 2013. (c) Blocking diagram for the wind profiles shown in (b). (d–l) The same as the top panels except for (d, e, and f) May 5, 2013, (g, h, and i) April 21, 2013, at Davis, and (j, k, and l) April 22, 2013, at Davis.

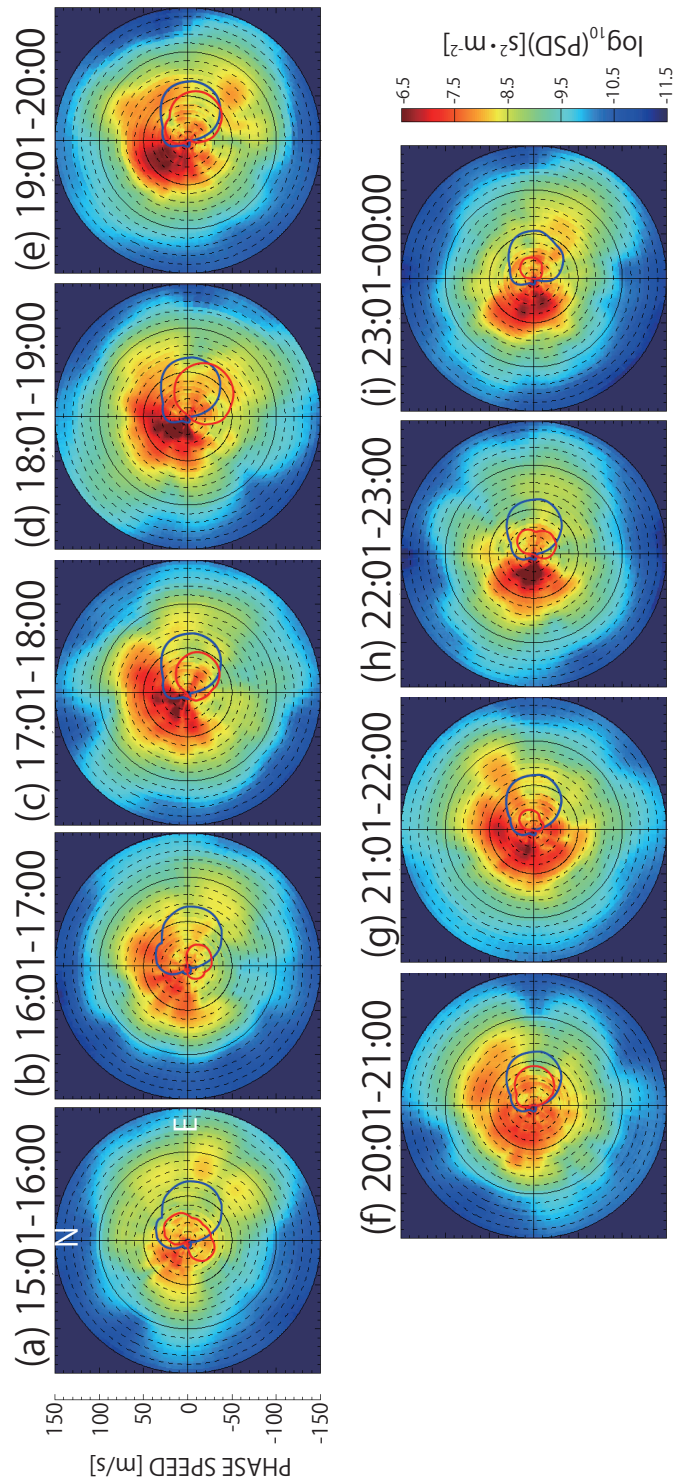


Figure 4.9: Hourly mean phase velocity spectra observed between 15:00 UT on May 11 and 00:00 UT on May 12, 2013, at Syowa. Blue and red circles indicate blocking diagrams calculated using MERRA wind (0–64 km) and MF radar wind (70–90 km), respectively. Note that MERRA wind is provided for every three hours.

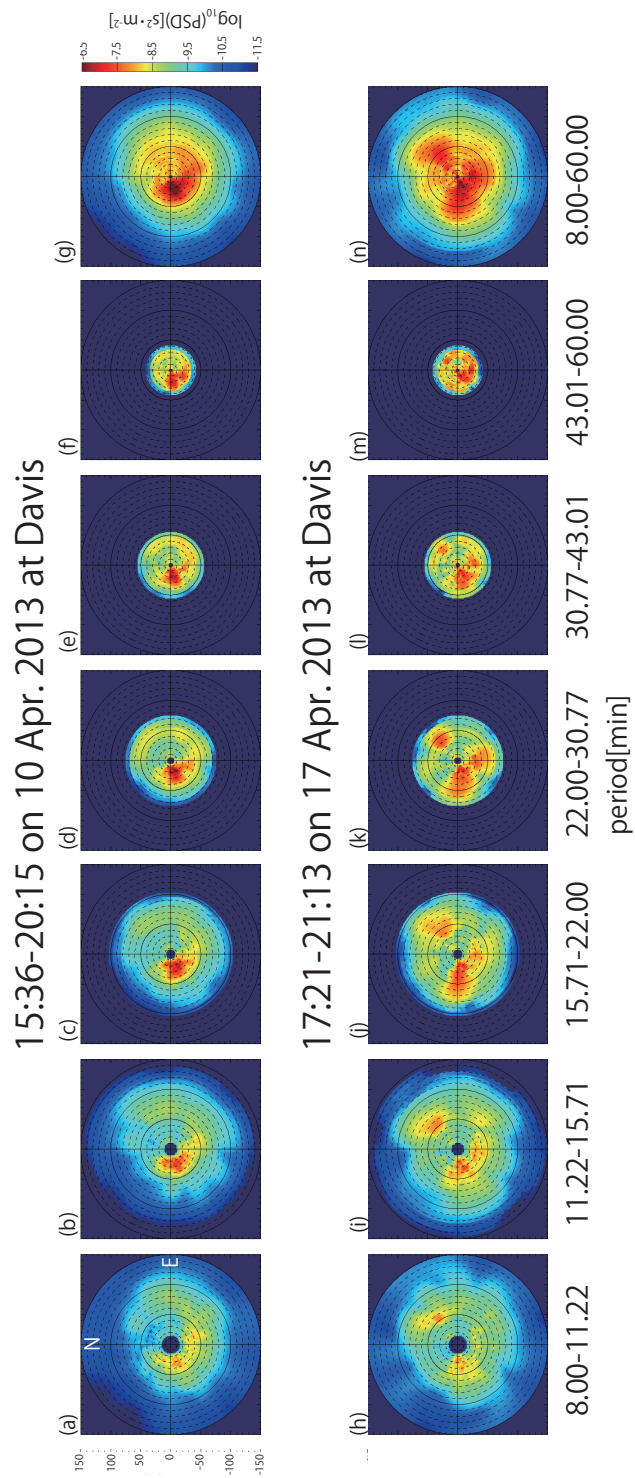


Figure 4.10: (Top panels) Phase velocity spectra for six period bands (a–f) and all periods between 8–60 min (g) observed at 15:36–20:15 UT on April 10, 2013, at Davis. (Bottom panels) Same as the top panels, except for the observation at 17:21–21:13 UT on April 17, 2013.

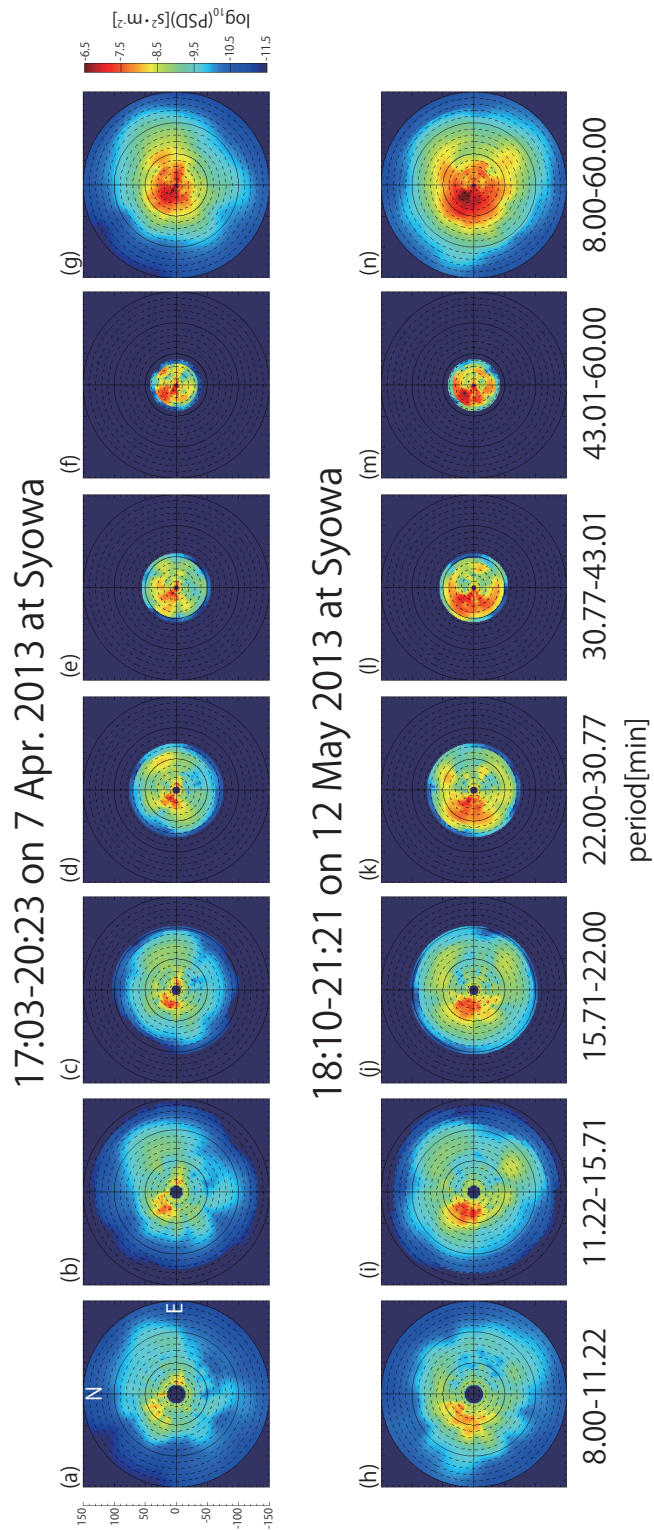


Figure 4.11: Same as Figure 4.10, except for the observation at 17:03–20:23 UT on April 7, 2013 (top panels), and 18:10–21:21 UT on May 12, 2013, at Syowa (bottom panels).

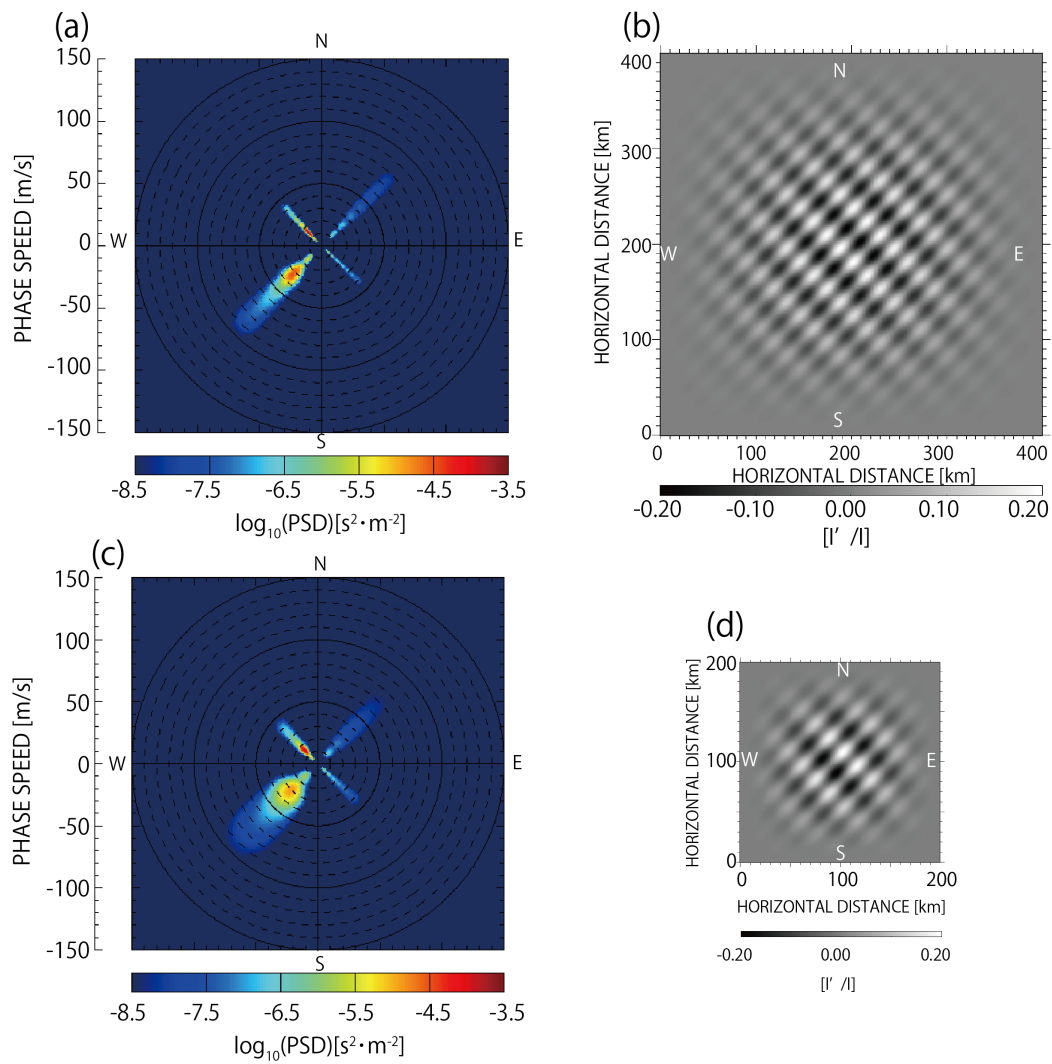


Figure A1: (a, c) Phase velocity spectra for test data and (b, d) examples image of test data corresponding to the spectra after application of a 2-D Hanning window, respectively. The spectra were derived from airglow images with a spatial size of (a)  $400 \times 400 \text{ km}^2$  and (c)  $200 \times 200 \text{ km}^2$  in geographic coordinates.

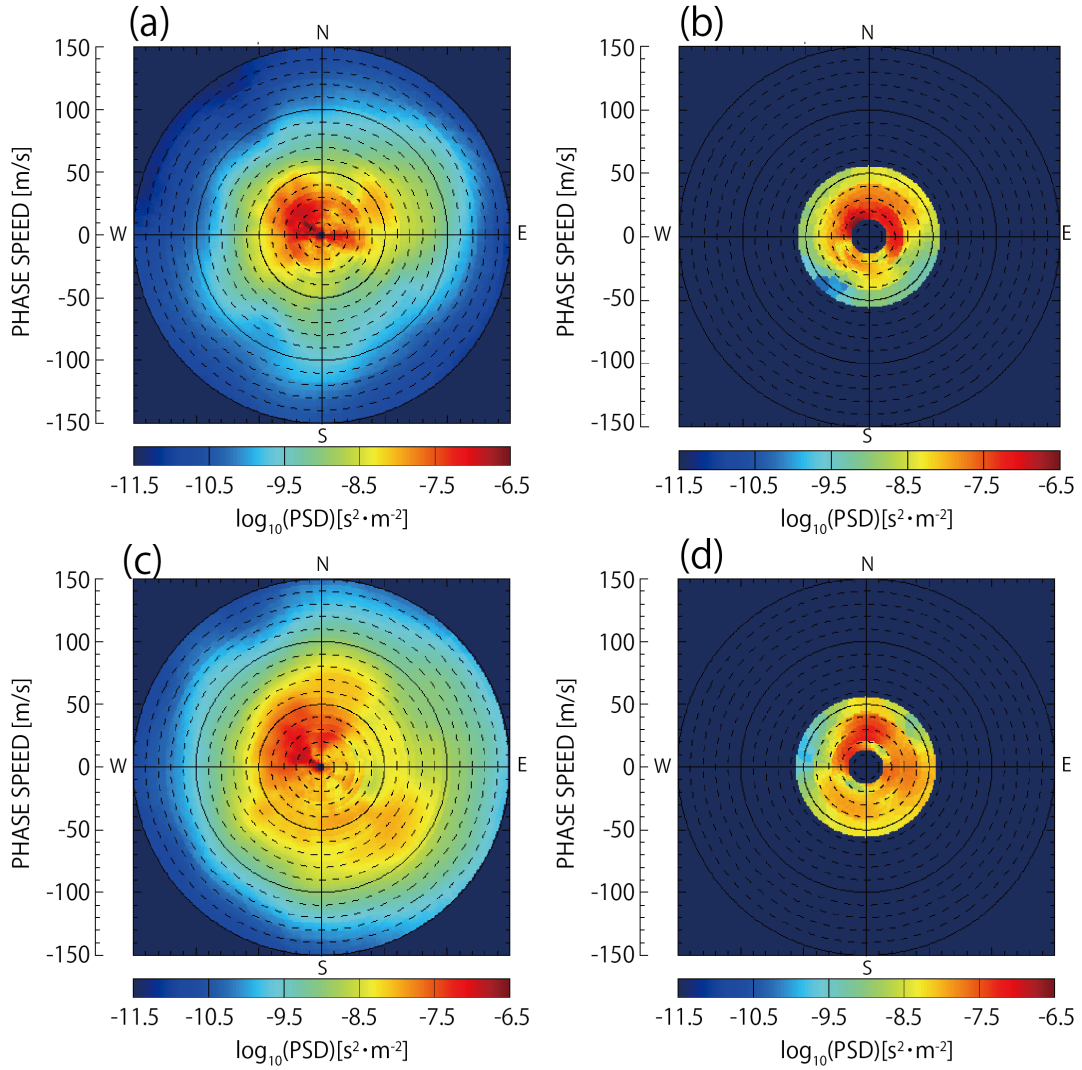


Figure A2: Phase velocity spectra (a, b) observed at 17:03-20:23 UT on April 7, 2013, at Syowa and (c, d) observed at 19:03-03:00 UT on May 10-11, 2013, at Syowa. The spectral ranges are (a, c) horizontal wavelengths of 10-100 km and periods of 8-60 min and (b, d) horizontal wavelengths of 100-200 km and periods of 60-120 min.

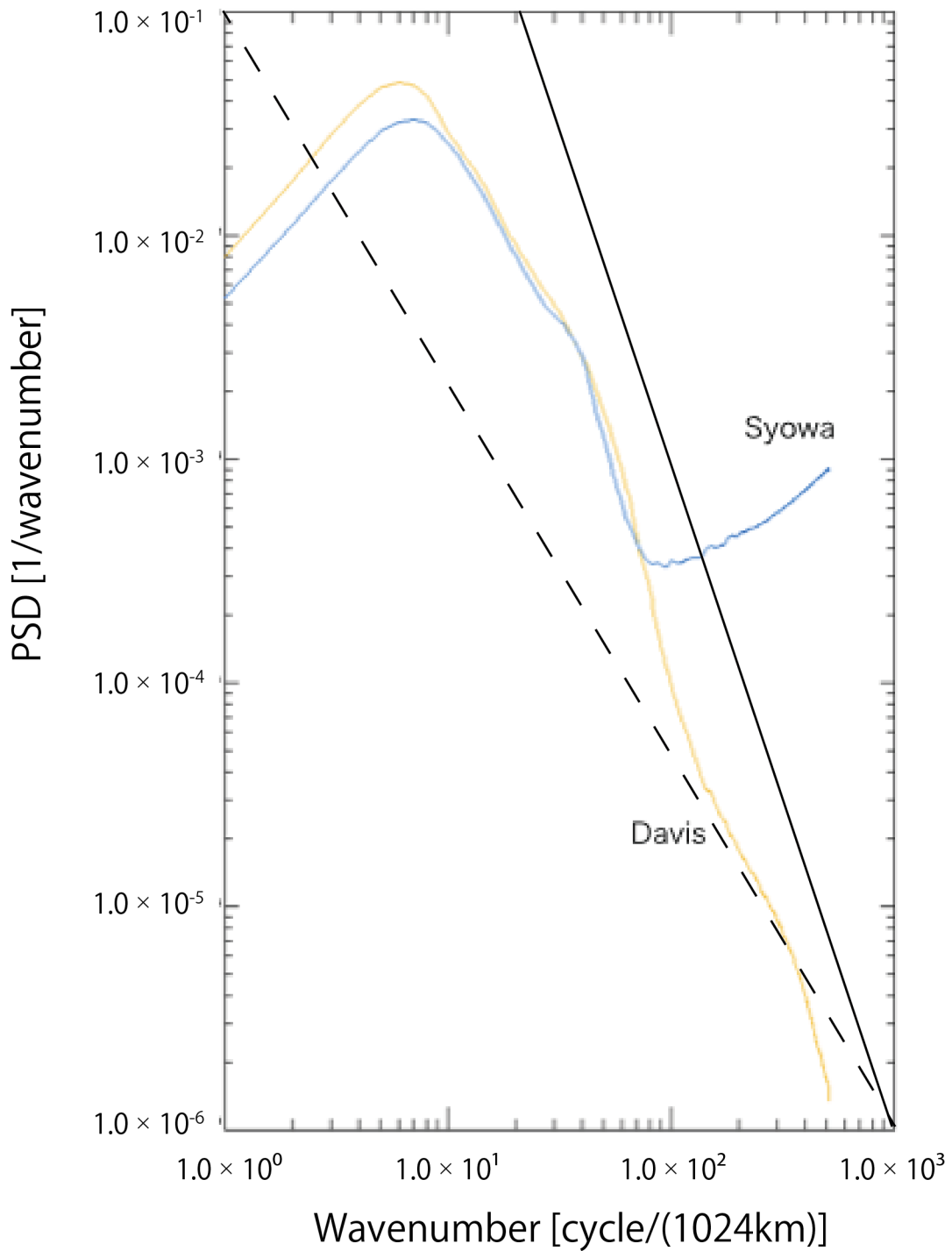


Figure A3: Averaged horizontal wavenumber spectra for the observation period at Syowa (blue) and Davis (yellow) during the period of Apr 7 and May 21 with two lines indicating the proportion of the 3<sup>rd</sup> (solid) and 5/3<sup>th</sup> (dash) power of the horizontal wavelength.

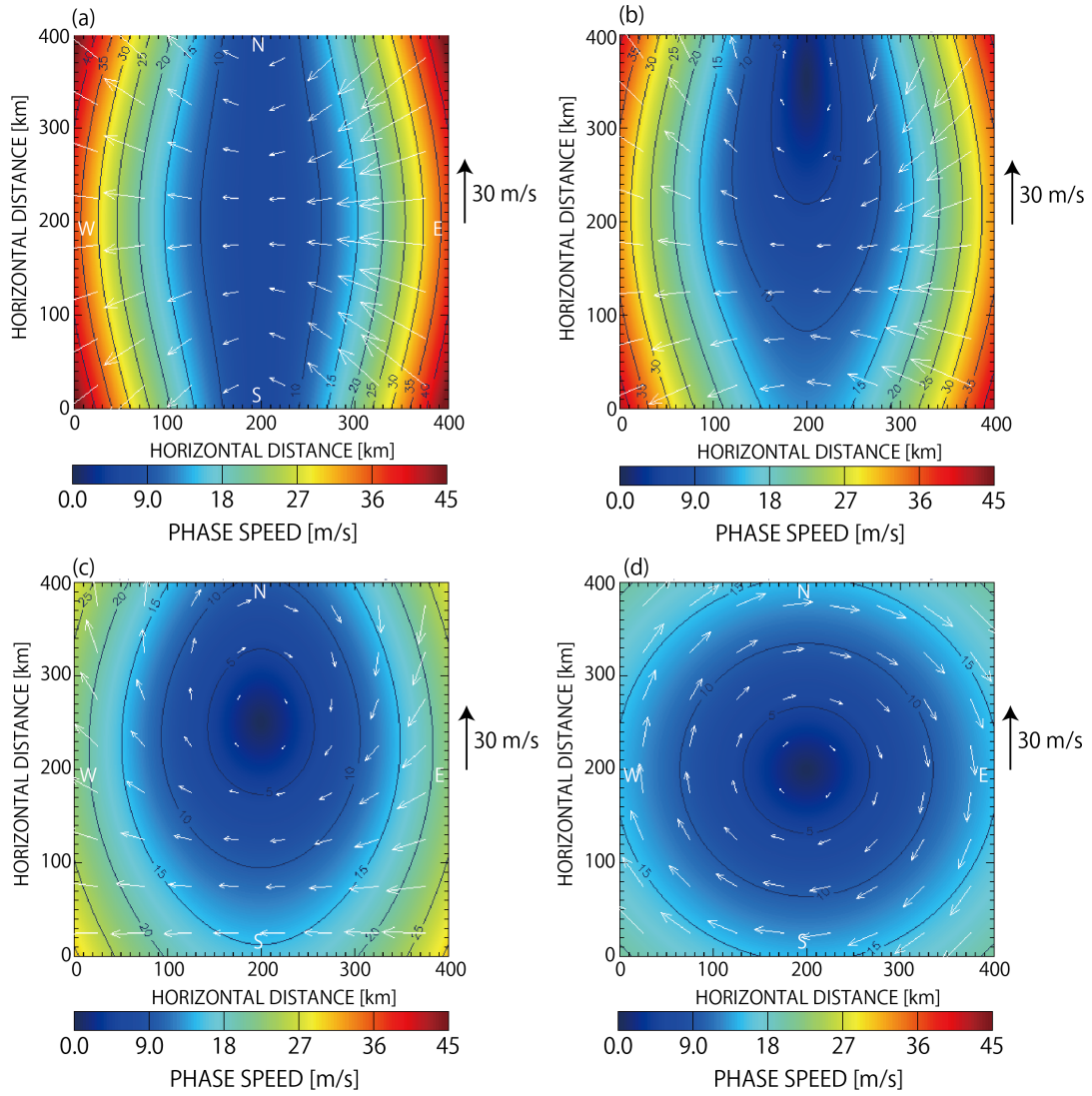


Figure A4: The virtual speeds (contour) and directions (arrows) of stars assuming the virtual height of 90 km in the image data projected onto the geographic coordinates at (a) 0°N, (b) 30°N, (c) 60°N, and (d) 90°N.